MOLECULAR BEAM EPITAXY GROWTH AND CHARACTERIZATION OF WIDE BANDGAP Zn(x)Mg(1-x)Se SEMICONDUCTOR MATERIALS AND HETEROSTRUCTURES FOR INTERSUBBAND DEVICES

by

MOHAMMAD A. SOHEL

A dissertation submitted to the Graduate Faculty in Chemistry in partial fulfillment of the requirements for the degree of Doctor of Philosophy, The City University of New York

2005

UMI Number: 3187389

UMI Microform 3187389

ProQuest Information and Learning Company
300 North Zeeb Road
P.O. Box 1346
Ann Arbor, MI 48106-1346

This manuscript has been read and accepted for the Graduate Faculty in Chemistry in satisfaction of the dissertation requirement for the degree of Doctor of Philosophy.

August 10, 2005 — Dr. Maria C. Tamargo

Date — Chair of Examining Committee

August 11, 2005 — Dr. Gerald Koeppl

Date — Executive Officer

Dr. Maria C. Tamargo

Dr. Daniel Akins

Dr. Hiroshi Matsui

Supervisory Committee

THE CITY UNIVERSITY OF NEW YORK

ABSTRACT

Molecular Beam Epitaxial Growth and Characterization of Wide Bandgap Zn(x)Mg(1-x)Se Semiconductor Materials and Heterostructures for Intersubband Devices

By

Mohammad A. Sohel

Thesis Advisor: Prof. Maria C. Tamargo

This thesis describes the molecular beam epitaxy (MBE) growth and characterization of the $Zn_xMg_{(1-x)}Se$ based semiconductor material system grown on InP substrates for quantum cascade lasers (QCLs) and other intersubband devices for room temperature operation and application in ultra fast optical communication.

Wide band gap II-VI semiconductor materials containing Mg, such as $Zn_xMg_{1-x}Se$, are of considerable interest for the fabrication of optoelectronic devices because their band gaps range from 2.75 to 3.7 eV, which allows us to reach higher bandgap values than those available from currently used II-VI materials. A series of high crystalline quality zincblende $Zn_xMg_{1-x}Se$ alloys was grown lattice matched to InP (001) substrates by molecular beam

epitaxy. Since we have used III-V InP substrates to grow this material, a lattice matched III-V InGaAs buffer layer, Zn irradiation and low temperature ZnCdSe interfacial layer was grown to improve the interface quality between III-V and II-VI material. The use of InP as a substrate allows us to optimize the material quality of the high Mg content compositions, since near lattice matching to this substrate is achieved with as much as ~87% Mg concentration. This lattice-matched alloy has a bandgap of 3.6 eV at 77K. The crystalline quality was assessed by X-ray diffraction techniques. The band gap energies of the alloys were determined using photoluminescence measurements and were plotted as a function of Mg concentration. A linear dependence between the band gap and the Mg concentration was observed for the entire range. From the extrapolation of our experimental data, the bandgap of zincblende MgSe was determined to be 3.74 eV.

Using $Zn_xMg_{1-x}Se$ as a barrier layer we have grown several $Zn_{x'}Cd_{(1-x')}Se/Zn_xMg_{(1-x)}Se$ single quantum well (QW) structures. These samples exhibited emission that ranges form the near-UV, throughout the visible range of the spectrum. The dependency of the QW emission with QW layer thickness was modeled using a finite barrier model. Finally, using a modulated spectroscopic technique known as contactless electroreflectance,

a very large conduction band offset for this QW structure, of ~1.12 eV, was estimated. This result makes this a very promising material for applications in the fabrication of intersubband devices such as quantum cascade lasers operating at room temperature or at short wavelengths such as 1.55 μm, as needed for ultra fast optical communications and other intersubband devices in the short wavelength region.

ACKNOWLEDGEMENTS

I would like to express my sincere gratitude and deep appreciation to my advisor Prof. Maria C. Tamargo for having introduced me into the field of semiconductor physics. Her encouragement and support has been of invaluable for this work.

I am also deeply indebted to Dr. Martin Muñoz of Virginia Commonwealth University, who during his postdoctoral research at City College has helped me with many ideas and advises on my dissertation project including the contactless-electroreflactence measurements and data analysis.

Many thanks are due to my past colleagues of the MBE group at City College : Dr. Shiping Guo, Dr. Oleg Maksimov, Dr. Xuecong Zhou, Dr. Francisco Fernandez, Hong Lu and M. Noemi Perez-Paz for their generous help regarding every possible issues in the lab. Also, thank is due to Dr. Aidong Shen for his comments and advise in the review of this dissertation.

I would like to thank my thesis committee members, Prof. Akins of City College, Dr. James D. Batteas of National Institute of Standard and Technology (NIST), and Prof. Hiroshi Matsui of Hunter College for serving in the committee. The support of the National Science Foundation -

Integrative Graduate Education and Research Traineeship (IGERT) through grant no. 9972892 is gratefully acknowledged.

I am very grateful to my wife, Shahida, for her support and encouragement through these years without which I could not concentrate on my research. Finally, my deepest appreciation is due to my parents for their support and encouragement during these years.

Contents

List of Illustrations

Chapter 1

Chapter 2

List of Tables

Chapter 3

Chapter 5

Chapter 1

Introduction

Since the demonstration of the first semiconductor lasers in 1962, the last four decades have seen a very rapid improvement in the state of the art of these devices due to the tremendous fundamental scientific discoveries that have taken place. Semiconductor lasers have been realized over a wide range of emission wavelengths in a variety of material systems. Most of the lasers used today are diode lasers, and the widespread applications of these tiny devices in laser printers, CD-players and for high-speed fiber optic communication have made diode lasers almost household objects. High power laser diodes have also revolutionized solid-state laser design, materials processing, printing, medical diagnosis and surgery. A number of significant breakthroughs, both in concepts, as well as growth and fabrication techniques have enabled this enormous development over the years. Key among these has been the concept of double heterostructure (DH) lasers, by Kroemer and Alferov, independently, followed by the separate confinement heterostructure (SCH) laser, the use of an ultra-thin quantum-well active region, and strained layer materials. Low dimensional electronic systems have been of considerable interest, as they have led to many

successful new technological applications. Low dimensional quantum well based optoelectronic and photonic devices such as diode lasers, detectors and light emitting diodes (LEDs) have been successfully demonstrated. The realization of these concepts has been made possible by advancements in various crystal growth technologies such as Molecular Beam Epitaxy (MBE), which enable us to control the layer thickness very precisely within monolayer accuracy. The choices of materials have also widened tremendously, including lasers from II-VI compounds, UV and blue-green lasers from the group-III nitrides and most recently, even electrically pumped organic lasers. Several other remarkable developments have occurred in the area of semiconductor lasers including the quantum wire and quantum dot lasers introduced by several groups, and a completely different class of semiconductor lasers: the unipolar quantum cascade lasers (QCLs), based on intersubband transitions within quantum wells (QWs).

Laser sources in the two wavelength windows of 3-5 μm and 8-13 μm in the mid-IR region have a wide range of industrial, military, and scientific applications such as highly sensitive trace-gas analysis, optical wireless communications, and others. The laser sources in the far-IR (THz) frequency range have potential applications in spectroscopy, astronomy, biological imaging, and free space communication. Ultrafast laser sources in the

wavelengths of 1.3 μm and 1.55 μm may also be very important for fiber-optic communications.

In QWs, the carriers are confined in one dimension. A thin layer of semiconductor material called the “active layer” is sandwiched between two layers with larger bandgap called the “barrier layers”. A schematic of a type I QW structure is shown in figure 1.1, where the smaller bandgap indium gallium arsenide (InGaAs) is sandwiched between two larger gap gallium arsenide (GaAs) semiconductor materials. A type I alignment implies that the energy gap of the narrow bandgap material is contained within the energy gap of the wide bandgap barriers, so that a potential well is produced both in the conduction and in the valence bands. In the example of Figure 1.1, the band gap of the InGaAs layer (E_g) is modified by quantum confinement and is shown as E_{QW}.

The conduction and valence band profiles are shown in the figure. Both electrons and holes can be confined along the growth direction depending on the relative band offset of the two semiconductor materials. Figure 1.1 also shows the quantized energy states of the well in the conduction and valence bands. By adjusting the thickness of the well, the barrier heights of the cladding layer, and their composition the energy levels can be manipulated within the quantum well.

An important phenomenon in these structures are the intersubband transitions, which are described as optical transitions between quantum-confined energy levels within the same band of either the conduction or valence band. These are illustrated in the figure by the blue arrow. Intersubband transitions have very short nonradiative relaxation times, which makes them very attractive for a variety of elements in high bandwidth fiber optical networks. This relaxation mechanism involves longitudinal optical phonons, carrier-carrier, and acoustic phonons; and depends mostly on the subband energy spacing, temperature, and material composition. Devices that depend on intersubband transitions include QCLs, quantum well infrared photodetectors (QWIP), and wavelength converters. QCL and QWIP are the two principal devices of interest in our group based on intersubband transitions.

The original concept of the quantum cascade laser was theoretically proposed by Kazarinov and Suris in 1971, who stated that, by applying a suitable voltage across a superlattice (SL) with electronic states localized in the quantum wells, light amplification could be obtained by photon assisted tunnelling at a photon energy equal to the energy difference between the ground state of a quantum well and an excited state of the adjacent downstream conduction band quantum well.[1] The first prototype

intersubband laser emitting in the mid-infrared (IR) 4-12 μm was demonstrated by Faist, Capasso and co-workers at Bell Labs in 1994. [2] The realization of this concept has opened great opportunity with this new type of laser sources in the mid-IR range and far-IR range.

A QCL is based on intersubband-transitions, that is, where the optical transition occurs between discrete electronic states within the conduction band. These states arise from quantization of electron motion in the active region. Unlike other semiconductor light sources, the emitted wavelength is not determined by the band gap of the materials used. QCLs are "unipolar", that is, only one type of carrier, namely electrons, is needed. The emitted photon energy is determined by the separation between discrete electronic states in the conduction band of the active region. When appropriate bias is applied and an electric current flows through the laser structure, electrons cascade down an energy "staircase", and every time they "fall down a step" they emit a photon and lose energy. When the lower-energy electron leaves the first well, it enters a region of material where it is collected and injected into an adjacent active region where it emits another photon in the process.

In the QCLs, the main non-radiative path is optical phonon emission rather than Auger recombination as in the diode lasers. In the latter, the energy released by a recombining electron is immediately absorbed by

another electron then dissipates this energy by emitting photons. Since smaller bandgap results in larger Auger coefficient, the Auger effect become severe in diode lasers when the lasing wavelength reaches near the IR, resulting in high threshold pumping intensity and poor thermal behavior, and making room temperature (RT) CW mode operation impossible. [2] In QCLs, the non-radiative process via phonon emission leads to devices operating at higher temperatures.

Another important characteristic of the QCLs is the intrinsic high speed due to the ultrafast carrier lifetimes. Intrinsic bandwidths ranging from a few hundred gigahertzes to 1 THz can be possible in QCLs; the bandwith is limited to 20 GHz in the case of diode lasers. [3] Recently, QCLs with a repetition rate on the order of 10 GHz have been reported. [4, 5] This property makes QCLs particularly well suited for generating ultrashort pulses.

The materials used in QCLs have wider energy gaps than those used in mid-IR diode lasers. The energy gaps allow QCL materials to transport large currents that would damage devices made of narrow-gap semiconductor such as lead salts. As a consequence of the ability to carry a large current along with the cascade effect, high power outputs can be generated in QCLs.

Electrons in a QCL pass through a succession of closely coordinated quantum wells, releasing energy as they go, in the form of photons. The basic operating mechanism of QCLs is illustrated in figure 1.2. Each active region shown in the figure actually consists of a coupled QW structure, such that three levels are obtained. Population inversion is achieved between the two electron levels labelled as 3 and 2. The electrons emit a photon when they drop from state 3 to the lower energy state 2. The electron then relaxes down to level 1 via non-radiative transition. Energy level 1 is needed to make sure that the electrons are cleared away from level 2 in order to sustain the condition of population inversion. Such a three energy level system is treated as a single active region in QC lasers. The electrons then tunnel into level 3 of the second active region and again the similar energy photon is emitted as shown in Fig. 1.2. In this way, a single electron produces several photons as it cascades down a series of identical energy steps built into the laser by stacking several such active regions. Typically, 25 to 75 active wells are arranged in a QC laser, allowing 25 to 75 photons to be created per electron journey. Therefore, the external quantum efficiency, which is defined as the number of photons produced by the laser divided by the number of injected electrons, can be higher than 100%. Since only one injected electron is needed to produce multiple photons in the process, this is

a very efficient process compared to the recombination of one electron with one hole to create a photon, as in conventional semiconductor lasers.

The growing interest in QCLs and other devices based on intersubband transitions emphasizes the need to research relevant fundamental parameters of heterostructures such as the band offsets. In spite of the considerable advances that have been achieved in the development of the QCLs, several limitations have hindered the performance of this device. A critical one is the unavailability of mid-IR QCLs operating in continuous wave (CW) mode at room temperature (RT). Also, it is difficult to find a suitable material system for heterostructures in which the conduction band offset is large enough to accommodate intersubband transitions at 1.55 μm (0.8 eV) for ultra fast optical communication. Both limitations are related to the relatively small conduction band discontinuity present in the most frequently used systems based on GaAs and InP, which imposes the shortest wavelength limit of 8μm [6] and 3μm [4], respectively, for QCLs made from these materials. In order to overcome these limitations, studies of intersubband transitions have been recently extended to other systems based on GaN [7, 8], GaSb [9, 10], Si [11] and II-VI compounds. [12-15] Among the most relevant parameters for the intersubband devices are the band offsets. A large conduction band offset is desired for application in intersubband

devices such as QCLs in order to address the present limitations of these devices. [16-22] This thesis focuses on the materials research, development, fabrication and band-offset determination of material systems for application in QCL emitting in the 1.55 μm for ultra fast optical communication.

Previously, our group has reported the growth and properties of wide bandgap II-VI semiconductor family based on ZnSe, CdSe, and MgSe alloys grown on InP substrates. [23-24] These materials offered the possibility of designing entirely lattice matched structures, thus promising to be less prone to degradation than the ZnMgSSe/ZnCdSe materials grown on GaAs substrates for blue green laser diodes. [25] The $Zn_xCd_yMg_{1-x-y}Se$ quaternary alloys lattice matched to InP exhibit a wide range of band gaps, from ~2.18 eV to ~3.5 eV as illustrated in figure 1.3, which shows the relationship between band gap and lattice constant for these materials. Lattice constant is shown here as a lattice mismatch to InP as we are interested to grow on InP substrates. The vertical dashed line at the center of the figure indicates the position of zero lattice mismatch to the InP substrate. The black squares represent the reported values of the binary ZnSe, CdSe, and MgSe materials. The solid lines are the ternary boundaries of the $Zn_xCd_yMg_{1-x-y}Se$ quaternary material system. From this figure, it is clear that by adding Mg to the $Zn_xCd_{1-x}Se$ alloy and keeping lattice matched conditions, the band gap of the

$Zn_xCd_yMg_{1-x-y}Se$ quaternary material can be varied from 2.18 to 3.5 eV, covering nearly all the visible spectrum, from yellow to blue.

$Zn_xCd_yMg_{1-x-y}Se$ lattice matched to InP can be used as cladding and wave-guide layers in LEDs and laser structures. Using the lattice matched $Zn_{0.51}Cd_{0.49}Se$ ternary (2.1 eV) as a quantum well (QW) and $Zn_xCd_yMg_{1-x-y}Se$ as a barrier layer QW emission from yellow to blue has been demonstrated by simply varying the QW thickness. [26] Red emission was achieved by using a strained $Zn_xCd_{1-x}Se$ QWs ($\Delta a/a \sim 1.8\%$) with excess Cd. Also, their application as visible light emitters was demonstrated by fabrication of full color LEDs and optically pumped lasers in the red-green-blue regions. The electroluminescence spectra of several LEDs are shown in figure 1.4. [27-28] In practice, the quaternary composition with highest bandgaps that we have been able to achieve with good crystalline quality is 3.25 eV. Higher Mg contents of the quaternary lead to deterioration of the crystalline and optical properties.

Furthermore, our group has recently reported the band-offset determination of the lattice matched $Zn_{0.53}Cd_{0.47}Se/Zn_{0.29}Cd_{0.24}Mg_{0.47}Se$ material and obtained a conduction band offset of 0.59 eV. [29] Such a large band offset makes this material attractive for application in QCLs and other intersubband devices. In order to increase the conduction band offset of

these structures it is desirable to increase the bandgap of the barrier layer. In this work we have investigated the growth and characterization of a new II-VI material, ZnMgSe ternary near lattice-matched to InP, where the band gap can be tuned up to 3.6 eV. The use of lattice matched ZnMgSe as the barrier of ZnCdSe QWs on InP should allow us to fabricate quantum cascade lasers with a larger conduction band offset for ultra fast optical communications in 1.55 μm.

In chapter 2, the basics principles of the MBE growth technique and sample characterization techniques such as X-Ray, photoluminescence, and contactless electroreflectance (CER) will be discussed.

In chapter 3, the MBE growth of high quality $Zn_xMg_{1-x}Se$ ternary alloy on InP substrates will be introduced. The growth conditions, assessment of the composition by X-ray, optical property analyses by photoluminescence, and detailed analyses of the sample will be presented. Based on our data, the bandgap of the zincblende MgSe will be determined and compared to estimated values.

In chapter 4, the growth of the ZnCdSe/ZnMgSe quantum well structures and their photoluminescence studies will be discussed. PL emission as a function of quantum well thickness will be presented which shows emission from near-UV to the visible range of the spectrum.

In chapter 5, the band-offset determination of the ZnCdSe/ZnCdMgSe and ZnCdSe/ZnMgSe quantum well structures using contactless electroreflectance and their possible application in the quantum cascade laser for ultra fast optical communication will be presented.

Finally, chapter 6 is the summary chapter, along with the publications highlights the key achievements obtained through this dissertation.

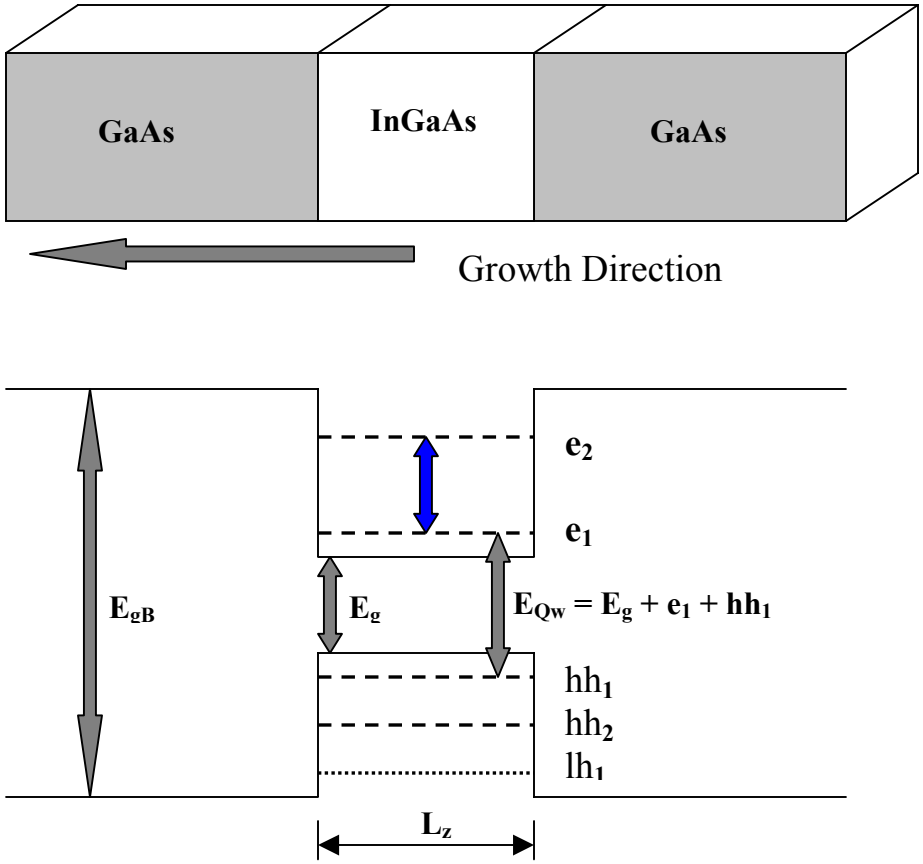

Figure 1.1 Schematic diagrams describing the quantum size effect in GaAs/InGaAs/GaAs quantum well.

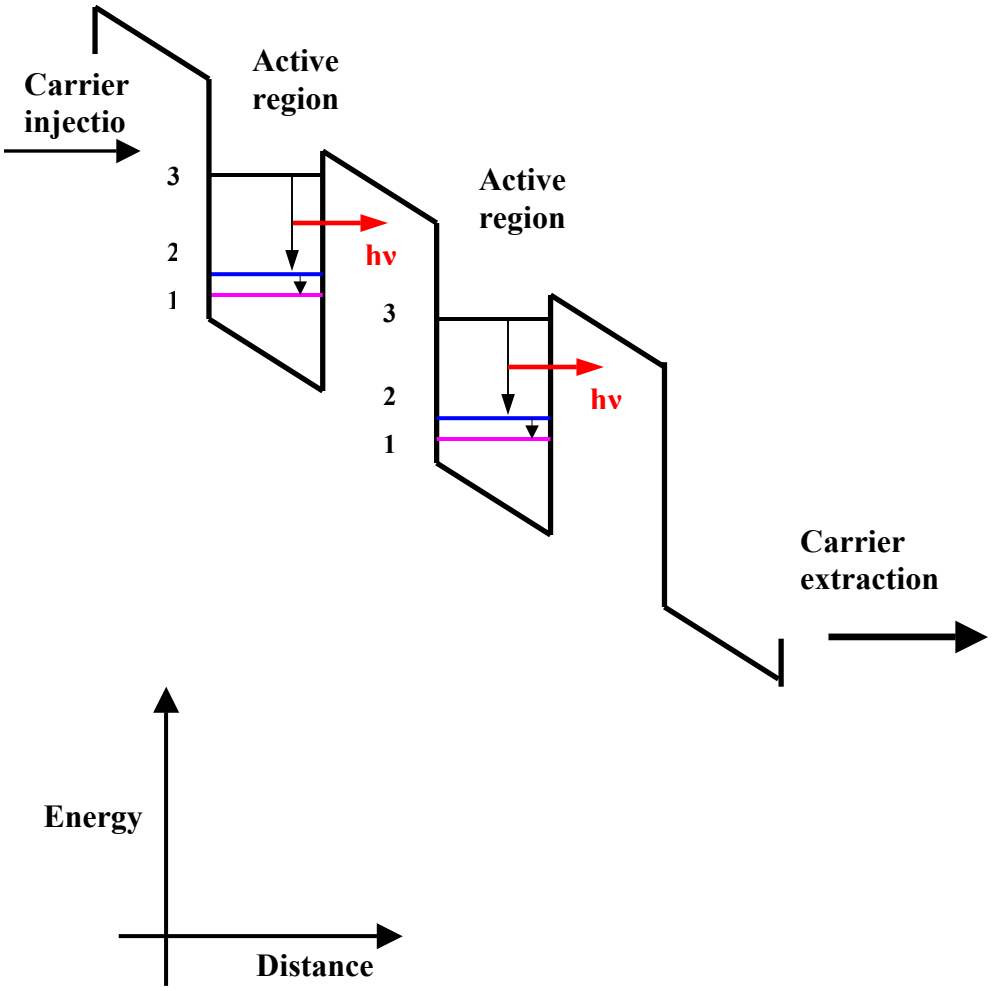

Figure 1.2. Basic principles of quantum cascade laser operation.

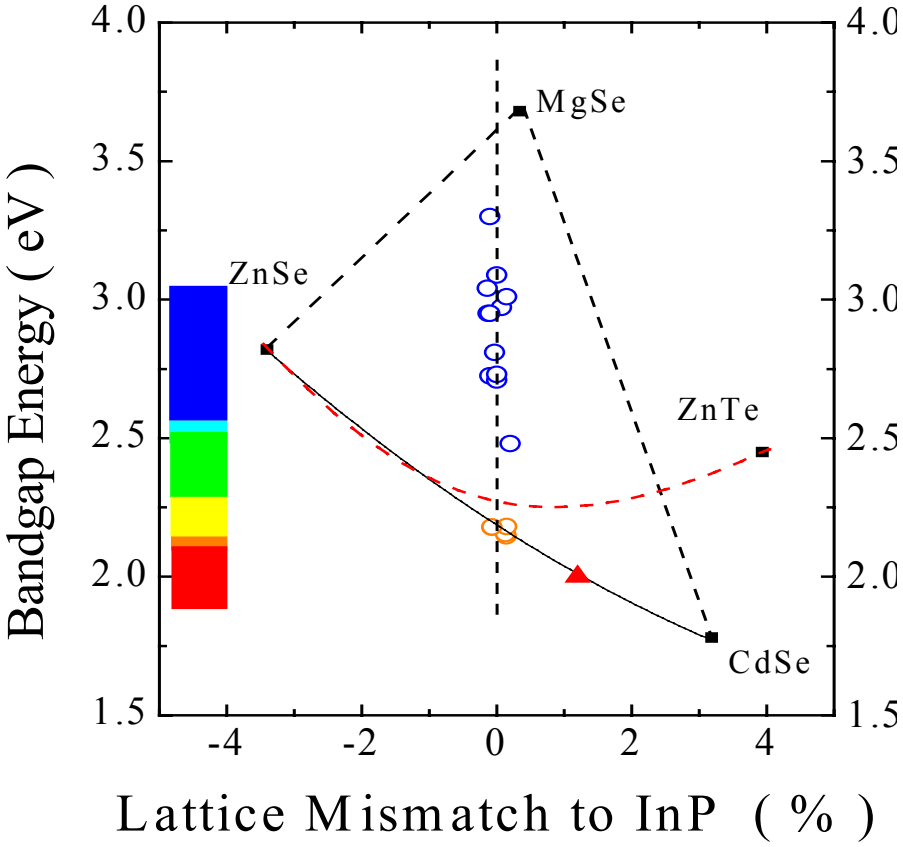

Fig. 1.3. Band gap energy versus lattice mismatch to InP substrate for $Zn_xCd_yMg_{1-x-y}Se$ material family.

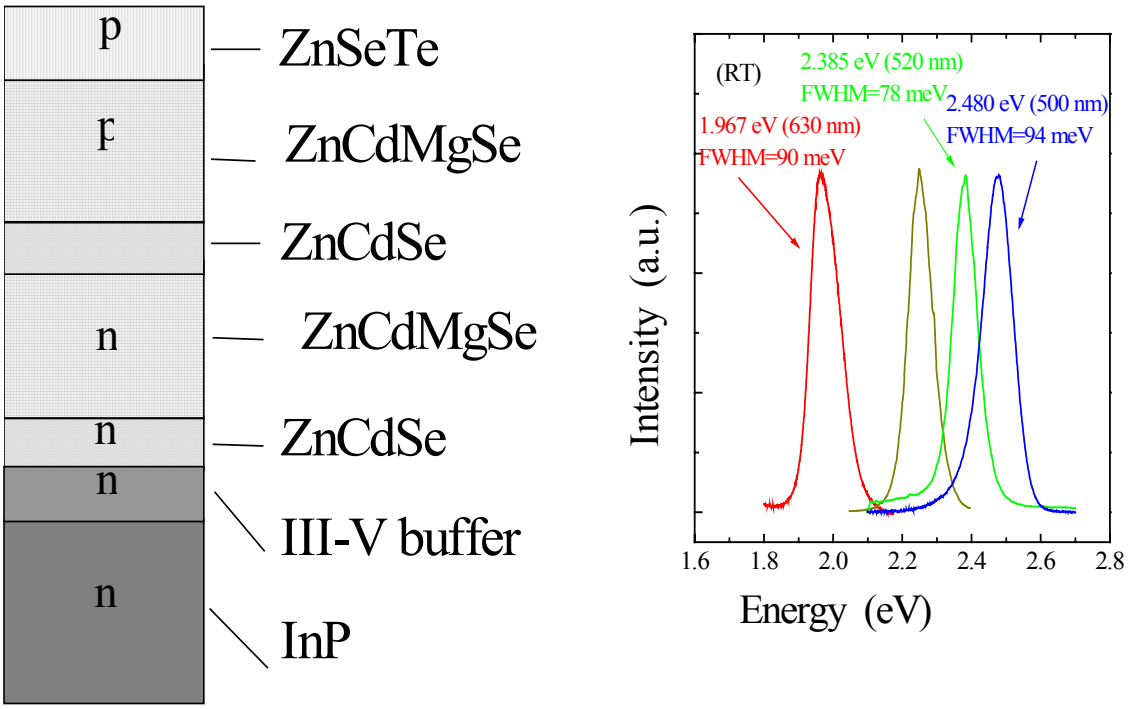

Fig. 1.4: Schematic of LED structures and their room temperature electroluminescence spectra.

Chapter 2

Background and Experimental Techniques

2.1. Molecular Beam Epitaxy System

The high quality of interfaces is essential for the good performance of heterostructure-based optoelectronic devices. The interfaces should be abrupt and free of defects and impurity states. For quantum cascade lasers (QCL) this is very important because their performance depends on the transport of carriers across many layers. The presence of defects and irregularities at the interfaces will undoubtedly reduce the efficiency of this process. Molecular beam epitaxy (MBE) is a unique technique that enables us to control interfaces very precisely for fabrication of the heterostructures for devices such as QCLs.

MBE is a versatile technique for epitaxial growth of semiconductor thin films. [1] In this process of deposition, epitaxial films grow from molecular or atomic beams on a heated substrate under ultra high vacuum (UHV) conditions. The basic MBE process is schematically illustrated in fig. 2.1. Under UHV conditions, the system is far removed from thermal equilibrium and the crystal growth is primarily governed by surface kinetics.

[2] The beams are thermally generated in Knudsen-type effusion cells that contain the constituent elements or compounds of the desired epitaxial films. The temperature of the cells is accurately controlled to give thermal beams of appropriate intensity. The thermal beams escaping from the orifices in the cells travel in a rectilinear path to the substrate where they condense and grow under kinetically controlled growth conditions. [3]

One characteristic of MBE is that UHV conditions during the growth process can produce very pure materials with low impurity concentration. In addition growth and alloy composition can be very well controlled and the interface between two layers has near atomic smoothness with very high quality. Usually the impinging atoms that arrive on the surface are controlled by means of their fluxes, which depend on the temperature of the cell of interest. By varying the temperature of the cell, the flux could be adjusted to grow any specific composition of the epilayers or structures.

A cross section of an MBE growth chamber is shown in figure 2.2, which shows a detailed description of its components. To achieve UHV conditions from atmosphere, the system is pre-pumped with standard mechanical and adsorption pumps. A combination of ion pump, cryo pump and titanium sublimation pump are used to achieve ultra high vacuum up to 10^{-9} torr. In order to attain a pressure as low as 10^{-11} torr for pre-growth

condition (before heating the cells), a combination of an ion pump along with a titanium sublimation pump (or cryo pump), and a cryo panel surrounding the chamber filled with a liquid nitrogen flow is used. The liquid nitrogen shroud prevents the cross heating and cross contamination of the cells and reduces the partial pressure of the unused cells. The molecular beams are generated in Knudsen type effusion cells whose temperatures are controlled to an accuracy of ±1ºC in the UHV system. The beam fluxes that are emerging from the non-equilibrium effusion cells are generally determined experimentally using a nude ionization gauge that is placed in the substrate position.

The substrate holder is located along the central line. All the cells are angularly oriented in a way so that their beams converge on to the center of the substrate holder. The cells are equipped with shutters to open and close the cells, and, therefore, interrupt the fluxes as needed. The crucibles that contain the evaporating materials are made of Pyrolytic Boron Nitride (PBN) and they are surrounded by tantalum or molybdenum wires for resistive heating. Both the substrate holder and the crucible are attached to a tungsten-rhenium thermocouple for precise control of the temperature. The furnace filaments are powered via a proportional-integrating-differentiation (PID) power control unit. The parameters are set according to the particular

material and furnace size. During the growth process the substrate is heated up to a certain temperature to provide mobility of the impinging and condensed atoms, and rotated to achieve layer uniformity. The ability for the impinging atom to move on the surface is essential for high crystalline quality and layer uniformity. In order to monitor the *in-situ* deoxidation of the substrate and growth of the layers, the chamber is equipped with reflection high-energy electron diffraction (RHEED), which is described later in section 2.2. The typical MBE growth rate is ~1 μm/h, which is low enough to ensure surface migration of the impinging species.

The research for this dissertation was accomplished in a Riber 2300 MBE system. The schematic for this particular system is shown in figure 2.3. As shown in the figure, there is a loading chamber through which the substrates mounted on to the molybdenum blocks for easy handling, are introduced into the system; and then unloaded after growth. The system also contains two growth chambers, and a metallization chamber. They all are connected via UHV transfer modules. One of the growth chambers is dedicated to grow III-V materials and the other one is for the II-VI materials. The III-V chamber is equipped with effusion cells of group III materials such as In, Ga, and Al and As as the group V material. Cells for Be and Si are also contained in the III-V chamber for p-type and n-type dopant

sources. The II-VI chamber consists of Zn, Cd, Mg, Be sources as group II elements and Se, and Te as group VI element sources. A radio frequency (RF) nitrogen plasma source for p-type doping and a $ZnCl_2$ source for n-type doping are also incorporated in the II-VI chamber. Both chambers are pumped with ion pumps along with titanium sublimation pumps. In addition, the II-VI chamber is equipped with a cryo pump, which is used during the p-type doping with nitrogen plasma source. The loading chamber is equipped with a turbo molecular pump and the transfer channel is equipped with ion pumps. The loading chamber, growth chambers, and transfer channel all are separated from each other by gate valves.

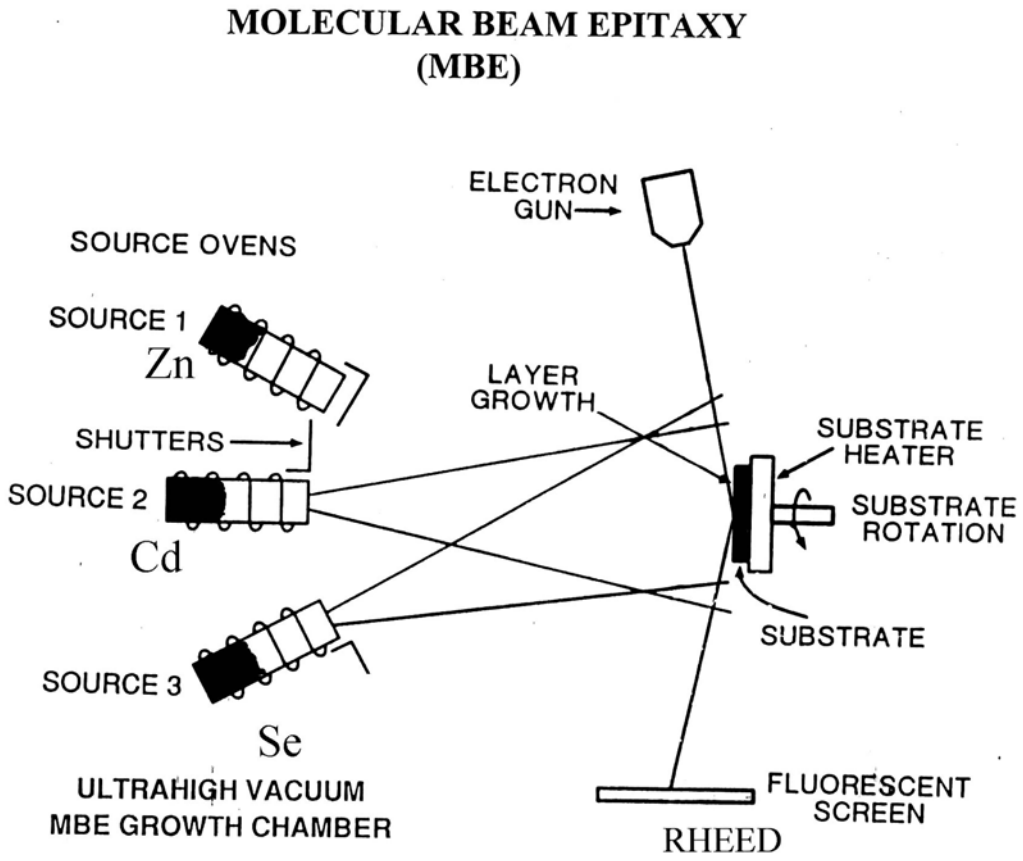

Figure 2.1 Schematics of MBE process.

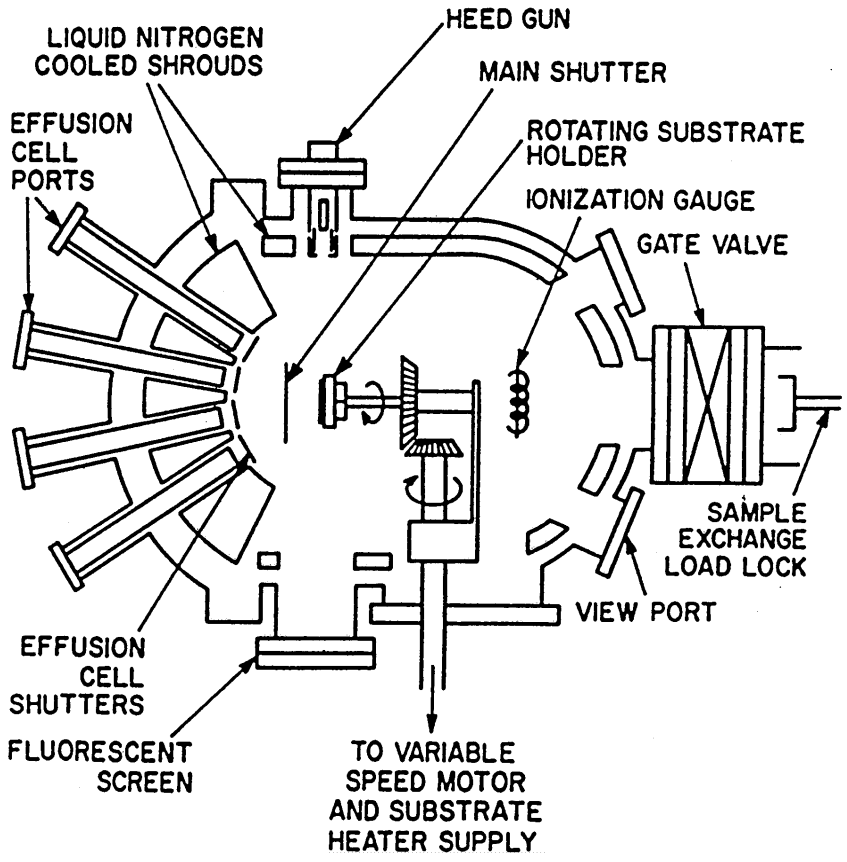

Figure 2.2. Cross section of a MBE chamber viewed from the top.

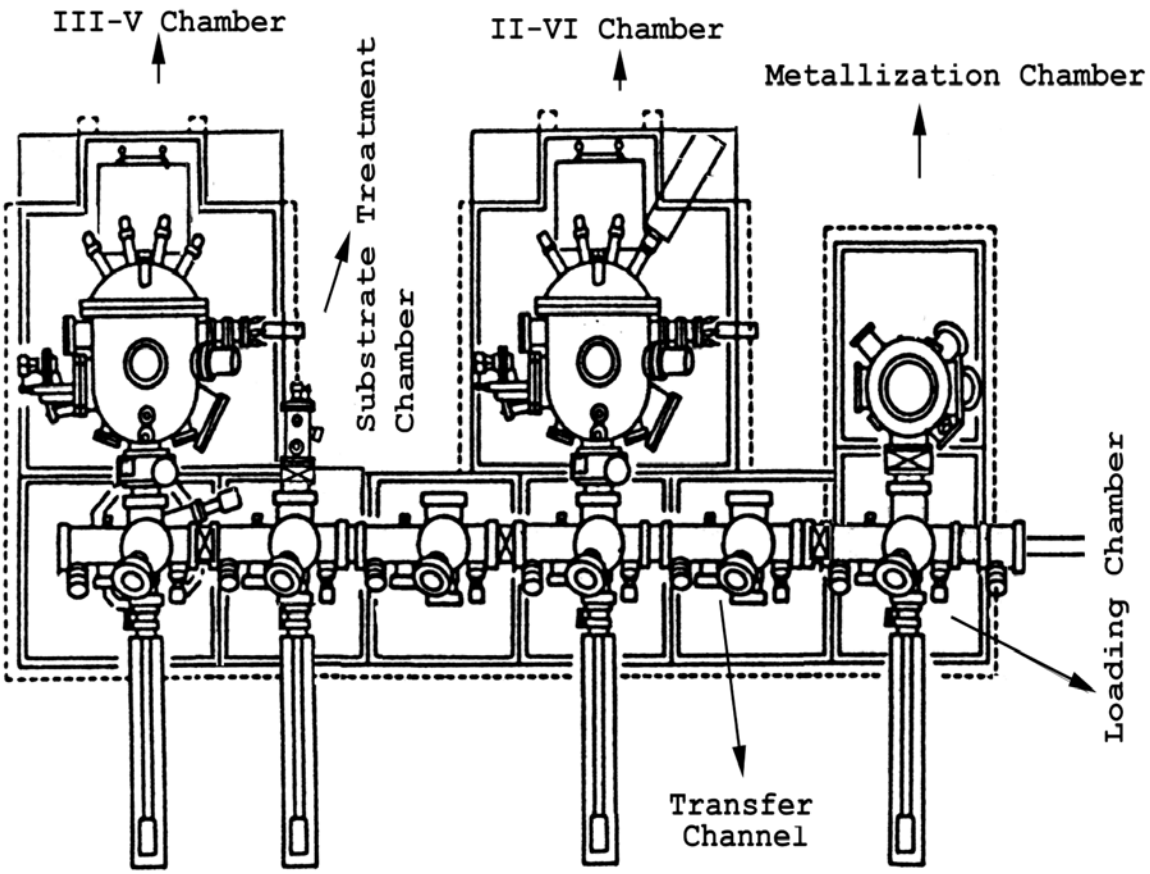

Figure 2.3. Riber 2300 MBE system at City College.

2.2. Reflection High Energy Electron Diffraction (RHEED)

Reflection high-energy electron diffraction (RHEED) is the most important tool used during growth. It allows us to get an immediate feedback of the growth process *in-situ*. The RHEED patterns obtained at glancing incidence provide information on surface reconstruction, microstructures, and surface smoothness. [2] The equipment consists of an electron gun, emitting electrons with high kinetic energy of 10 – 100 KeV. The beam hits the substrate surface at a very low angle (~1º) penetrating through a very thin layer of the surface where it becomes diffracted as shown in figure 2.4. This gives rise to a diffraction pattern that is projected on the phosphor fluorescent screen. The diffraction pattern is unique for a given azimuthal orientation of substrate and provides, in addition to the surface structure, information about surface quality and growth mode.

The RHEED pattern depends on the atomic arrangements, flatness and direction of the surface. A typical expected RHEED pattern is two-dimensional streaky pattern where streaky sharp lines indicate the well-ordered and flat surface. [4] For example, a surface structure denoted by GaAs (001) (m x n) means that a GaAs crystal is oriented with the [001] direction normal to the surface and has a surface structure due to the reconstruction whose unit cell is m x n times larger than the underlying bulk structure. A (4

x 2) RHEED pattern that is typically observed in the fluorescent screen during GaAs growth by MBE means a four-fold periodicity in the [1$\bar{1}$0] direction and two-fold periodicity in the [110] direction. In one direction the periodicity with respect to the bulk lattice is every second lattice point and in the perpendicular direction it is every fourth lattice point as shown in figure 2.5.

An As terminated surface of (001)GaAs in the (100) growth direction, is (2x4) or c(4x4) or c(2x8) depending on how much excess As is on the surface. The Ga terminated surfaces of (001)GaAs are (4x2) or c(8x2). [5] In that case, the four-fold periodicity in the [110] direction and two-fold periodicity in the [$\bar{1}$10] direction occurs which appears on the screen. [6] Similarly, the Zn terminated surface of ZnSe is c(2x2), and the Se terminated surface is a (2x1) streaky RHEED pattern. [7] Other RHEED pattern qualities, such as spotty or arrow shaped appearance, indicate three-dimensional growth, and usually a poor crystalline quality. During the crystal growth a very precise ratio of V/III fluxes for III-V material growth, or VI/II fluxes for II-VI growth are needed to maintain stoichiometry at the surface. If stoichiometry is not maintained there is a likelihood of the formation of metallic islands. These will inevitably lead to defective growth. All these growth possibilities can be monitored *in-situ* via observation of the

RHEED pattern. Before the initiation of the growth, substrate deoxidation, a crucial step of the growth can also be monitored via RHEED as the pattern changes from a hazy diffuse glow, (oxidized) on the phosphor screen to a streaky pattern as the substrate temperature is increased and the oxide is desorbed during the deoxidation process prior to growth.

Routine calibration of the source material such as group III beam flux to maintain flux ratios can be performed by observing the RHEED oscillations. This can be done through an optical fiber, which guides the diffracted lines to a photo multiplier tube (PMT), which gives an electrical signal to a recorder. The reflected beam from the sample changes its intensity periodically as each atomic monolayer (ML) is deposited on the substrate, as can be seen in figure 2.6. The RHEED intensity initially decreases, with respect to the static conditions, and starts to oscillate periodically, with damped intensity, until the shutters are closed again. The origin of the oscillations is illustrated in figure 2.7. If the initial surface is perfectly flat, reflectivity of the specular spot will be relatively high. As layer-by-layer growth starts, the incident electron beam gets partially scattered by the island steps of the forming monolayer, thus reducing the reflected intensity. Scattering becomes a maximum at half-monolayer coverage, while as the new monolayer completes, the surface flattens again

by coalescence of the islands, and the reflected intensity recovers its value. [8] The continuation of the RHEED oscillations can therefore be considered as a measure of the layer-by-layer epitaxial quality during growth. However, as shown in figure 2.6, the oscillations dampen as growth proceeds, and eventually disappear. This is because at higher coverage the growth front becomes statistically distributed over more and more layers (a new ML starts before the preceding one completes), yielding eventually a constant surface roughness.[8] The period of the oscillation is the time it takes to grow one monolayer, and the growth rate can be deduced very accurately from this. [9]

The Bragg condition $2d\ Sin\theta = n\lambda$ can be applied in the case of RHEED by assuming that the lattice spacing is d, the distance between substrate and the fluorescent screen is L, the separation between the streaks on the screen is $\lambda L/d$ for small angles. The wavelength λ of the electron is related to the kinetic energy, which is 10 KeV in our case, which results in a wavelength of approximately 0.12 Å. Thus the lattice spacing d, can also be obtained from the RHEED pattern.

In conclusion, from the RHEED observation during the *in-situ* growth, we can know whether deoxidation has been performed on the surface of the substrate, whether the growth is two dimensional, which element terminates the surface, the growth rate of the sample by observing

the oscillation of the RHEED during growth, and finally, the lattice spacing of the material's crystal structure.

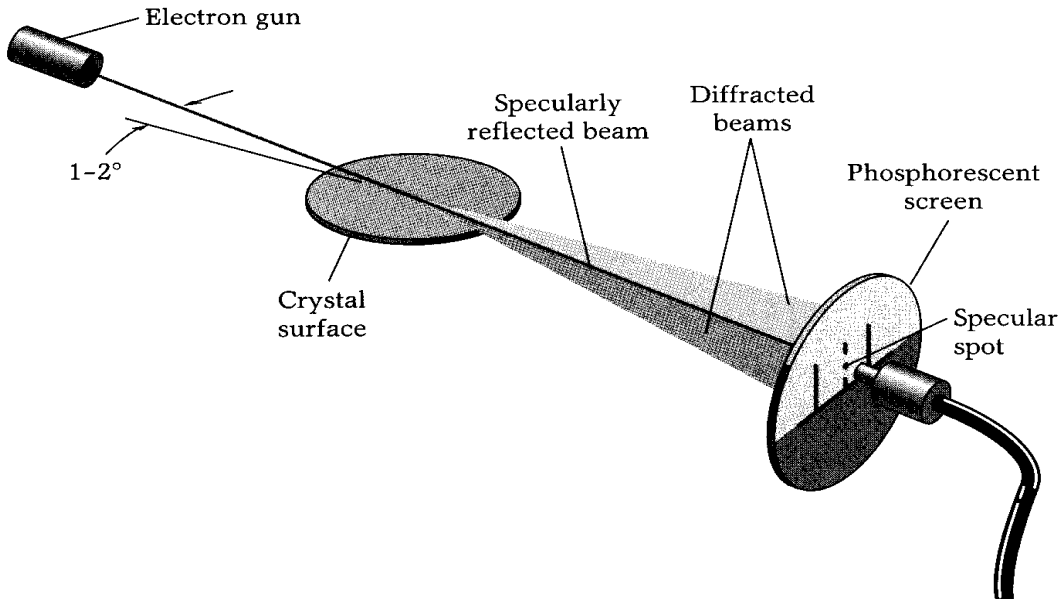

Fig. 2.4. Schematic of the RHEED and RHEED oscillations measurement.

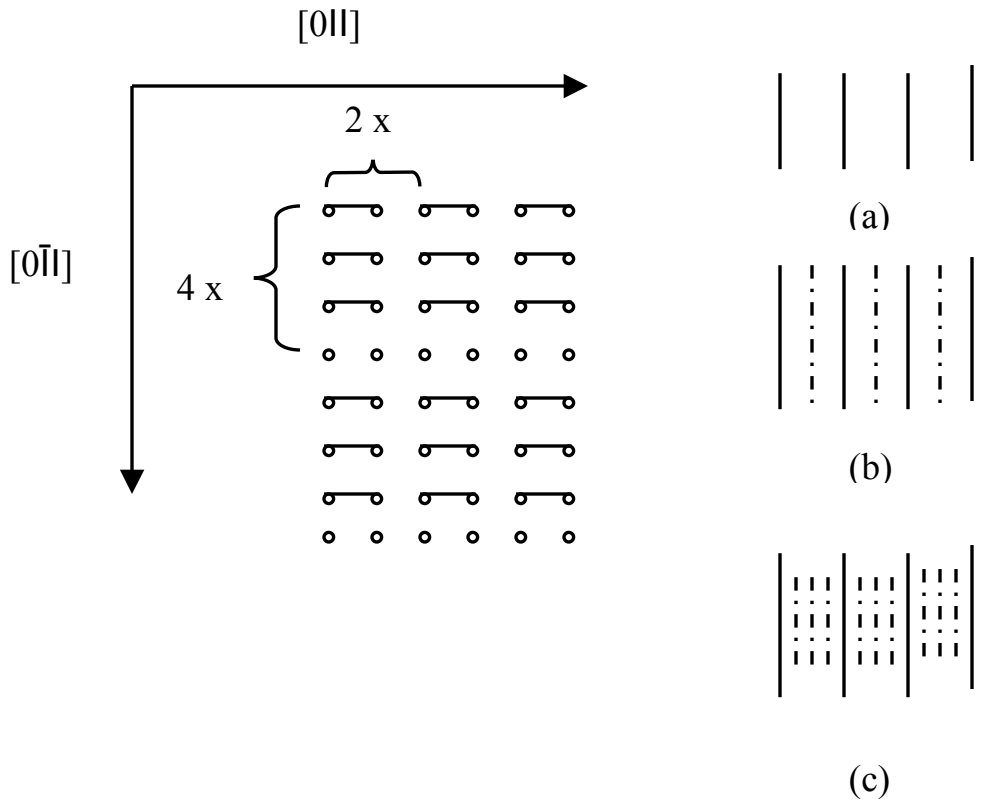

Figure 2.5. A (001) GaAs (2 x 4) As terminated surface (a) An un-(1 x 1) RHEED pattern (b) 2-fold and (c) 4-fold RHEED pattern.

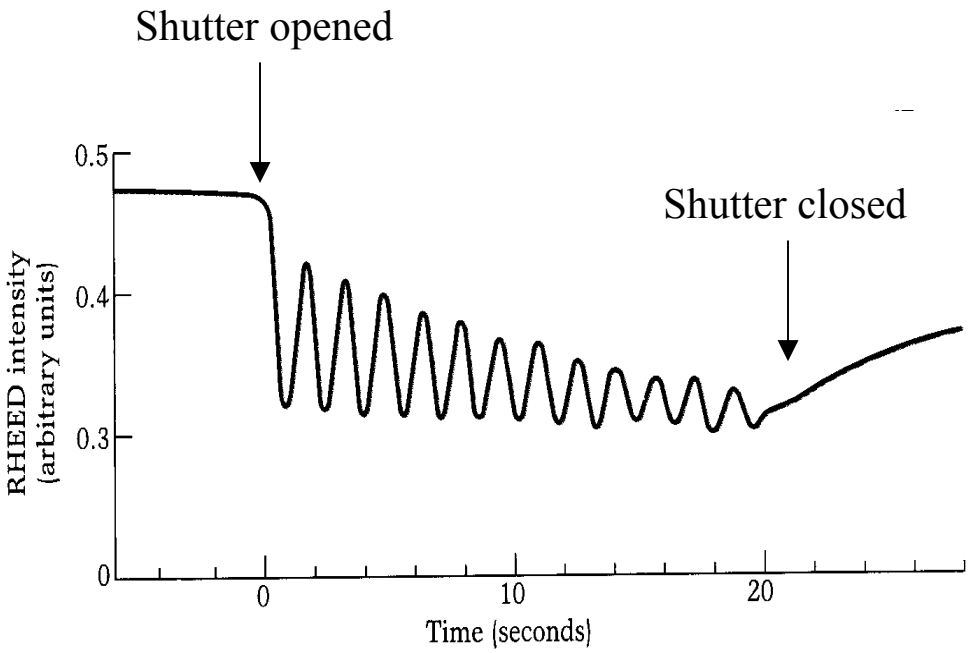

Fig. 2.6. Diagram of RHEED intensity oscillations vs. time.

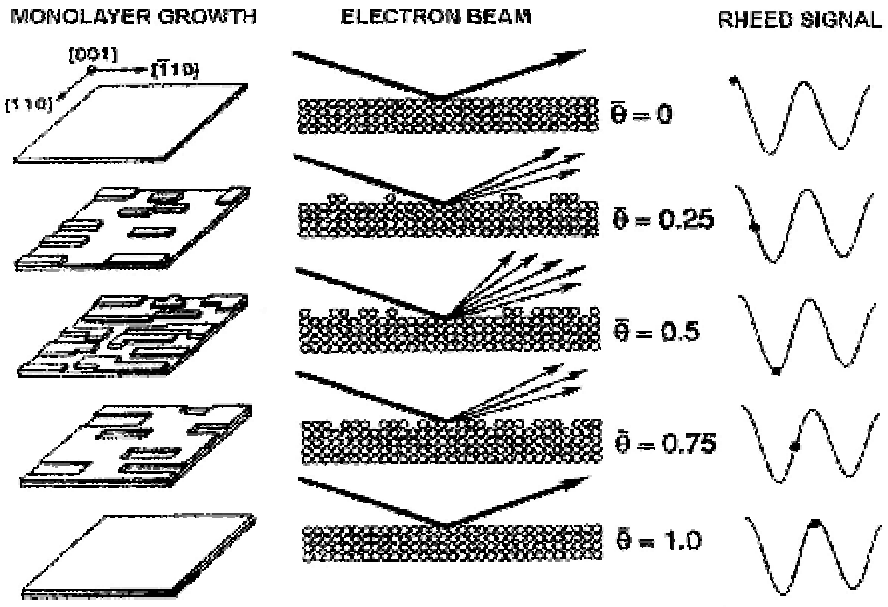

Figure 2.7. Mechanisms of RHEED intensity oscillations during growth of a monolayer. (Ref. 8)

2.3. X-Ray Diffraction

X-ray diffraction (XRD) is used in many applications to study parameters that depend on the crystal structure. Structural information can be obtained conveniently by XRD. For example, the value of the lattice constant, which is deduced from the XRD, can be used to determine alloy composition, structural arrangement, inner diffusion at heterostructures, strain in materials, thickness of embedded layers and parameters of super lattices. The XRD measurement is very simple to perform, it is non-destructive and the samples can be easily mounted directly after they are grown and do not require any prior preparation. In our case we use single and double crystal XRD on a routine basis to determine the alloy composition, lattice mismatch with respect to the substrate, and crystalline quality of the epilayers.

The XRD is based on Bragg's law, which is based on the condition for the constructive interference:

$$2d_{hkl} \, Sin\theta = n\lambda \qquad (2.1)$$

and $$d_{hkl} = a/(h^2 + k^2 + l^2)^{1/2} \qquad (2.2)$$

where, d_{hkl} is the spacing of the lattice planes with miller indices (hkl), θ is the Bragg angle between the planes and the incoming x-ray beams, a is the lattice constant, λ is the x-ray excitation wavelength, and *n,* an integer which

is the order of diffraction. The x-ray diffraction geometry has been described in figure 2.8, where φ is the angle between lattice plane and the surface, k_1 and k_s are the incident and scattered wave vector, respectively.

If φ = 0, the reflecting lattice planes are parallel to the surface and the reflection is called a symmetric Bragg reflection. For φ ≠ 0, the Bragg reflection is called asymmetric Bragg reflection. Since the excitation wavelength λ is 1.5406 Å for a Cu source, and using the lattice constant, the Bragg angle for widely used substrates such as GaAs and InP can be calculated, which are 33.04˚ and 31.66˚ for a (004) reflection by first calculating d_{hkl} where h, k and l are 0, 0, and 4, respectively.

The schematic of our single and double crystal x-ray diffraction set up is shown in figure 2.9 (a). It consists of an X-ray source, a single crystal X-ray diffraction system (SCXRD), manufactured by Rigaku, and a double crystal X-ray diffraction system (DCXRD), manufactured by Blake Industries Inc. A detail description of both systems is given below.

In SCXRD, only one crystal namely the sample is used. In practice, the X-ray source produces polychromatic and divergent radiation. Since only one crystal (the sample) is used, this technique is not monochromatic, because a broad range of wavelengths including the Cu$K_{\alpha 1}$ and Cu$K_{\alpha 2}$ lines that are produced by the X-ray source are present. Two broad diffraction

peaks associated with Cu$K_{\alpha 1}$ and Cu$K_{\alpha 2}$ are observed in the diffraction peaks of the epilayers. Both θ-2θ are coupled in this case. The detector is rotated twice as fast and in the same direction around the diffractometer axis as the sample, simultaneously. Sometimes the system is calibrated with respect to pure GaAs or InP crystals to optimize the X-ray performance and to obtain reliable data. Generally, based on the peak position, the lattice constant and estimated composition can be obtained for a large lattice mismatched sample. But, for a nearly lattice-matched sample, where the broad diffraction peaks are nearly overlapped, it is not possible to obtain an accurate value. In this case, high resolution DCXRD is used which is described below. Only primary information about sample quality is obtained by SCXRD.

Double crystal X-ray diffractometry is a two-crystal system as opposed to the SCXRD described above. A first crystal of pure Ge (100) is used which eliminates all but a narrow band of excitation wavelengths before the X-rays reach the sample, and minimizes the wavelength spread. An angular aperture setting is used of which the angular tilt of the aperture is controlled by the following equation-

$$\delta\theta = (h + s)/L \qquad (2.3)$$

where, h is the source size, s is the slit size and L is the distance between the source and the sample. Thus, it produces a very monochromatic radiation

around the $CuK_{\alpha 1}$, as shown in the real space geometry in figure 2.9 (b). The $CuK_{\alpha 1}$ radiation is very useful because of its convenient wavelength of 0.154 nm, which is useful for most interplanar spacings and because of its high intensity. [10] The second crystal is the sample itself. In the DCXRD system, the detector is fixed, that is, 2θ is fixed. The sample is rotated around, that is, ω is rotated around θ. This type of measurement is called a "rocking curve". Due to its high-resolution source, the peaks of the nearly lattice matched samples can be resolved easily within the arc second range. From the full width at half maxima (FWHM) we can assess the quality of the material.

Usually, a (400) reflection is convenient for a (100) substrate because it is intense and the planes are parallel to the surface. Straightforward analysis of the rocking curve Bragg separation can be made of the (400) reflection for a epitaxial layers grown on a InP (100) oriented substrate since the lattice spacing d of the Bragg formula can be given by $a_{\perp}/4$, where $a_{\perp}$ is the lattice parameter in the [100] direction. For example, figure 2.10 is a DCXRD (004) reflection spectrum of InGaAs epilayers grown on InP substrate. The strong dominant peak is the InP substrate peak and the other peak is due to the InGaAs epilayer. From the separation of the peaks we can calculate the lattice constant of the InGaAs epilayer using the Bragg formula as follows-

$(a_{InGaAs})_{\perp} = 2^* 1.5406/\sin(31.66 + \Delta\theta)$ (2.4)

where, $\Delta\theta = \Delta\omega$, and $\Delta\omega$ is the measured angular separation between the Bragg peaks. In fig.2.10, $\Delta\omega$ =185 arc sec = 0.05˚. Thus, the lattice constant of the InGaAs epilayers in the perpendicular direction is found to be 5.860 Å. Also, lattice mismatch can be calculated by using the following relation –

$(\Delta a/a)_{\perp} = (a_{\perp} - a_s)/a_s = -\Delta\theta / \tan\theta_B$ (2.5)

where, a_s is the lattice parameter of the substrate, θ_B is the Bragg angle corresponding to a_s, $\Delta\theta$ is the angular separation between Bragg peaks. From figure 2.10, the lattice mismatch can be calculated by using the above relation either by first calculating the lattice constant of the InGaAs epilayers or by calculating the $\Delta\theta$ from the spectrum. In either way the lattice mismatch in the perpendicular direction was found to be –0.14%.

The bulk lattice constant can be calculated by considering both the parallel and perpendicular lattice constant. The bulk lattice constant of the layer is-

$a_{bulk} = [(1-\nu) / (1+ \nu)]\, a_{\perp} + [2\, \nu / (1+ \nu)]\, a_{II}$ (2.6)

Usually, under matched conditions, assuming a pseudomorphic layer, the parallel lattice constant, a_{II} is equal to the lattice constant of the substrate, a_s, which is 5.8687 Å. Here, ν is the poisson ratio of the layer, which is defined as the ratio of perpendicular and parallel strain in crystal:

$\nu = - \varepsilon_{\perp}/\varepsilon_{||}$

Usually, the poisson ratios for the semiconductor films are between 0.25 and 0.35. The poisson ratio for InGaAs is 0.33. Using this value for the poisson ratio, the bulk lattice constant was estimated to be 5.864 Å.

The composition can also be calculated by assuming the validity of Vegaard's law, which is the linear dependency of the lattice constant on the alloy composition. Since the lattice constants of the ternary can be calculated from x-ray measurement, by knowing the lattice constant of the binary alloys such as InAs (6.058 Å) and GaAs (5.653Å) that comprises the ternary InGaAs, we can calculate the composition as follows-

$a_{InGaAs} = a_{InAs} * x + a_{GaAs} * (1-x)$ (2.7)

$5.864 = 6.058\ x + 5.653\ (1-x)$

Here, x = 0.52, where x is the fraction of In in the alloy. Thus, the composition of the near lattice-matched epilayers is $In_{0.52}Ga_{0.48}As$.

Unless an epitaxial layer is perfectly lattice matched to the substrate, generally its lattice will not have the same cubic unit cell as that of that substrate because as the layer grows it will adopt the lattice constant of the substrate by tetragonally distorting its lattice cell. In general, the distortion introduces strain. As the layer thickness increases, the strain builds up until it is large enough to produce misfit dislocations that allow the layer to relax.

Therefore, depending on the thickness and the elastic constant of the layer, it can be fully strained, partially strained, or fully relaxed. When the thickness of the epilayers is less than a certain thickness (critical thickness), the epilayers will be pseudomorphic (fully strained), and their structure will be tetragonally distorted as shown in fig. 2.11. For layers grown on high symmetry planes such as (100), the lattice of the epitaxial layer will be tetragonally distorted with a different lattice parameter in the growth plane, a_{II}, than in the growth direction, $a_{\perp}$. [11] When the thicknesses of the epilayers exceed the critical thickness, the epilayers first becomes partially relaxed and then fully relaxed. If the layer is partially relaxed, the parallel mismatch is not equal to zero any more, but it is still smaller than the perpendicular mismatch. In the case of a fully relaxed layer, the parallel and the perpendicular lattice mismatches are equal to each other. For the case of a tetragonal distortion, the lattice mismatch in the growth direction $(\Delta a/a)_{\perp}$, and the mismatch parallel to the interface, $(\Delta a/a)_{II}$, can be calculated from the double crystal rocking curves in terms of the separations between Bragg peaks observed on rocking curves. Generally, from the (511) a and (511) b reflection we can calculate the lattice reflection geometries with x-ray incident angle of $(\theta+\varphi)$ and $(\theta-\varphi)$, respectively, where, θ is the Bragg angle and φ is the mismatch both in the parallel and perpendicular orientation. The

subscripts a and b represent (511) reflection geometries with x-ray incident angle of $\theta+\varphi$ and $\theta-\varphi$, respectively (θ is the Bragg angle, $\varphi = 15.793$). The peak separation from (511)a is very close to the peak separation from (400). By measuring peak separations $\Delta\theta_a$ and $\Delta\theta_b$, between the substrate and the epilayer peaks, the parallel and perpendicular mismatch can be determined:

$$\Delta(a/a_s)_{\perp} = (a_{\perp} - a_s)/a_s = \sin\theta*\cos\varphi/[(\sin(\theta+(\Delta\theta_a+ \Delta\theta_b)/2)*\cos(\varphi+(\Delta\theta_b - \Delta\theta_a)/2) - 1]; \quad (2.8)$$

$$\Delta(a/a_s)_{II} = (a_{II} - a_s)/a_s = \sin\theta*\sin\varphi/[(\sin(\theta+(\Delta\theta_a+ \Delta\theta_b)/2)*\sin(\varphi+(\Delta\theta_b - \Delta\theta_a)/2) - 1]; \quad (2.9)$$

Finally, the bulk lattice constant can be accurately calculated using equation (2.6)

A double crystal x-ray rocking curve of $Be_{0.03}Zn_{0.97}Se$ grown lattice matched to (001)GaAs substrate with (004), (511) a and (511) b is shown in figure 2.12.

Another possible phenomenon that is some times associated with X-ray diffraction is the observation of thickness fringes, also called pendellösung oscillations, which indicates a very high crystalline quality of the material. These oscillations originate from the interference between two X-ray wave fields within the crystal. This phenomenon has been described

in more detail in chapter three. From these thickness fringes the thickness of the epilayers can be calculated.

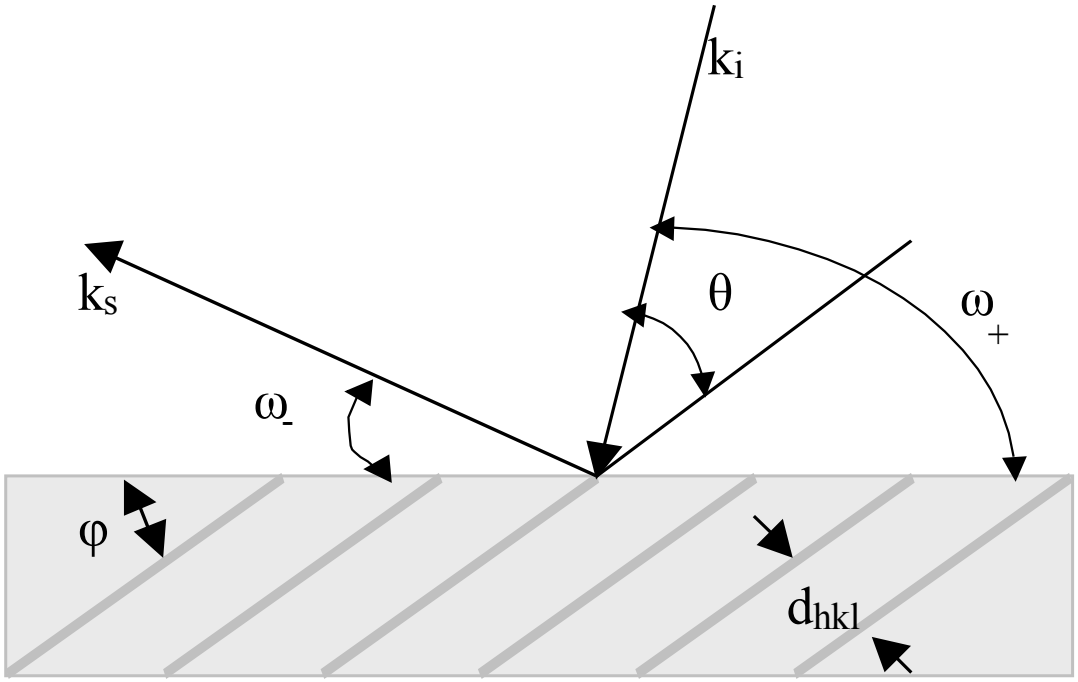

Figure 2.8 Schematic of the X-ray diffraction.

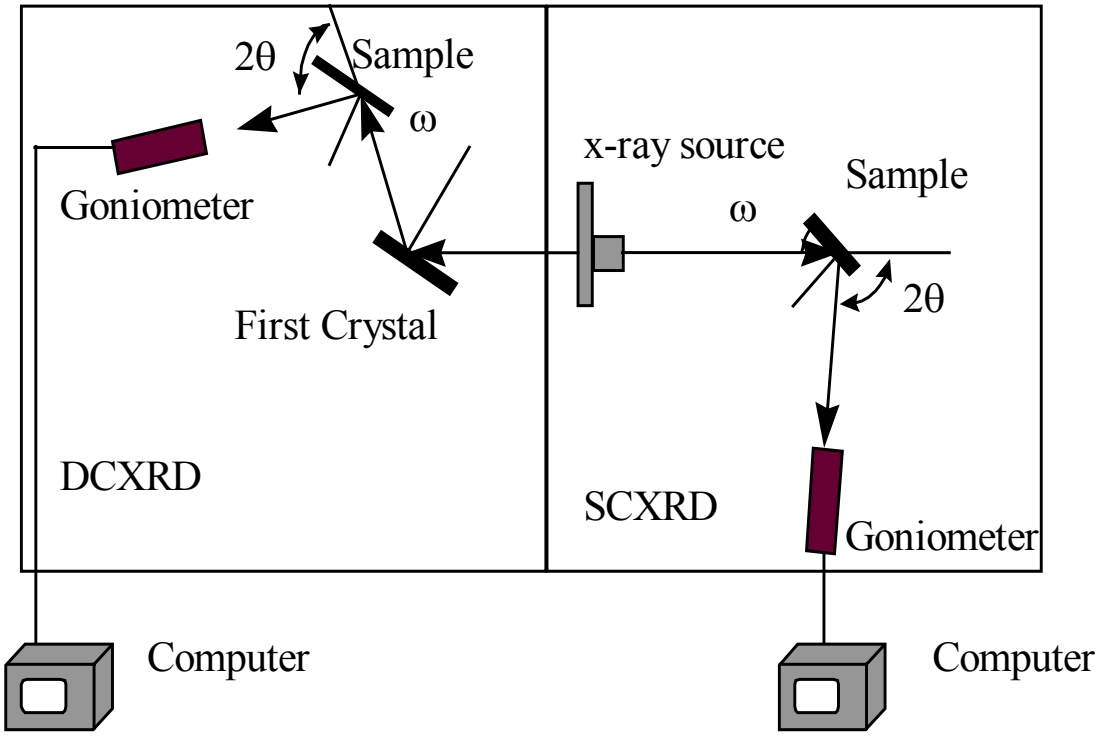

(a)

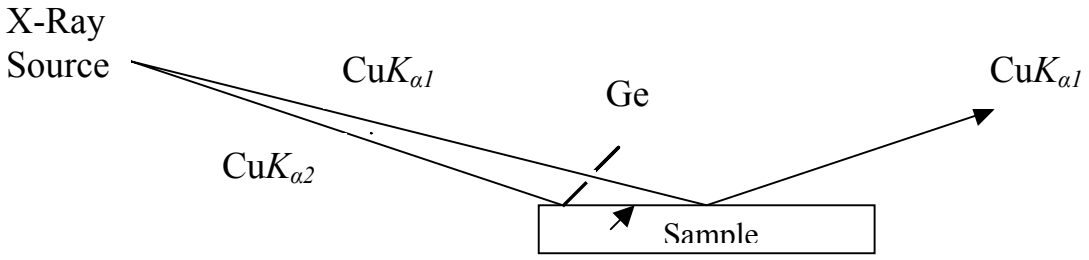

(b)

Figure 2.9. (a) X-ray diffraction system showing single and double crystal x-ray set up. (b) Real space geometry of DCXRD showing Cu$K_{\alpha 1}$ radiation.

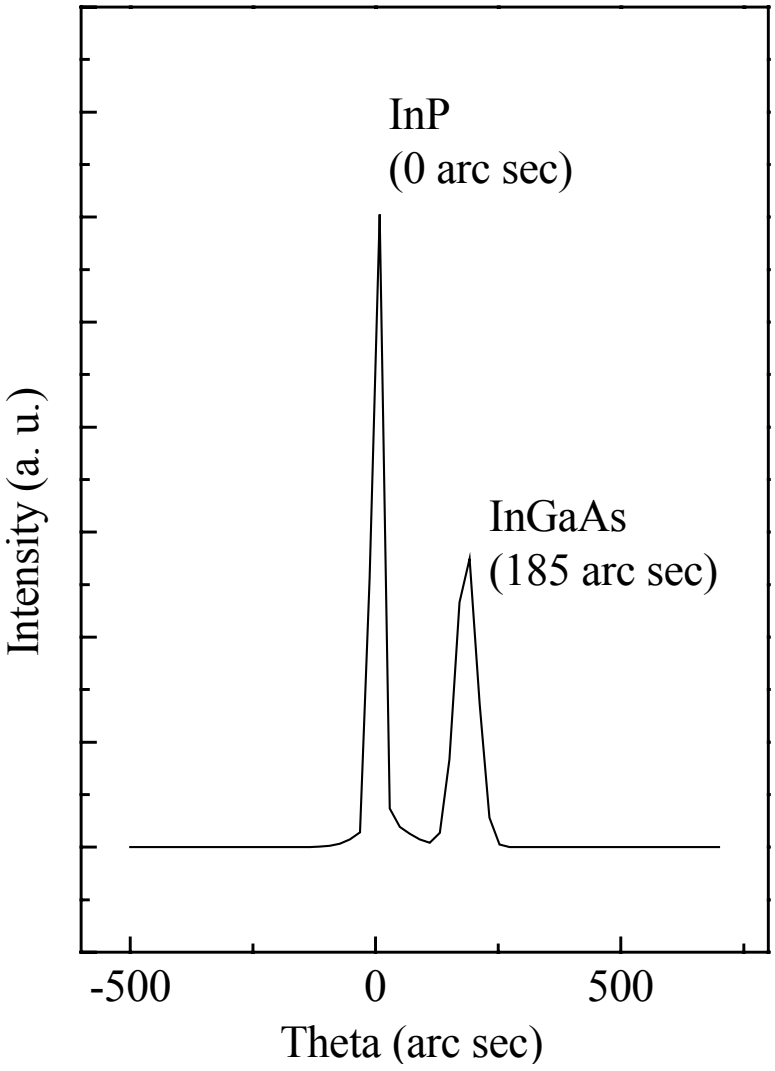

Figure 2.10. Double crystal x-ray rocking curve from an InGaAs layer grown on an InP substrate.

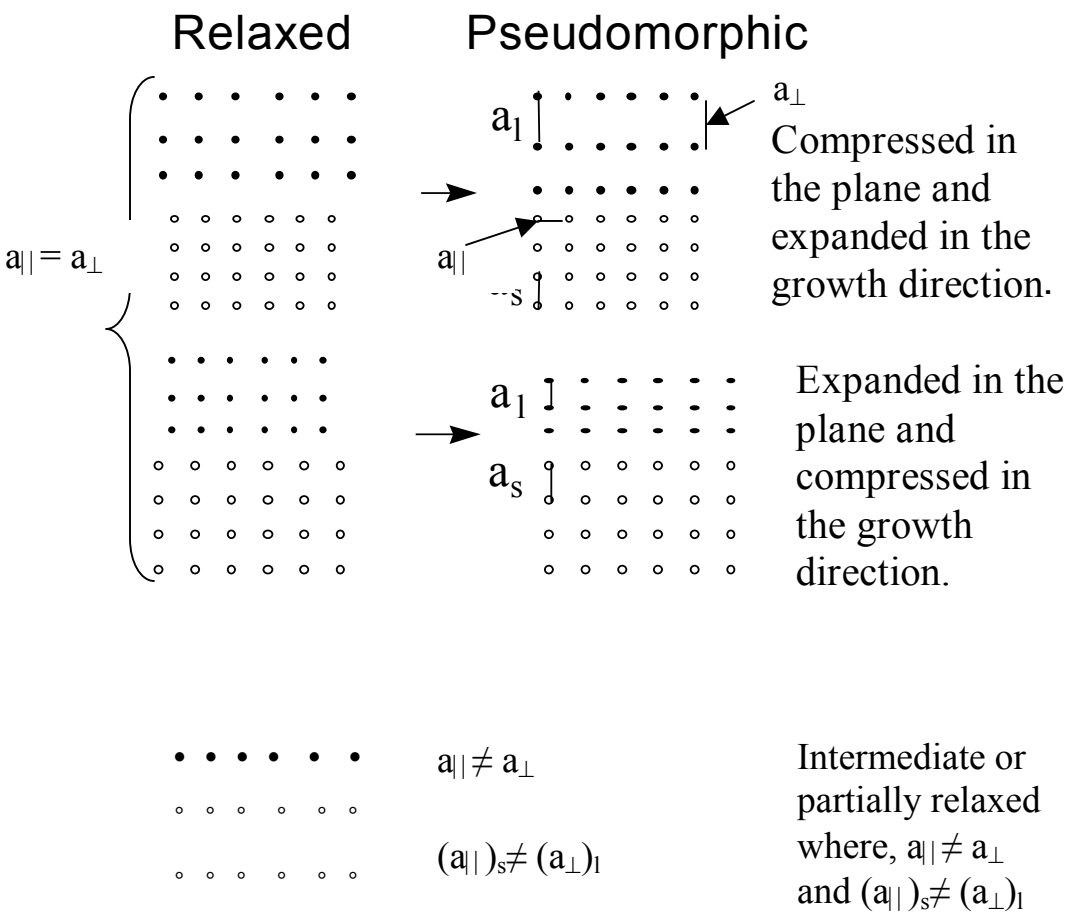

Figure 2.11. Schematic of the crystalline lattice under compressive and tensile strain

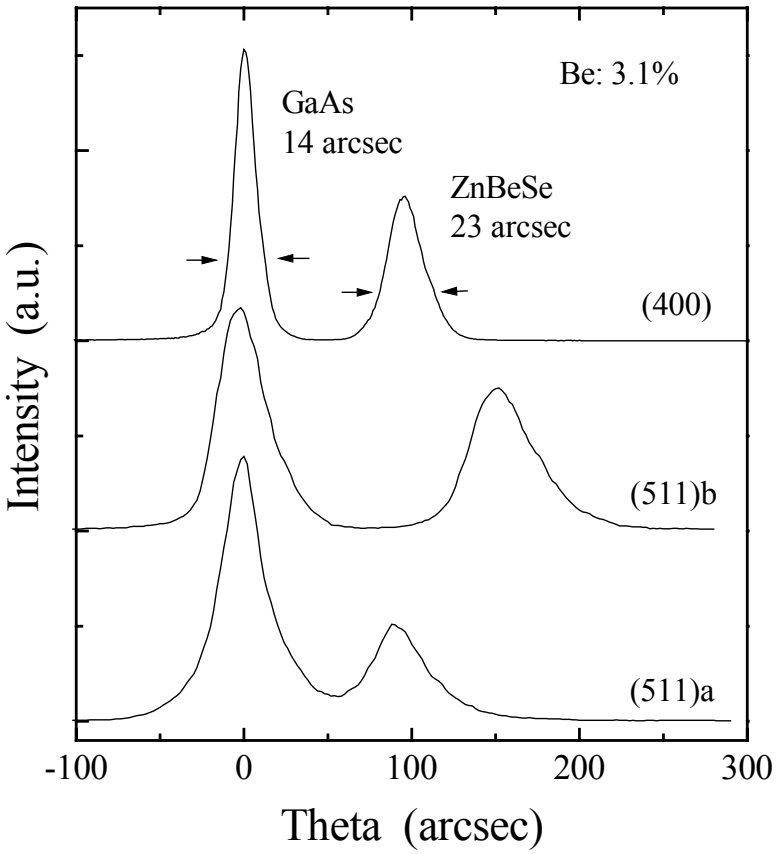

Fig. 2.12. The DCXRD rocking curves for $Be_{0.03}Zn_{0.97}Se$ epilayers on GaAs substrate showing (400), (511) a and (511) b rocking curve.

2.4. Photoluminescence

Photoluminescence (PL) is the spontaneous emission of light from a material under optical excitation. PL is one of many widely used methods, both to understand the fundamental recombination process in the alloys as well as to characterize it for its quality. It is a very sensitive method to detect optical transitions from an excited electronic state to a lower one, usually the ground state. If several excited states exist, only the transition from the lowest excited states can normally be observed. Usually, for direct bandgap semiconductors, the dominant luminescence emission is a radiative recombination between the conduction band and the valence band. In this work we have characterized the optical properties of the epilayers using PL to asses the quality based on their photoluminescence properties.

Radiative recombination occurs when the semiconductor is under a non-equilibrium condition i.e., excess electron-hole pairs are created in the material by some external excitation to cause departure from equilibrium and return to equilibrium occurs by the recombination of the excess carriers. Usually electrons are excited by the absorption of light from the valence band to the conduction band. The excited electrons reach the conduction band minimum and recombine with the holes in the valence band. During this radiative recombination process, the excitation may involve a direct

transition, where materials have the minimum of the conduction band above the top of the valence band, that is in the same point of *k*-space, or indirect transition where the minima and maxima occurs in different points of the *k*-space as shown in figure 2.13. For example, in ZnSe the excitations occur through direct transitions where electron does not change the wave vector and k = 0 and the material is defined as direct band gap material. Momentum needs to be conserved in this absorption process, since photons have very small momentum, $k_e = k_h$. In the case of an indirect gap material such as BeTe, the transitions require both energy and momentum. This case, $k \neq 0$ and electrons change their wave vector during excitations. This transition require phonon cooperation to conserve momentum and $k_e = k_h \pm q$, where q is the phonon wave vector. This is a two-step process since the photon cannot provide a change in momentum. Since this is a multi-step process, indirect transitions have lower probability to occur than the direct transitions.

Relaxation of the excess carrier density occurs by one of the many ways described in Fig. 2.14, where optical absorption is compared with the photoluminescence process. There is a band-to-band (B-B) recombination of an electron in the conduction band with a hole in the valence band as shown in figure 2.14 a. Radiative recombination can also occur via shallow

impurities. Ionized donors and acceptors have a large capture cross section for the photo excited electron and holes, respectively. If the captured electron recombines with a free hole in the valence band, a donor to valence (D-V) occurs (Fig. 2.14 b). Similarly recombination between the captured holes with a free electron in the conduction band gives conduction band-to-acceptor (C-A) transition (Fig 2.14 c). Both D-V and C-V transitions are referred to as free to bound transitions. There are also donor-to-acceptor (D-A) pair transitions where two bound particles recombine with each other (Fig. 2.14 d). These transitions are radiative. Transitions that recombine via a deep center are likely to be nonradiative. Another nonradiative phenomenon occurs when three particles are involved which is known as band-to-band Auger recombination process. In this case the energy released by an electron-hole recombination kicks a third electron deep in the conduction band. All these pathways can be identified by using temperature and intensity dependent measurements. Band structure, band gap, epilayers properties, phonon properties can be obtained from these measurements. [12] Radiative transitions in semiconductors involve localized defect levels. The photoluminescence energy associated with these levels can be used to identify specific defects, and the amount of photoluminescence can be used to determine their concentration.

Some of the advantages of PL are that it is a non-destructive technique and it requires very small amount of material and environmental control. Because the samples are optically excited, it doesn't require any electrical contacts or junctions and high resistive material can be used without any difficulty. Finally, it is sensitive to the chemical species of impurities, which can be detected even at very low densities.

The schematic of the PL system is shown in figure 2.15. A very small piece (2mm x 2mm) of the sample is mounted on the cold finger of Janis cryogenic system. Then the cold finger is pumped down to ~ 10^{-5} torr. Based on the requirement of the experiment, the cold finger can be cooled down to 5.8K using liquid helium or 77K using liquid nitrogen. In order to control the temperature between 5.8K and 300K, a heater is installed in the back of the cold finger and the desired temperature can be set with the aid of a controller. A He-Cd laser with an excitation wavelength of 325 nm is used as an excitation source, which has large enough energy to excite electrons in most of the wide bandgap materials of our interest. The laser beam passes through the chopper, which converts the beam to a periodic ac signal, which is then focused on the sample by aligning the cold finger. The laser intensity can be controlled by placing neutral density filters between the laser and chopper. The luminescence produced by the sample due to the excitation is

collected by a concave lens and converted to a collimated beam. The collimated beam is focused on the first entrance slit of the SPEX 1680-B spectrometer and passes through the second exit slit to a photomultiplier and is converted to an electrical signal. The ac signal is then fed to a lock in amplifier to be amplified. The amplified signal is collected into the data scan, which is connected, to the computer to be analyzed.

Figure 2.16 shows the 77 K PL spectra of two ZnCdSe bulk layers grown nearly lattice matched to InP substrate. In figure 2.16 (a) the PL spectrum exhibits a deep level emission at ~ 1.8 eV, which is known to be due to defects near the interface of the substrate and epilayers and indicates a poor quality of the sample. Deep levels originate when an electron in the defect level of the semiconductor is trapped near the defect. Such electrons cannot participate in current flow very easily. That is why it is important to avoid deep level defects as much as possible in semiconductors. Fig. 2.15 (b) illustrates a high quality PL spectrum that exhibits only band-edge emission. The full width at half-maximum of this sample is also consistent with good material quality.

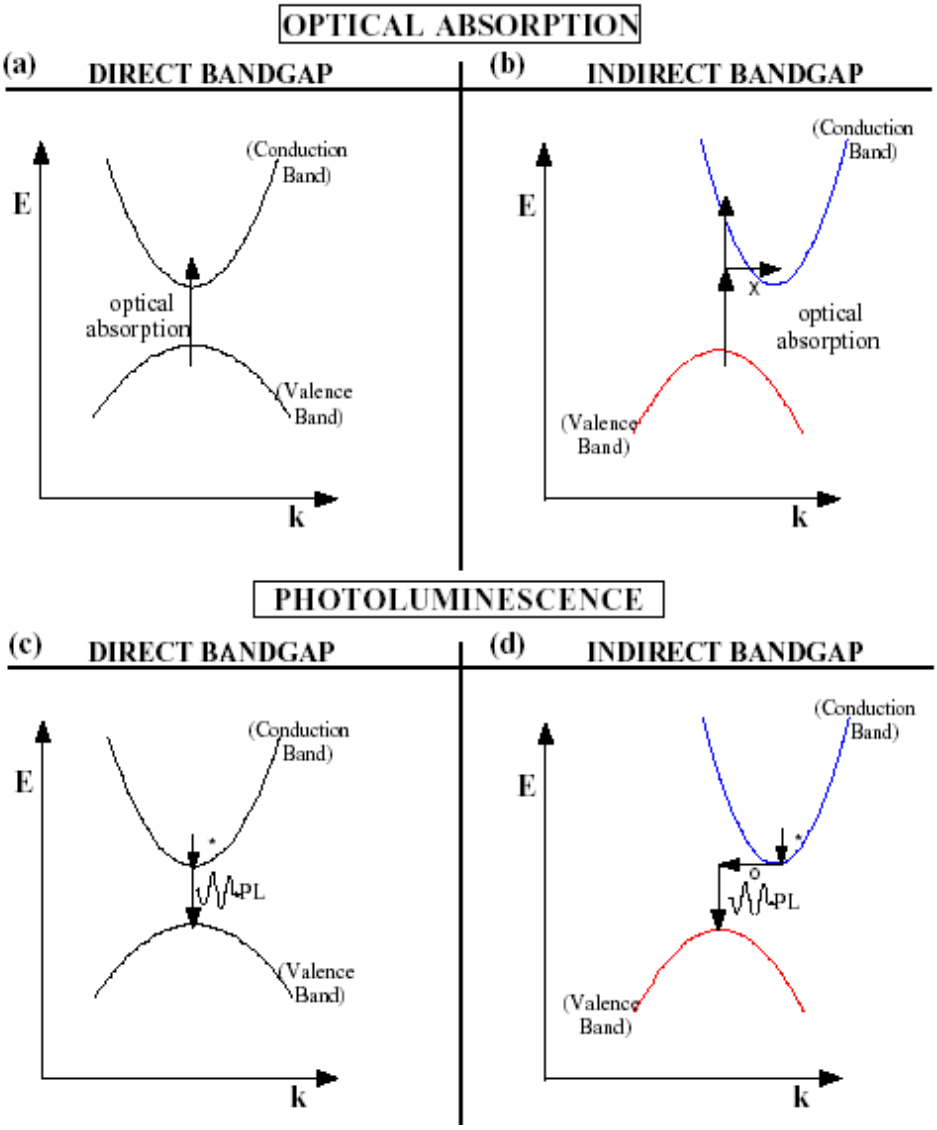

Figure 2.13. The energy band diagram: (a) and (b) represents optical absorption, (c) and (d) represents photoluminescence. Also, figure (a) and (c) represents direct bandgap semiconductor; figure (b) and (d) represents an indirect bandgap semiconductor. (Ref. 3)

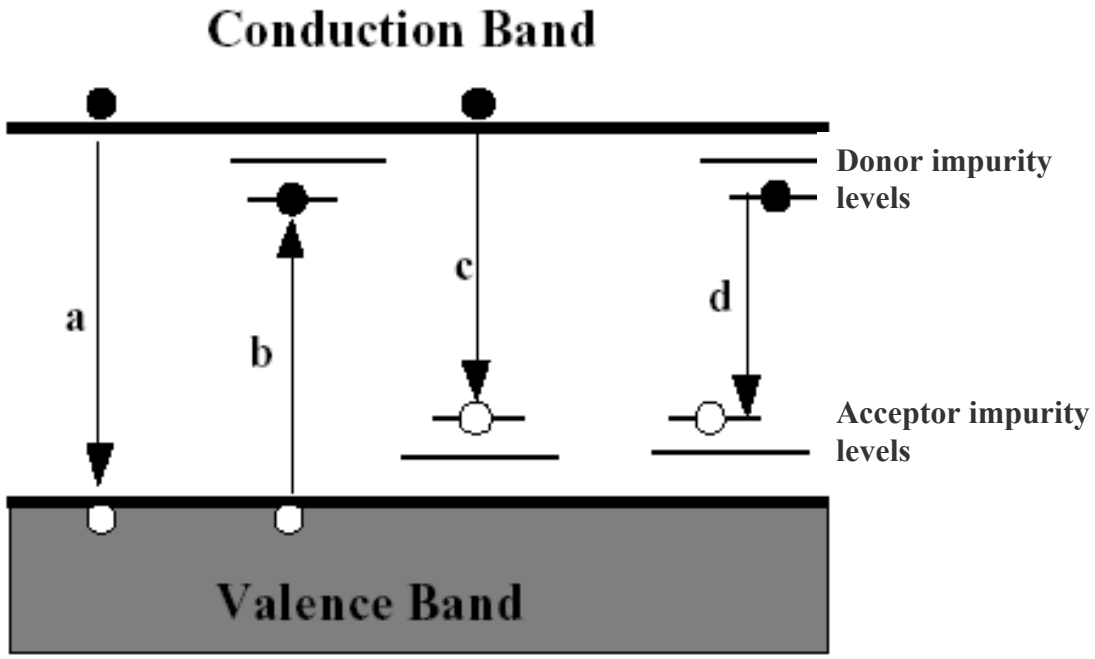

Figure 2.14. Radiative transitions: (a) simple electron-hole band to band recombination (B-B) (b) defect-band involving donors (D-B), (c) defect-band involving acceptors (C-A), (d) donor-acceptor pair (D-A).

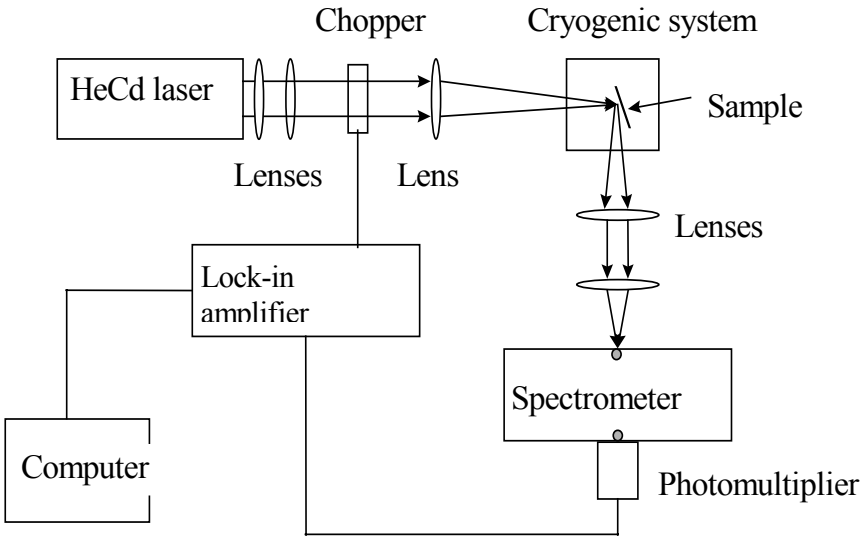

Figure 2.15 Illustration of photoluminescence set up.

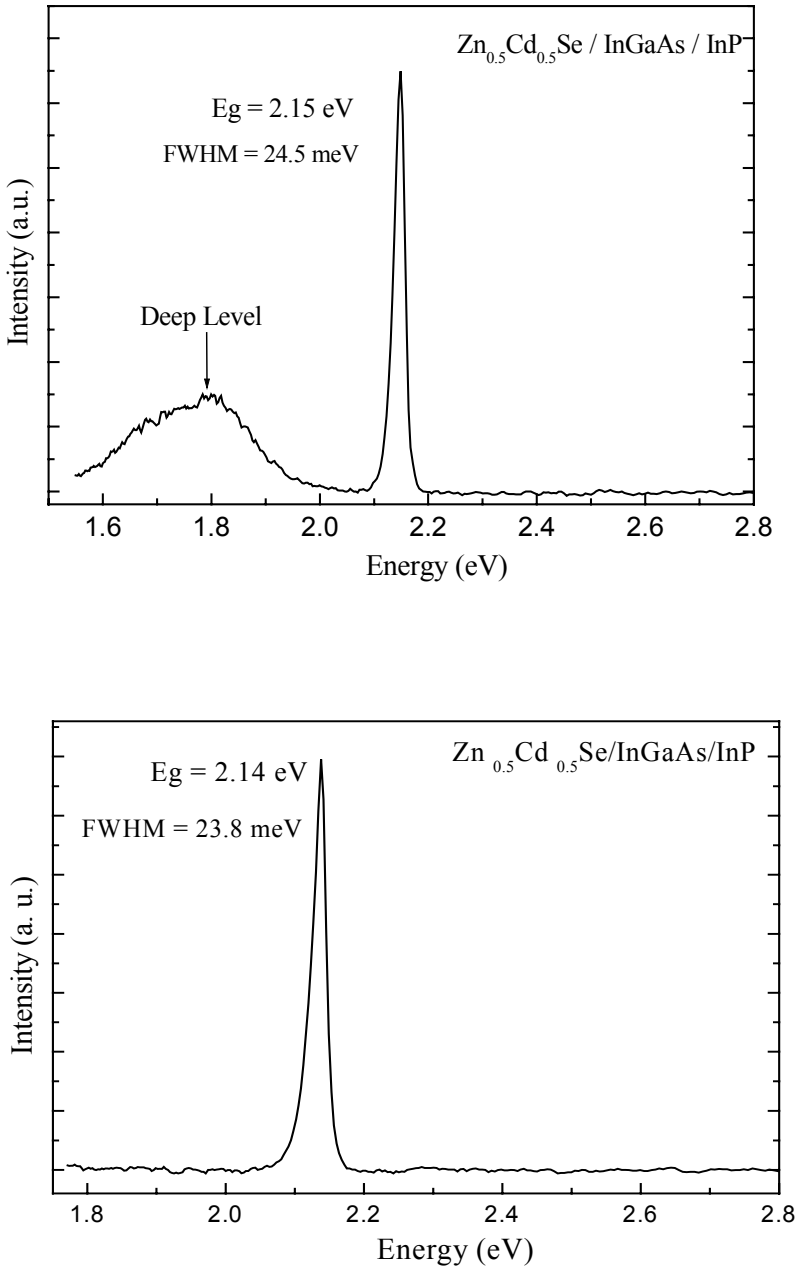

Figure 2.16. PL spectra of nearly lattice matched ZnCdSe/InGaAs/InP (a) with deep level emission, (b) sample with no deep level emission, indicating good quality of the sample.

2.5. Reflectometry

Reflectometry is a non-destructive technique that is used to study energy levels, bandgap, indices of refraction and thickness of semiconductor thin films. This technique is not very sensitive to material quality as in the case of photoluminescence. Since the reflectance technique is based on absorption, the direct bandgap of indirect semiconductor materials can be measured easily, which is not always so in PL, which is based on emission.

Reflectance is the ratio of the intensity of the outgoing light compared to that of incident light. It is often difficult to measure the incident light directly. So, the incident light is usually measured by reflecting the light from a reference. As can be seen in figure 2.17, when the film is semitransparent, and thus more than one interface is present, such as substrate and a thin film, the resultant reflected beam returning to medium 1 (air) consists of the light which is initially reflected from the first interface as well as the light that is transmitted by the first interface (air/ZnMgSe) and reflected from the second interface (ZnMgSe/InP) and then transmitted by the first interface and going in the reverse direction. Each successive transmission back into medium 1 is smaller than the last transmitted one. Finally, the infinite series of these waves makes up the resultant reflected

wave. For a single film with two interfaces (air/ epilayers/substrate) the total reflectance R, is expressed by-

$$R = (ax + b/x - 2abcos2\delta)/(ex + a^2b^2x - 2abcos2\delta) \quad (2.10)$$

Where,

$x = e^{\alpha d}$,

$a = ((n-1)^2 + k^2)/ ((n-1)^2 + k^2)^{1/2}$,

$b = ((n-n_0)^2 + k^2)/ ((n+ n_0)^2 + k^2)^{1/2}$

$\alpha = 4\pi k/\lambda$ is absorption coefficient, d is the epilayer thickness, and $\delta = 2\pi nd/\lambda$, and k is the extinction coefficient.

Figure 2.18 is the reflectivity spectrum of a ZnMgSe epilayers grown on InP substrate. In the lower energy region where $h\nu < Eg$, is a transparent region where the epilayers do not absorb light. In this region, k vanishes and $\alpha d = 0$. In the mid region where $h\nu \approx Eg$, is the transition region where epilayers start to absorb light. In this region, $k < n$ and $\alpha d \sim 1$. The high energy region of the spectra where $h\nu > Eg$ is the highest absorption region. In this region $k > n$ and $\alpha d > 1$. It could be possible to identify higher energy critical points in this region. For thick layers, the point at which the oscillations begin (i.e., the point at which the film becomes transparent) can be identified as the bandgap of that material.

A thick transparent film usually has many interferences oscillations that can be identified in the reflectance measurement. The thickness of the film can be calculated from these oscillations by Fourier analysis of the experimental reflectance data. [13] Some conditions must be assumed, such as the films refractive index is assumed to be constant over some spectral range so that it can be ignored during calculation. So the interference oscillation due to the film in that spectral range will have a period, which is constant. A Fourier analysis of these data yields a peak at a single frequency. This frequency is proportional to the optical thickness of the film. The optical thickness is defined as the physical thickness multiplied by index of refraction of the film. Thus, thickness of thin film can also be calculated by reflectance measurement.

A simple single-beam reflectometer schematic is shown in figure 2.19 (a). In this system, a light beam from the light source is incident in a beam splitter. Part of the beam is reflected down through the focusing lens and imaged on to the sample through the lens. The beam is reflected back from the sample and passes through the focusing lens again. The part of the beam, which is transmitted through the beam splitter, enters the detector, which measures the intensity.

A Cary 500 UV-Visible Spectrophotometer with a Variable Angle Specular Reflectance accessory was used in this research. The accessory features a dual ‘V-W’ configuration, with one spherical mirror (S1) and two toroidal mirrors (T1 and T2) per beam as shown in figure 2.19(b). The spherical mirrors mounting are movable which allows them to be used for both calibration and sample measurement. These same optical components are in the light path during both calibration and measurement During experiment, when a sample is mounted, the only change in the system is due to the reflectivity of the sample.

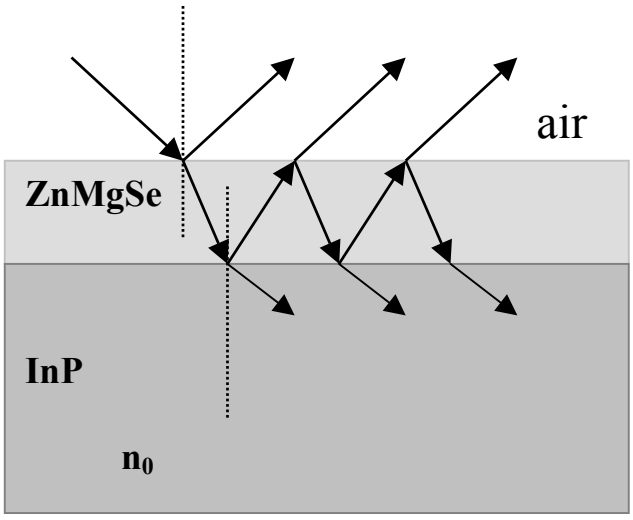

Fig. 2.17. Schematic of a ZnMgSe epilayers grown on an InP substrate. Reflections and transmissions for two interfaces are shown. The resultant reflected beam is made up of the specular beam and the infinite series of beams, which are transmitted, from ZnMgSe back into air.

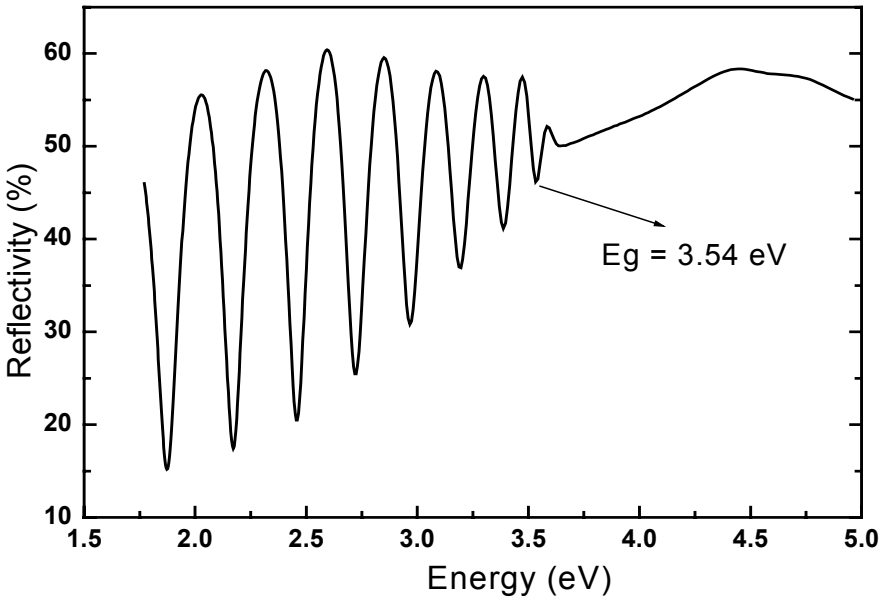

Fig. 2.18. Reflectivity spectrum of a ZnMgSe epilayer grown on InP substrate.

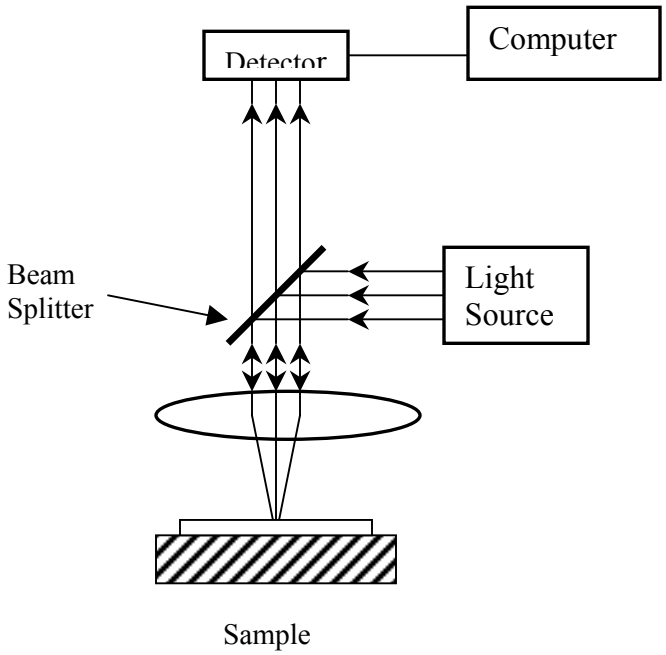

Fig. 2.19 (a) A simple single beam reflectometer.

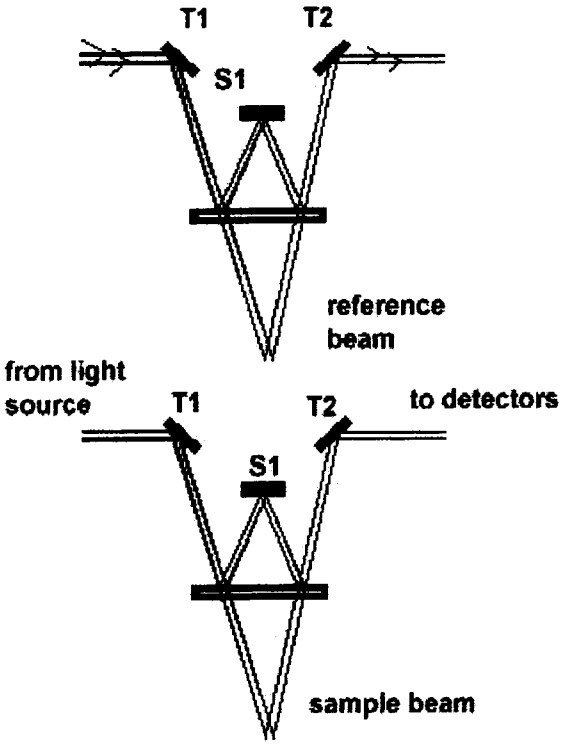

2.19 (b) Geometry of the variable angle specular reflectance accessory .

2.6 Modulation Spectroscopy

Modulation spectroscopy is a powerful and versatile optical technique for the study and characterization of a large number of semiconductor systems including bulk and thin films, microstructures including quantum wells, super lattices, quantum dots, surface interfaces and actual device structures. [14] Modulation spectroscopy is an analogue method for taking the derivative of the optical spectrum such as reflectance or transmittance of a material by modifying the measurement conditions. [15-18] The spectral response of a sample can be modified directly by applying a repetitive perturbation such as an electric field (electro modulation), a heat pulse (thermo modulation), or stress (piezomodulation). The periodic variation of the measurement conditions gives rise to sharp, differential-like spectra in the region of interband or intersubband transitions. Thus, modulation spectroscopy emphasizes relevant spectral features and suppresses uninteresting broad background effects. The ability to perform a line shape fit is one of the advantages of the modulation spectroscopy. Since for the modulated signal the features are localized in photon energy, the line shapes yield accurate values of energies and broadening parameters of interband transitions.[9] For example, figure 2.20 shows a direct comparison of the reflectivity and electric-field modulated reflectance (electroreflectance)

spectra of bulk GaAs at 300K. [19] The room temperature reflectivity is characterized by broad features and very basic information such as band gap, indices of refraction can be extracted from the spectra. But the electroreflectance has zero as a base and is dominated by a series of very sharp, derivative like features corresponding to specific transitions in the Brillouin zone. The electric field modulated spectra of GaAs is also shown in the bottom part figure 2.20. In modulated signal the features are localized in photon energy. By performing a line shape fitting to the spectra accurate values of the energies and broadening parameters of the interband transitions can be obtained. In figure 2.20, it is possible to determine the energies of the E_0, $E_0 + \Delta_0$, E_1, $E_1 + \Delta_1$ peaks within a few meV at room temperature. Also, if interested, other modulated variables such as phase, modulated frequency, modulated amplitude can also be determined from the spectra.

2.6.1 Contactless electroreflectance (CER)

Electromodulation such as contactless electroreflectance (CER) is a modulated technique that measures the changes in optical reflectance of a material with respect to applied electric field. [20] In this technique the spectral response can be modified by applying the electric field. Very sharp and well-resolved derivative like features can be observed as a result of the applied

perturbation, which can be assigned of different transitions based on the properties of the material. This method utilizes a condenser-like system with the top electrode being either (a) a thin transparent conductive coating of indium-tin-oxide or Au or Ni metal on a transparent substrate such as glass, quartz etc. or (b) a wire grid. [21-22] A second electrode consisting of a metal strip is separated from the first electrode by an insulating spacer. The sample is placed between these two capacitor plates. The dimension of the spacer is such that there is very thin layer (~0.1 mm) of air or vacuum between the front surface of the sample and the conducting part of the first electrode. Thus, there is nothing in direct contact with the front surface of the sample. Figure 2.21 shows the sample holder and electrode arrangement that is used in the contactless electroreflectance measurement in our lab.

Figure 2.22 is a schematic diagram of the complete CER set up at City College. Light from an appropriate light source (xenon or tungsten lamp) passes through a monochromator. The exit intensity at wavelength λ, $I_0(\lambda)$, is focused on the sample by means of a lens. The electro modulation is applied to the sample at frequency Ω_m. The reflected light is collected by a second lens and is focused on an appropriate detector such as photomultiplier tube or a photo diode. The light striking the detector contains two signals: the d.c. and the a.c signals. The d.c. component of the

light is given by $I_0(\lambda)R(\lambda)$, where $R(\lambda)$ is the d.c. reflectance of the material, while the modulated value is $I_0(\lambda)\Delta R(\lambda)$, where $\Delta R(\lambda)$ is the change in reflectance due to the applied high electric field modulation. The a.c. signal from the detector, which is proportional to $I_0\Delta R$, is measured by a lock-in amplifier. Typically, $I_0\Delta R$ is in range of 10^{-4} to 10^{-6} of I_0R because optical response is very small.

In order to evaluate the quantity of interest, for example the relative change in reflectance $\Delta R/R$, a normalization procedure is used to eliminate the uninteresting common feature $I_0(\lambda)$. In figure 2.22, the normalization is performed by a variable neutral density filter (VNDF) connected to a servo mechanism. The d.c. signal from the detector, which is proportional to $I_0(\lambda)R(\lambda)$, is introduced into the servo, which moves the VNDF in such a manner as to keep $I_0(\lambda)R(\lambda)$ constant, i.e. $I_0(\lambda)R(\lambda) = C$. Under these conditions the a.c. signal $I_0(\lambda)\Delta R(\lambda) = C\ \Delta R\ (\lambda)/R(\lambda)$. Thus, the signal to the lock-in amplifier is proportional to the quantity of interest, i.e. $\Delta R(\lambda)/R(\lambda)$. We used electro reflectance measurement to identify transitions within quantum wells of interest.

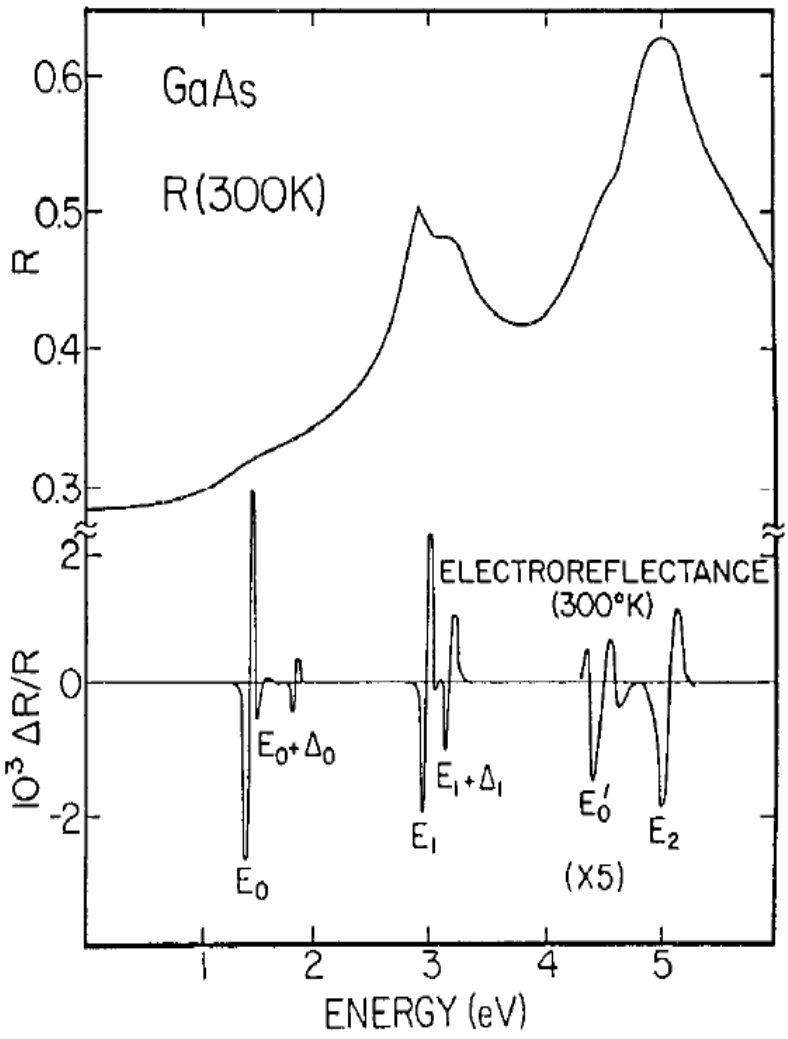

Figure 2.20. Comparison of room temperature reflectivity and electric field modulated reflectivity of GaAs.

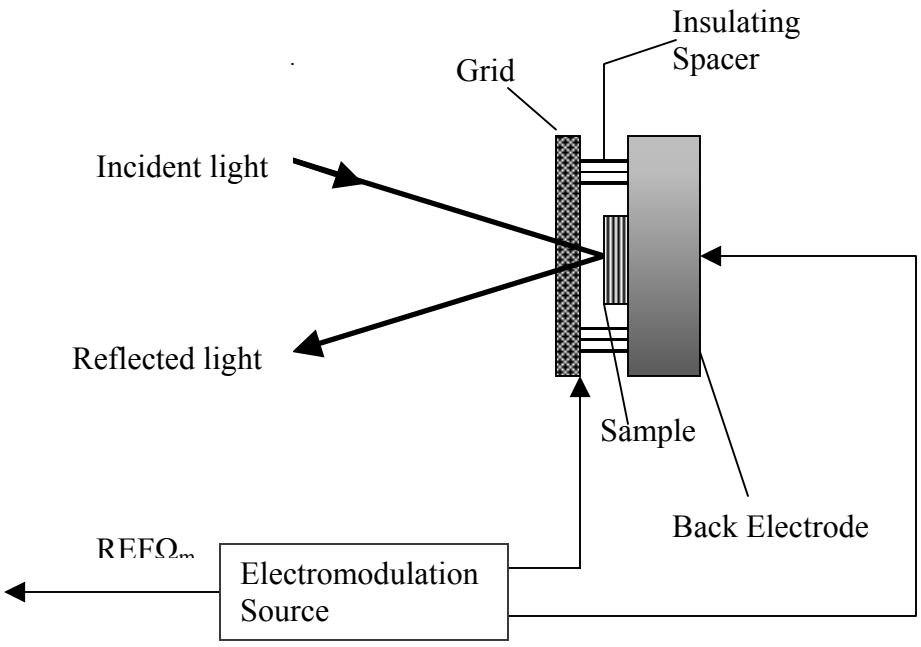

Figure 2.21. Schematic view of the condenser-like arrangement (sample holder) used in the contactless electroreflectance setup.

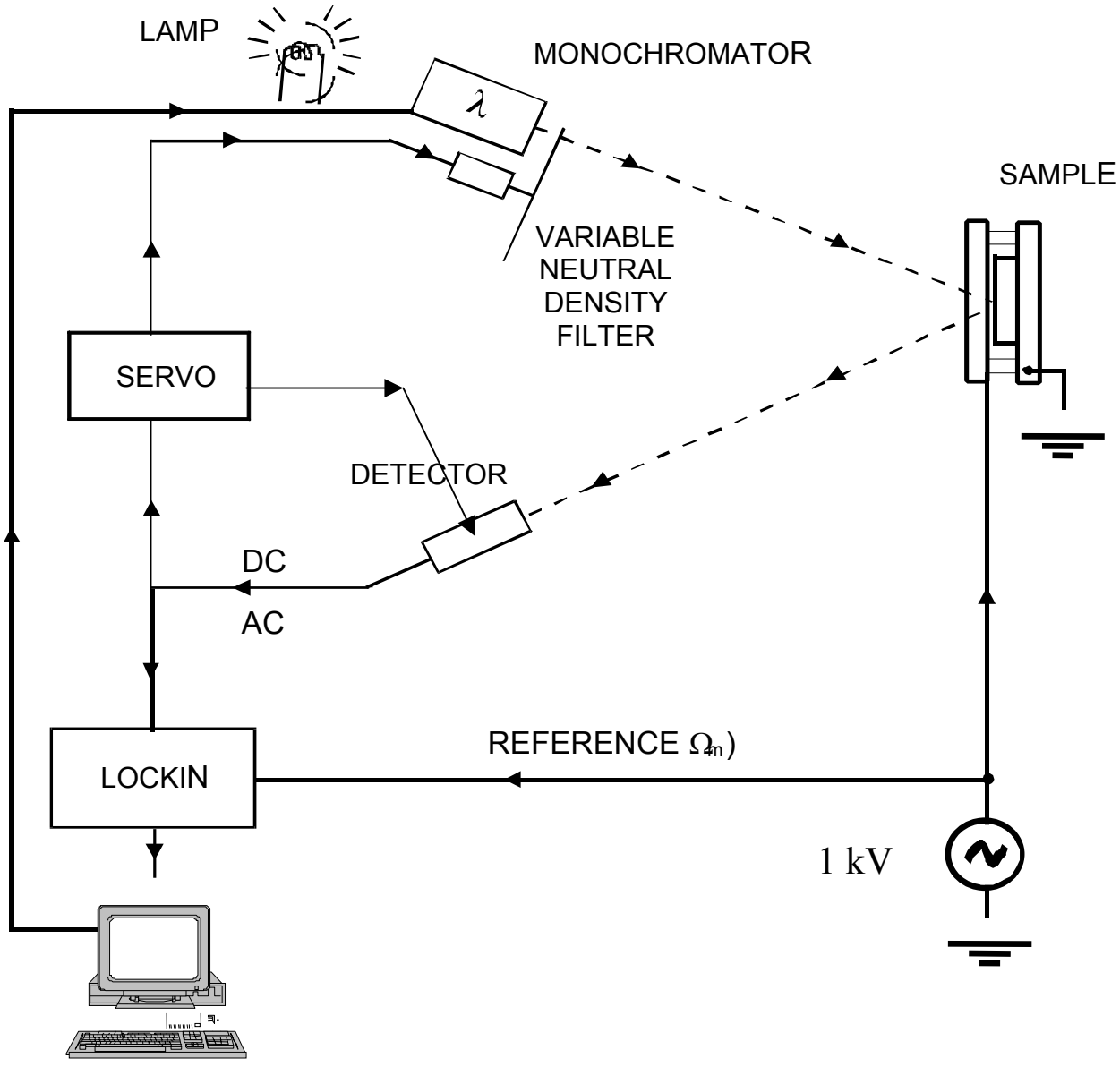

Figure 2.22. The schematic of the contactless electroreflectance setup.

Chapter 3

Growth and characterization of zincblende ZnMgSe on InP substrates by Molecular Beam Epitaxy

3.1 Introduction

Since the first demonstration of the quantum cascade lasers (QCLs) in 1994 by Faist et al. at Bell Labs, interest in intersubband devices has grown considerably. [1] Among the most relevant parameters for the intersubband devices are the band offsets, which determine the emission wavelengths that can be obtained in devices such as QCLs. Even though significant scientific advances have been achieved in the development of the QCLs, there are still many limitations of these lasers. A critical one is the unavailability of mid-IR QCLs operating in continuous wave (CW) mode at room temperature (RT). Another is the absence of QCLs operating at short wavelengths, such as λ=1.55μm, needed to develop ultra fast optical communications. Both limitations are related to the relatively small conduction band discontinuity present in the most frequently used systems based on GaAs and InP, which imposes the shortest wavelength limit of 8μm [2] and 3μm [3], respectively, for QCLs made from these materials. In order to overcome these limitations studies of intersubband transitions have been recently extended to other

systems. Quantum wells (QWs) of GaN/AlGaN with IS transition wavelengths as short as 1.4 μm have been demonstrated. [4 -5] InAs based QCLs have been demonstrated in the 4 μm region in the InAs/InGaSb/AlSb system, and low temperature GaSb substrate based QCLs have been demonstrated at a wavelength of ~ 3.9 μm. [6-7] Si based Si/SiGe QCLs have also been demonstrated in the wavelength range of ~8 μm. [8] In II-VI compounds QCLs from (CdS/ZnSe)/BeTe quantum wells have been demonstrated at the wavelength of 1.62 μm. [9-12] In this regard, the growth of III-nitride multiple layer structures is especially challenging due to the lack of a lattice-matched substrate, which produces serious concerns about their crystalline quality in particular when structures made up of tens of layers are needed for these devices. Furthermore, as mentioned above, a small conduction band discontinuity limits the GaAs and InP based QCLs for shorter wavelength, below 3μm. In order to overcome the limitations mentioned above, and to obtain QCLs operating in the 1.55μm for ultrafast optical communications, it is useful to investigate new material systems with large conduction band offsets.

Mg-based II-VI materials are of considerable interest for the fabrication of optoelectronic devices. This is because their band gaps can be controlled as a function of Mg concentration, offering a tuning of the optical

confinement. [13] Our group investigated the growth of visible light emitters using ZnCdMgSe alloys lattice matched to InP substrates. The lattice-matched compositions of this alloy system can be tuned between 2.1 and 3.3 eV. Using ZnCdMgSe with a bandgap of 2.8 eV, our group has reported the conduction band offset (CBO) of a $Zn_{0.53}Cd_{0.47}Se/Zn_{0.27}Cd_{0.23}Mg_{0.50}Se$ single QW structure which yielded a band offset of 0.59 eV at RT measured using contactless electroreflectance (CER). [14]

Blue-green laser diodes (LDs) have been demonstrated using ZnMgSSe as a cladding layer on lattice matched GaAs substrate. [15] The wide bandgap ZnMgSe ternary material borders ZnMgSSe, and its study helps to determine the structural and electronic properties of the quaternary. Recently, particular interest has evolved in the ZnMgSe alloy due to its direct band gap and potential application as a cladding layer for optical devices in the blue region. [16] The $Zn_{(1-x)}Mg_xSe$ alloys have been grown on GaAs substrates [17-19] on InAs substrates [20] . It has been reported [19, 21] that $Zn_{(1-x)}Mg_xSe$ with more than 40% Mg undergoes a phase transition from zincblende to rock salt, so that the maximum band gap of the zincblende phase layers grown on GaAs reported by these authors is about 3.1eV. As can be seen from figure 3.1, where the ZnMgSe is shown by the bold line, the use of an InP substrate is an alternative to further increase the bandgap of

zincblende $Zn_{(1-x)}Mg_xSe$ up to ~3.62 eV when grown nearly lattice matched to InP. This high bandgap will make it attractive as a cladding layer for even higher carrier confinement.

3.2. Experimental Techniques

Most of the InP substrates used were epi-ready, obtained from AXT. If required, the substrates were *ex-situ* chemically degreased and etched. The degreasing was done by boiling the substrates in the trichloroethylene (TCE), acetone, and methanol, sequentially. Then, a solution of H_2SO_4:H_2O_2:H_2O (4:1:1) was used for etching the substrates. The substrates were flushed in deionized water and blown dry with ultra high purity nitrogen gas. Then the substrates were mounted on a pre-cleaned molybdenum block with indium and promptly introduced to the loading chamber of the MBE system.

For the growth of II-VI materials on III-V substrates, the II-VI/III-V interface is an important aspect. The II-VI/III-V interface is very difficult to control in the growth of II-VI materials on InP substrates because the congruent evaporation temperature of InP is low compared to the InP deoxidation temperature, [22] so it is hard to get a clean and smooth surface with correct the stoichiometry. For this reason it is also difficult to initialize

the II-VI growth directly on the InP substrate in a two dimensional growth mode at the optimized growth temperature. It was found that improved and atomically flat best surface quality can be achieved by depositing an InP or InGaAs buffer layer in the III-V chamber after the deoxidation. [23-24] After the InGaAs buffer layer growth, the RHEED shows a streaky (2 x 4) surface reconstruction, indicating the formation of As terminated atomically flat surface.

After transferred from the III-V chamber, the growth of an initial low temperature (LT) II-VI layer is performed. This is expected to reduce the reaction between Se atoms and In or Ga atoms and allow an ordered II-VI epilayers to deposit on the III-V surface. Dai et al. found that it is very important to grow low temperature (170 ºC) ZnCdSe in order to obtain initial two- dimensional (2D) nucleation. [25] Furthermore, a detailed study by Zeng et al. showed that, by depositing a low temperature ZnCdSe initial layer the quality of the full width at half maxima (FWHM) of both the PL and X-ray improved dramatically as opposed to using a LT ZnCdMgSe quaternary layer during growth of the bulk quaternary ZnCdMgSe layers. Also, the etch pit density (EPD) decreased from 10^9 cm^{-2} to $10^6 cm^{-2}$. The RHEED pattern remained streaky in both cases. [26]

Zeng et al. also showed that exposure of the Zn flux (Zn irradiation) prior to the growth of the LT ZnCdSe buffer layer in the II-VI chamber further helps to avoid interaction of Se with the III-V surface. It was found that by using Zn irradiation along with a low temperature ZnCdSe buffer the EPD of the ZnCdMgSe bulk layer was reduced to the mid- $10^4 cm^{-2}$, a value consistent with device quality material.

3.3 Growth of ZnMgSe alloys

All the samples discussed in this thesis were grown on InP (001) substrates by molecular beam epitaxy (MBE) using a dual chamber Riber 2300P MBE system that includes one chamber for the growth of As based III-V materials and another for the growth of wide gap II-VI materials, the two connected by ultra high vacuum (UHV) transfer modules. The detail of the chamber and cell preparation procedure prior to growth is described in chapter 2. Prior to the growth, the growth chambers are cooled down to the desired background pressure with liquid nitrogen. The growth process is actually initiated with the introduction of the sample in the III-V chamber for oxide desorption. Oxide desorption of the InP substrate was performed thermally in the III-V chamber by heating to 500°C under an As flux. Deoxidation of the substrate and growths were monitored *in situ* by

reflection high-energy electron diffraction (RHEED). Then a lattice matched InGaAs buffer layer of ~0.1 μm was grown, exhibiting a streaky (2x4) RHEED pattern throughout the growth. The substrate with the buffer layer was transferred to the II-VI chamber via the UHV transfer module. The growth of the epilayers in the II-VI chamber was performed under Se rich conditions. The VI to II flux ratio was between ~ 5-6. The beam equivalent pressure (BEP) ratio of Zn to Mg was ~1.77. The growth was initiated at 170°C in the II-VI chamber with a 40 seconds exposure of the InGaAs (2x4) surface to the Zn flux (Zn-irradiation) prior to initiating the growth. This step is useful to avoid any interaction of Se at the III-V/II-VI interface i.e., formation of Ga_2Se_3 at the interface. This is followed by the low temperature growth of ~50 Å ZnCdSe "interfacial layer" at 170 °C. Growth was interrupted and the substrate temperature was adjusted to the desired growth temperature. A (2 x 1) surface reconstruction develops. At 250°C an ~80 Å thick $Zn_{(1-x)}Mg_xSe$ buffer layer was grown. Then a thick (~0.8 μm) $Zn_{(1-x)}Mg_xSe$ epilayers were grown at 270°C. A very slow growth rate of 0.40-0.50 μ/hour is maintained because it was found that too fast a growth led to a spotty RHEED pattern indicating a three dimensional (3D) growth. Several samples were grown with different composition. A streaky (2x1) RHEED pattern was observed throughout the growth of the II-VI material, indicating

the zincblende phase stability and the absence of facet formation. Since high Mg content materials are highly reactive and hygroscopic, the samples were capped with a ~50 Å thick ZnCdSe cap layer to avoid oxidation.

3.4. Results and Discussions

The $Zn_{(1-x)}Mg_xSe$ crystalline quality was assessed by double crystal x-ray diffraction (DCXRD) measurements using a double-crystal biaxial diffractometer and $CuK_{\alpha 1}$ radiation. In order to calculate the bulk lattice constant, the (004) symmetrical reflection and the (115) *a* and *b* asymmetrical reflections of the DCXRD rocking curves were obtained. The compositions of the films were determined using the bulk lattice constant and a linear interpolation between the lattice constants of ZnSe, 5.668Å,[13] and MgSe, 5.90Å, the last value is an average of the two reported values, [20] 5.89 and 5.904Å, respectively.

Samples were grown with Mg contents ranging from 65% up to lattice-matched conditions (~87% Mg) or slightly in excess of Mg (up to 92% Mg). All the samples were found to be of the zincblende structure. During the growth of the ZnMgSe epilayers, the RHEED showed a streaky (2x1) pattern throughout. A very slow growth rate of ~0.4 to ~0.5 μm/hr was maintained

during the growth as it was observed that too fast a growth in some cases led to a spotty RHEED pattern.

Figure 3.2 shows a single crystal x-ray spectrum of a 0.9 μm ZnMgSe bulk layer grown on InP. The Bragg peak arising from the (400), (200) and (111) reflections of both the InP substrate and the ZnMgSe epilayers are shown. The expected Bragg angle of the rocksalt phase MgSe and ZnMgSe were calculated by taking the 5.464 Å as the rocksalt lattice parameter. [27] Since the lattice constant of the rocksalt structure is different than the zincblende MgSe (5.90 Å), the peak of the rocksalt phase, if any, must have appeared as a unique separate peak from the other assigned peaks in the spectra. The observed peak positions of the ZnMgSe are consistent with a zincblende structure in all the reflections, suggesting a favored zincblende structure formation during growth. This and other wide-angle analysis of the single crystal X-ray have shown no additional peaks, confirming the absence of any rocksalt structure formation with the higher Mg contents.

Figure 3.3 presents the double crystal x-ray rocking curve of a 0.55 μm thick $Zn_{0.09}Mg_{0.91}Se$ layer with a 0.18% ($\Delta a/a \times 100$) lattice mismatch to the InP substrate. The inset in this figure shows the room temperature reflectance measurement indicating a bandgap of 3.58 eV. The PL measurement of this sample is not possible with our experimental setup because of the proximity of

this emission to the 325nm He-Cd laser line. The (511) *a* and *b* DCXRD spectrum of the same sample is shown in figure 3.4. From the (115) *a* and *b* asymmetrical reflections and using equation 2.8 and 2.9 of chapter two, the lattice constant of the epitaxial layer perpendicular ($a_{\perp}$) and parallel (a_{II}) to the growth surface was obtained to be 5.878 Å and 5.870 Å, and a lattice mismatch of 0.158% and 0.022%, respectively. [28] These measurements allow us to calculate the bulk (relaxed) lattice constant of the layers using the following equation with a poisson ratio of $\nu = 0.28$,

$$a_{bulk} = [(1-\nu) / (1+\nu)]\, a_{\perp} + [2\,\nu / (1+\nu)]\, a_{II} \qquad (3.1)$$

For the sample presented in figure 3.3, the bulk lattice constant was found to be 5.874 Å. From the comparison of the perpendicular and parallel lattice constants it was found that the samples were partially relaxed.

In most of these samples we have observed the very low intensity of the peak of the ZnMgSe epilayers in the x-ray measurement, which is consistent with other reports. [29] In order to understand this behavior we have estimated the expected relative intensity of the peaks based on the value of the structure factors for ZnSe, MgSe, ZnCdSe, and ZnMgSe, as described below. The structure factor F for binary compounds $A_{II}B_{VI}$ can be obtained from the atomic scattering factor *f*, which describes the efficiency of scattering, and is the ratio between the amplitude of the wave scattered by an atom to the

amplitude of the wave scattered by one electron. Thus, the atomic scattering factor depends on the atomic number of the constituent atoms. The structure factor F, depends on the unit cell of the crystal lattice. The relationship between the structure factor and the atomic scattering factor is-

$$| F |^2 = 16 (f_A + f_B)^2 \qquad (3.2)$$

The relative intensity of the peaks was calculated via the calculation of the structure factor using Debye-Scherrer equation for ZnSe, MgSe, ZnCdSe, and ZnMgSe. [30] In our case, we have done the following calculation using a simplified version of the Debye-Scherrer equation-

$$I = | F |^2 \, p \, \{(1+ \cos^2 2\theta_B) / (\sin^2 \theta_B \cos\theta_B)\} \qquad (3.3)$$

where, I is the relative integrated intensity (arbitrary units), F = structure factor, p = multiplicity factor, and θ_B = Bragg angle. The trigonometric terms in parentheses are the Lorentz-polarization factors. The term $(1+ \cos^2 2\theta_B)$ is called the polarization factor in this case. The overall use of this geometrical factor is to decrease the intensity of reflections at intermediate angles compared to those in the forward or backward direction. $\mathrm{Sin}^2\,\theta$ can be obtained from the Bragg equation, $2d \sin \theta_B = n\lambda$.

The results are summarized in table 3.1. The calculated relative intensity of ZnMgSe was found to be very small. This is related to the inefficient scattering of the magnesium atom. As was described earlier, the

atomic scattering factor increases with increasing atomic number and ultimately increasing number of electrons in the orbital. The atomic number of Mg is 12 while that of Zn is 30.

Typically, the tetrahedral covalent radius increases within the column as the row number increases in the periodic table. This means the degree of shrinkage of average radius of the outermost orbital caused by the increase of the nuclear charge is less than the degree of enlargement of the average radius of the outermost orbital caused by the addition of the new orbital due to the increase of the principal quantum number in the same column. Mg (group IIA), is larger than Zn (group IIB). This means that shrinkage of the average radius of the outermost orbital caused by the increase of the nuclear charge (12 for Mg to 30 for Zn) is more pronounced than the enlargement of the average radius of the outermost orbital (3s, 3p for Mg to 4s, 4p for Zn) with the increase of the principal quantum number. [31] Thus, the larger MgSe results in lower x-ray intensity than ZnSe.

Figure 3.5 shows the double crystal x-ray of a $Zn_{0.148}Mg_{0.852}Se$ sample closely lattice matched ($\Delta a/a \sim -0.05\%$) to the InP substrate, whose thickness measured by the cylindrical groove technique is ~0.75μm. The low intensity oscillations between the satellite peaks are Pendellösung oscillations. These originate from the interference between two x-ray wave fields within the

crystal. [32] Generally, two interfering wave fields are generated at the entrance surface of the crystal and cause intensity oscillation at the exit surface producing equal thickness fringes on an x-ray topograph. These fringes are weaker than the main Bragg peak and highly sensitive to the thickness uniformity and flatness of the film. They are usually not present in the thicker samples (>1μm) because in those cases the lack of the lower surface causes one of these x-ray wave fields to be absent, thus leading to a loss of phase coherence. [33] These thickness fringes are an indication of high crystalline quality of the samples. [34-35] Any imperfection, relaxation, or compositional inhomogeneity would cause loss of phase coherence and eliminate the fringes. The thickness of the epilayer can be calculated from the period of the fringes using the following relations-

$$t = \lambda \gamma_H / \Delta\theta \mathrm{Sin}2\theta_B \qquad (3.4)$$

The simplification of this formula yields to-

$$t = \lambda / 2\Delta\theta \mathrm{Cos}\theta_B \qquad (3.5)$$

Where λ is the X-ray wavelength, γ_H is the direction cosine of the reflected beam with respect to the layer normal, θ_B is the Bragg angle and $\Delta\theta$ (arc seconds) is the angular spacing of adjacent maxima or minima measured in the wings of the rocking curve. [36] In our sample of ZnCdSe/ZnMgSe/InP shown in Figure 3.5, one of the fields is generated at the interface between

ZnCdSe and ZnMgSe and another wave field is on the surface of the ZnCdSe layer. As was stated, interference can only be seen in crystals that are thin and have perfectly parallel boundaries. [37] The thickness of the layer illustrated in Figure 3.4, calculated from the Pendellösung fringes, is 0.38 μm, which confirms a significant error in the cylindrical groove technique that we used previously to measure the thickness of the sample. A very weak shoulder seen on the higher angle side of the curve in Figure 3.5 is the InGaAs buffer layer.

Photoluminescence (PL) measurements were performed at 77K using the 325 nm line of the He-Cd laser for excitation. Reflectance measurements were performed using a Cary500 spectrophotometer. Figure 3.6 shows the PL at 77K and the room temperature (RT) reflectance spectra of a sample with 85% of Mg (near lattice matched to InP). A very efficient PL emission at 3.59 eV was observed with a full width at half maximum (FWHM) of ~103 meV. We observed that the width of the PL peak increased with increasing Mg content in the alloy, a behavior that has been observed in other Mg alloys. Also, no deep level emission, characteristic of poor material quality, was observed in any of the samples. The RT bandgap of the sample from the reflectance measurement was found to be 3.52 eV and differs by 0.07 eV from the PL peak value. This difference corresponds approximately to the

anticipated temperature dependence of the bandgap. The PL and reflectance spectra were overlapped in the figure to illustrate the direct band gap of this material.

Figure 3.7 shows the bandgap energy as a function of Mg concentration and lattice mismatch to the InP substrate (top axis) of the $Zn_{(1-x)}Mg_xSe$ alloys. The open square data points are taken from our PL measurements at 77K, the open triangles are from our reflectance measurements at RT, and the open squares are the estimated 77K PL values for the same samples. We have done this estimation because the PL emission of these samples was close to the laser line, and thus could not be directly measured at 77K. To estimate the 77K value of the bandgap we added 0.07eV to the band gap value obtained by reflectivity measurements at RT, which is the average observed difference between the PL and reflectivity measurements in the samples for which both measurements were possible. The solid circles, solid squares and solid up- and side-triangles are the band gap values of $Zn_{(1-x)}Mg_xSe$ alloys grown on GaAs reported in references 16, 17, 29 and 31, respectively. The solid down-triangle represents the band gap of MgSe grown on InAs, reported by Litz. [20] A linear relationship between Mg concentration and bandgap was observed for our measurements and for most of the reported values, and is in excellent agreement with Vegards law which states that the lattice constant in the alloy

will depend linearly on the composition. In this case assuming the relationship between the lattice constant and the composition for $Zn_{(1-x)}Mg_xSe$, the lattice constant of the ternary alloy will be the linear combination of the lattice constant of the binary compound ZnSe and MgSe which is:

$$a_{Zn(1-x)MgxSe} = xa_{ZnSe} + a_{MgSe}(1-x) \qquad (3.6)$$

Here the lattice constant of the ZnSe and MgSe are 5.668 and 5.90 Å. Based on the alloy composition (x) we can calculate the lattice constant of the ternary alloy $Zn_{(1-x)}Mg_xSe$.

Lattice matched $Zn_{(1-x)}Mg_xSe$ was grown on InP substrates with a band gap of ~3.59 eV with 87% Mg. Furthermore, with higher Mg content the bandgap of the ZnMgSe grown on InP substrates was increased to ~3.66 eV. The relationship between bandgap (E) and composition (x) at 77K is given by the following empirical formula:

$E(x) = 2.764 + 0.975x$; where x ($0 \leq x \leq 1$) is the Mg concentration

Figure 3.6 shows agreement between the band gap values in the literature and the linear relationship for concentrations of Mg up to 80%. For high Mg concentrations reference 21 reported that when $Zn_{(1-x)}Mg_xSe$ is grown on GaAs it undergoes a phase transition from zincblende to rock salt. References 17 and 20 reported a very large increase in the band gap for samples with 95% and 100% Mg grown on GaAs and on InAs, respectively. However, our

measurements clearly indicate that when high crystalline quality, zincblende layers are grown the linear relationship holds for values up to 92% Mg. We conclude that the observation of these very large bandgap values by others is due to the fact that both samples were grown with a very large lattice mismatch to the substrate which produced a very large strain, which as pointed out in reference 21, make it likely that they contain a rocksalt phase. The existence of a bowing parameter of the band gap of $Zn_{(1-x)}Mg_xSe$ as function of the Mg composition, reported in reference 17, is based on the band gaps of these two anomalous samples. Our results for a large number of samples with compositions between 65 and 95% Mg show that this bowing is not present. Using an extrapolation based on the linear fit shown in figure 3.5, it follows that the bandgap of zincblende MgSe is 3.74eV, which is in close agreement with the calculated values of 3.67eV and the 3.6 eV reported in references 16 and 31. The near linear dependence of the band gap and the Mg concentration presented in this work is in agreement with the first principle calculations of the bowing parameter of reference 31 based on Van Vechten's method which states that the bowing parameter is a function of the difference between the heteropolar bandgap energy of the constituent binaries (ZnSe and MgSe) that comprise the ternary, [38] and those based on Hill's theory, [39] both of which indicate that this value is zero. Also, Okuyama et al. has calculated

the bowing of ZnMgSe in detail with modified dielectric theory by considering intrinsic bowing along with extrinsic bowing (Vechten's method) and found that the bowing is about 0.1 eV, which is very close to the reported value of zero. An intrinsic bowing parameter arises due to the aperiodicity in the crystal. [31]

We have added the experimental data of ZnMgSe (blue square boxes) obtained in this study to the remaining $Zn_xCd_yMg_{1-x-y}Se$ experimental results from our previous work in the format of bandgap vs. lattice mismatch to InP, and they are shown in figure 3.7. In this figure we have used 3.74 eV value as the bandgap of MgSe that was obtained from our extrapolated values.

In summary, a series of zincblende structure $Zn_{(1-x)}Mg_xSe$ layers were grown by MBE on InP substrates with excellent crystalline quality. Their band gaps were determined by PL and reflectance measurements. The band gap was adjusted up to ~3.66 eV with increasing Mg content. A linear dependency was observed between the band gap and the Mg concentration of the ZnMgSe alloys, predicting a value of the bandgap for zincblende MgSe of 3.74 eV. Wide-angle single crystal x-ray measurements have confirmed the absence of the rocksalt phase formation in the ZnMgSe alloys grown on InP.

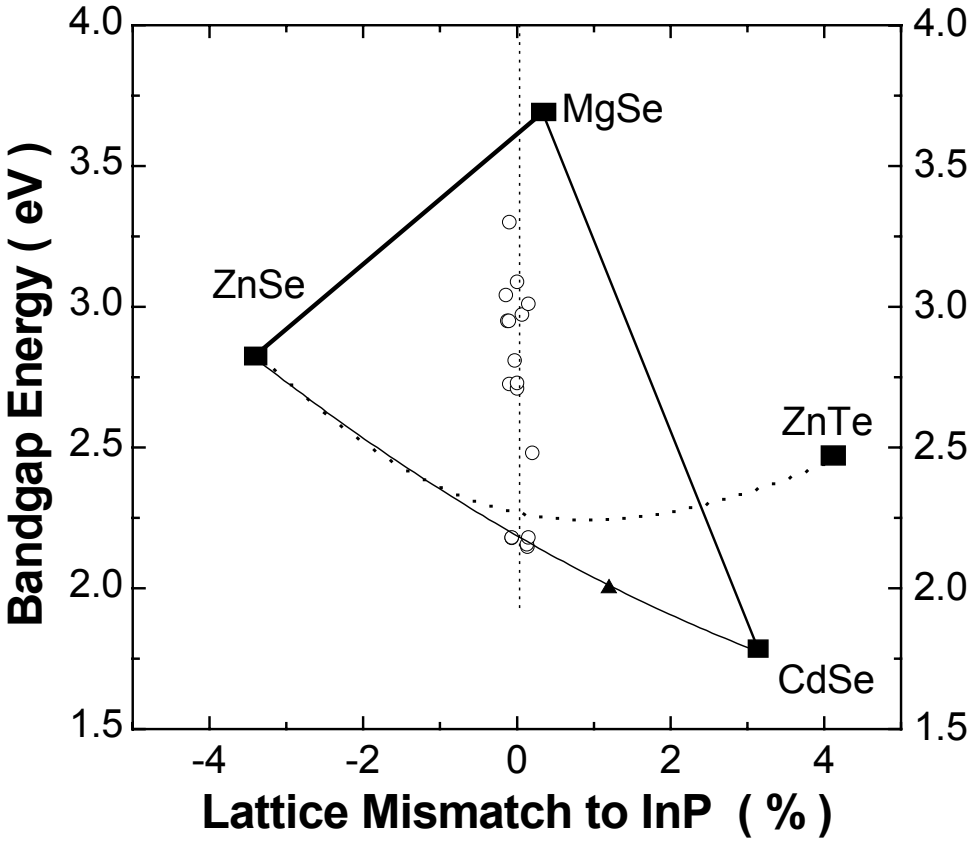

Fig. 3.1. Band gap energy versus lattice mismatch to InP substrate for $Zn_xCd_yMg_{1-x-y}Se$ material family.

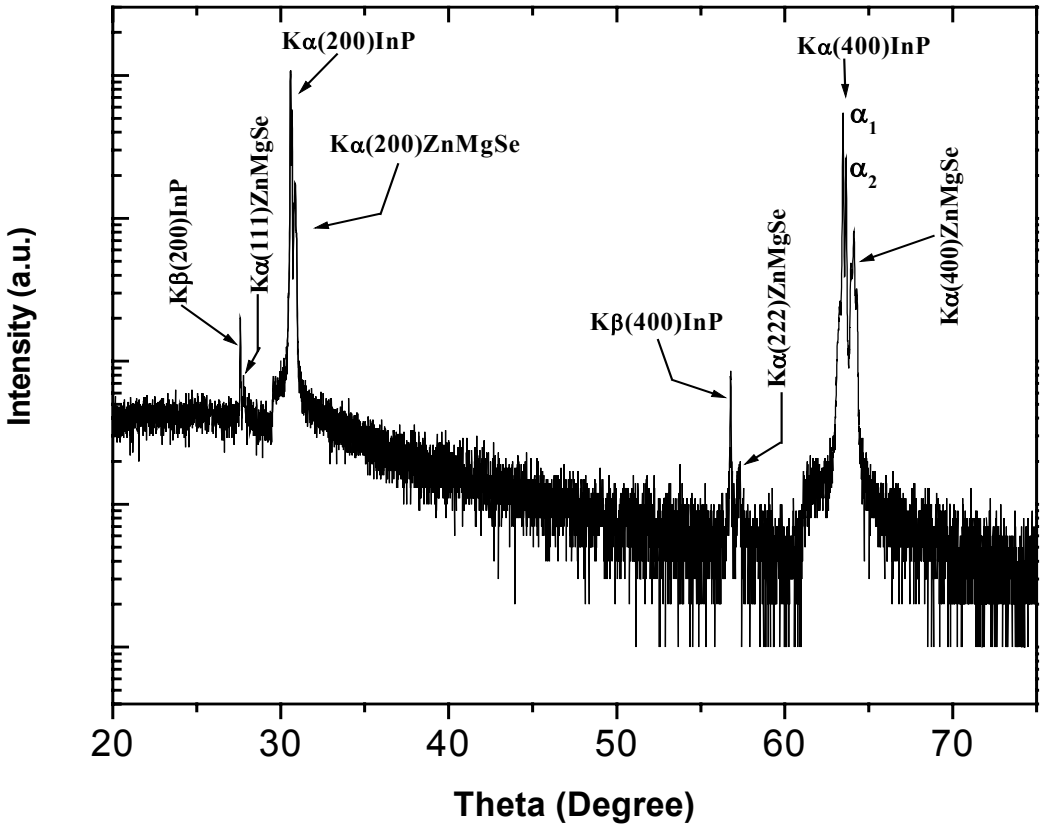

Figure 3.2 Single crystal XRD spectrum of a 0.90 μm thick $Zn_{0.17}Mg_{0.87}Se$ grown on InP (001). The (111), (222), and (200) diffraction peaks of ZnMgSe and InP are shown.

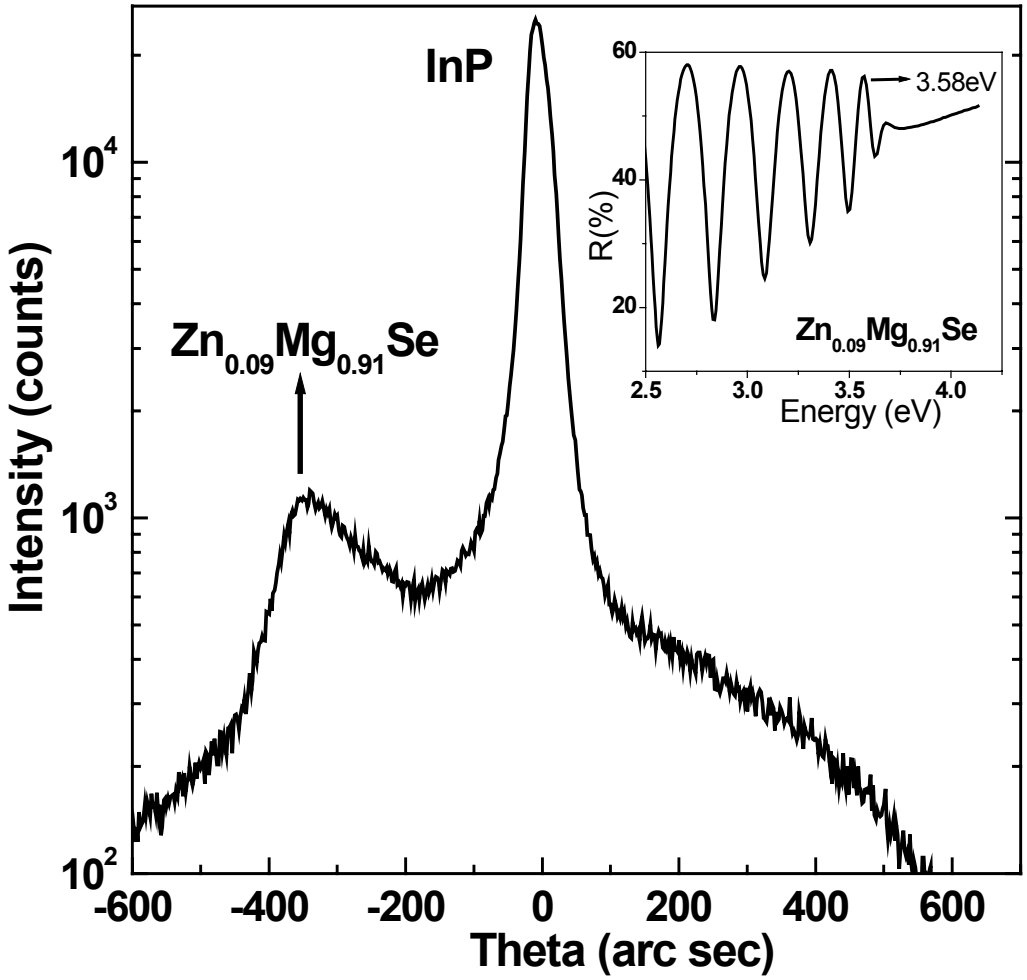

Figure 3.3. (004) reflection double crystal x-ray rocking curve spectrum of a 0.55μm thick $Zn_{0.09}Mg_{0.91}Se$. Room temperature reflectance measurement of the same sample. (inset)

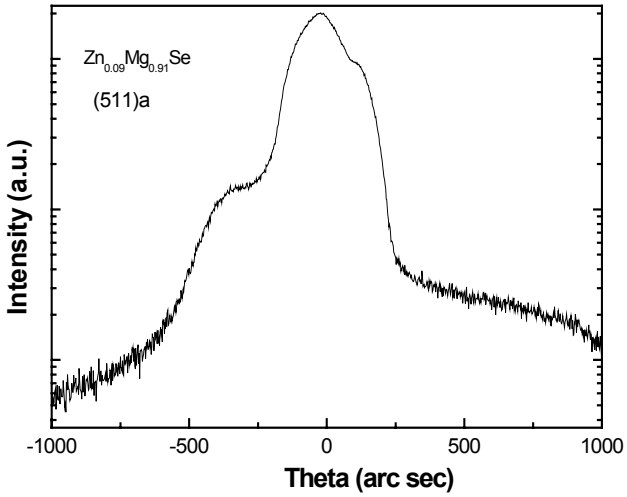

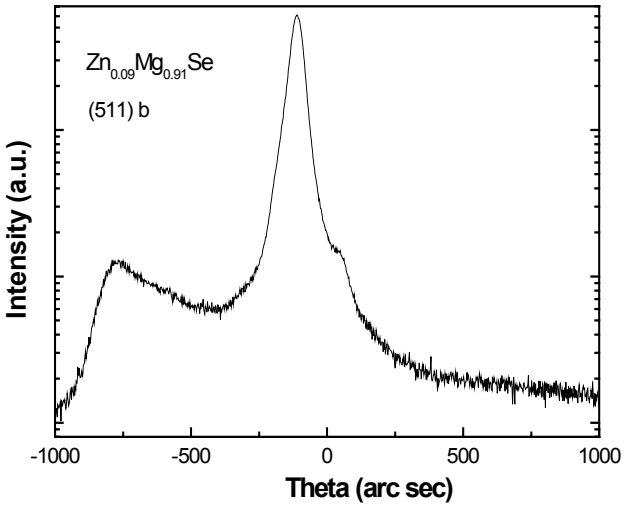

Figure 3.4. (115) *a* and *b* reflection double crystal x-ray rocking curve spectrum of a 0.55μm thick $Zn_{0.09}Mg_{0.91}Se$.

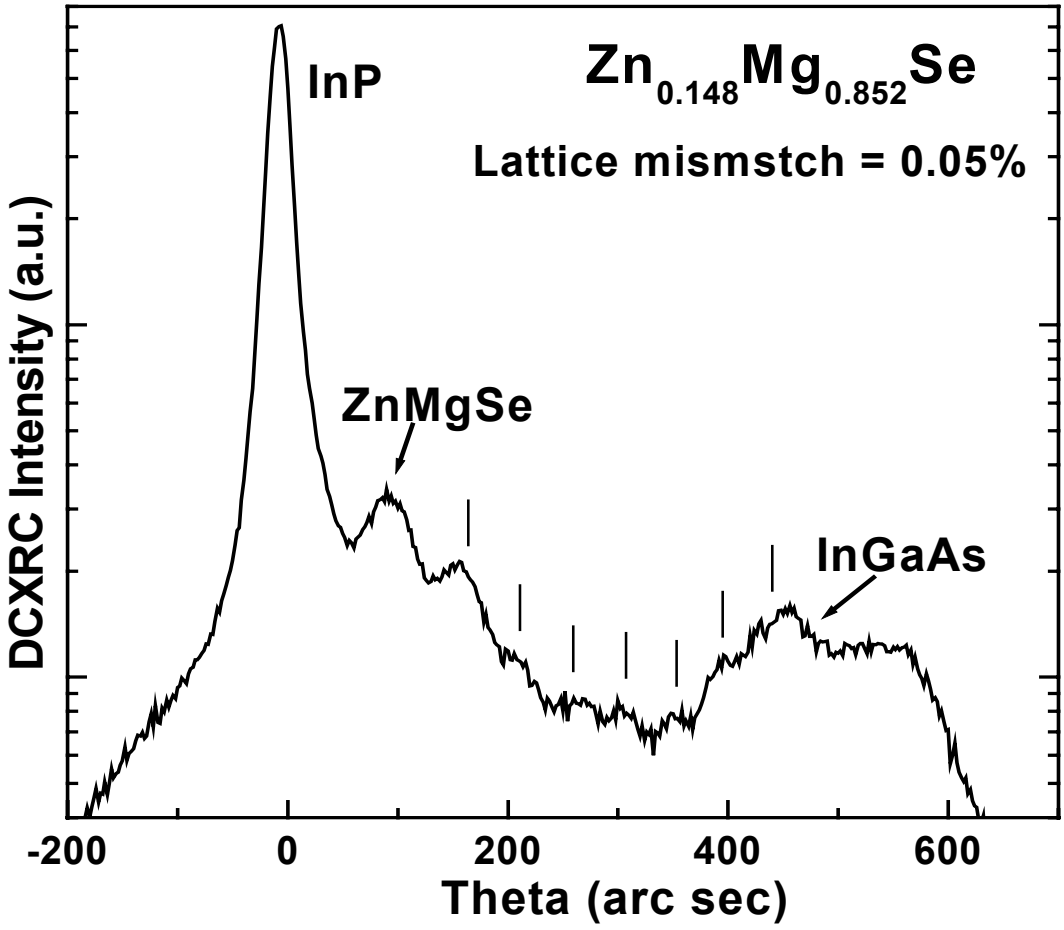

Figure 3.5. The double crystal x-ray rocking curve of a 0.75μm $Mg_{0.852}Se$ sample closely lattice matched to ($\Delta a/a \sim -0.05\%$) InP substrate.

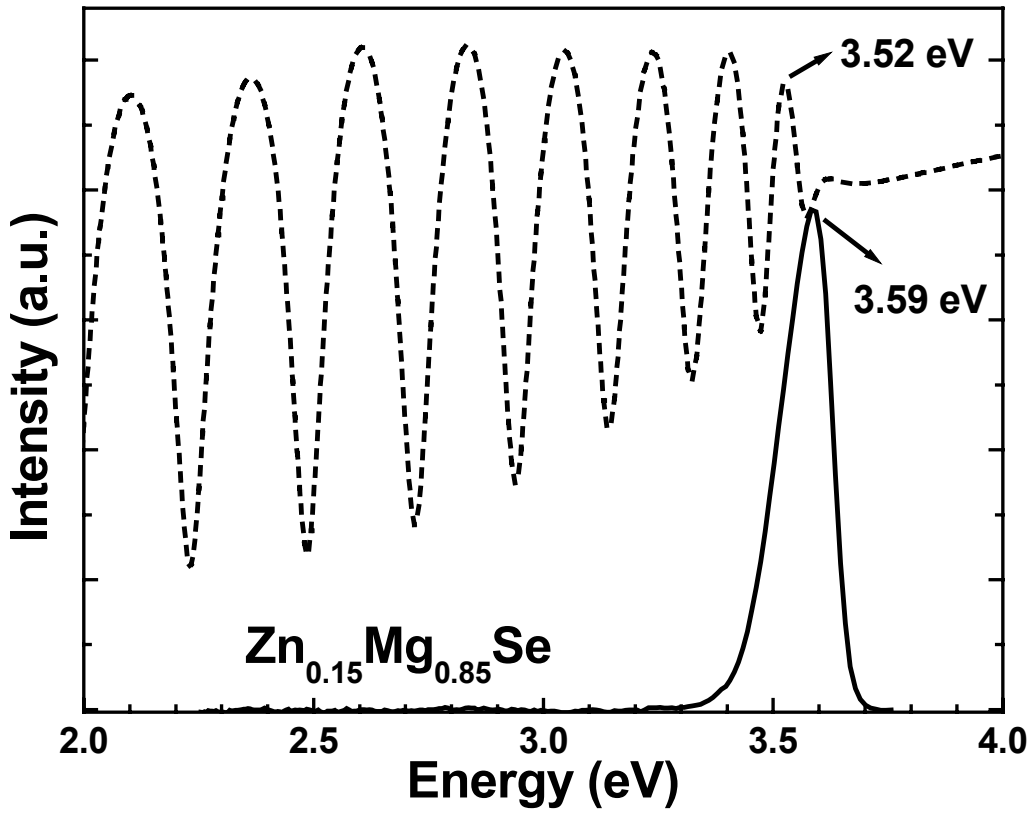

Figure 3.6. 77K PL and room temperature reflectance spectra of a $Zn_{0.15}Mg_{0.85}Se$ epilayers.

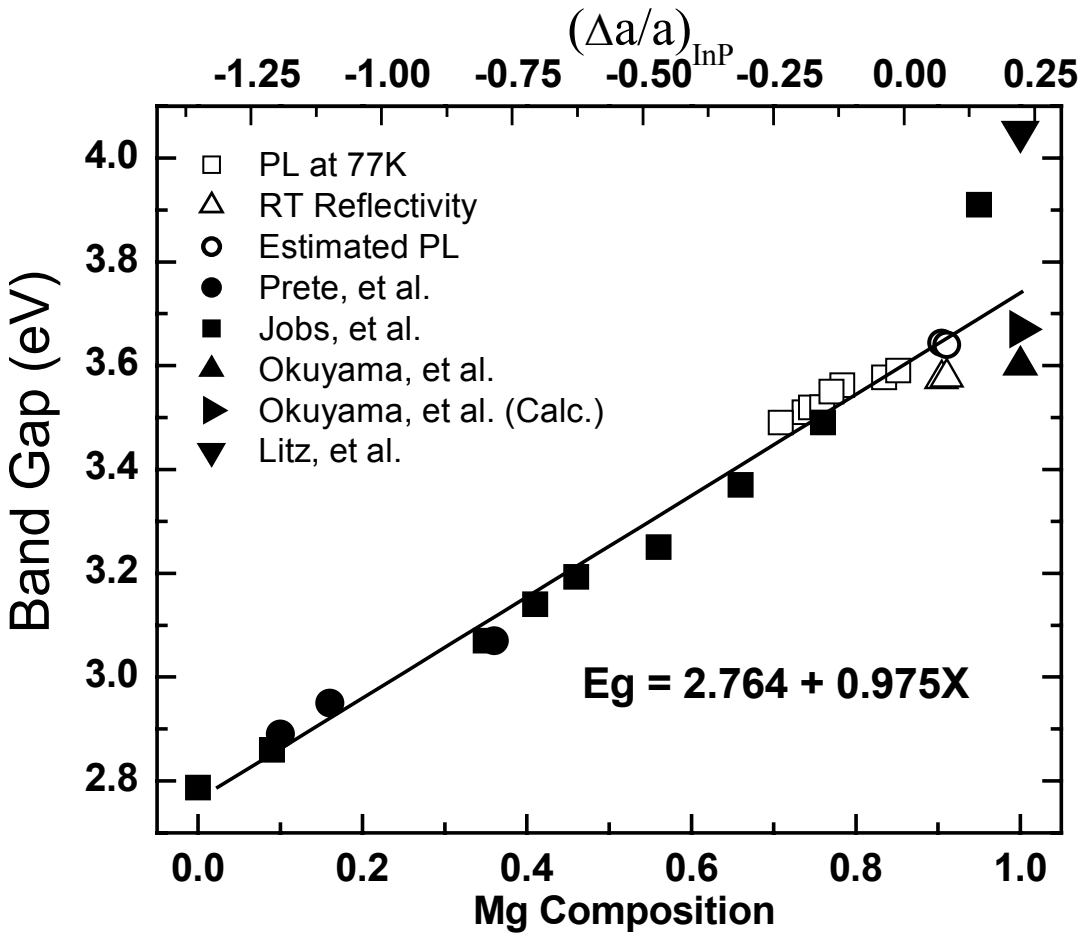

Figure 3.7. Bandgap energies of $Zn_{1-x}Mg_xSe$ alloys as a function of the Mg concentration and the lattice mismatch to InP. The sources of these data are our PL experiments at 77K (□), our reflectance measurements at RT (△), estimated band gap at 77K using our RT measurements (○), and references 29, 17, 16, 20, and 31 (●, ■, ▲, ▼ and ▶), respectively.

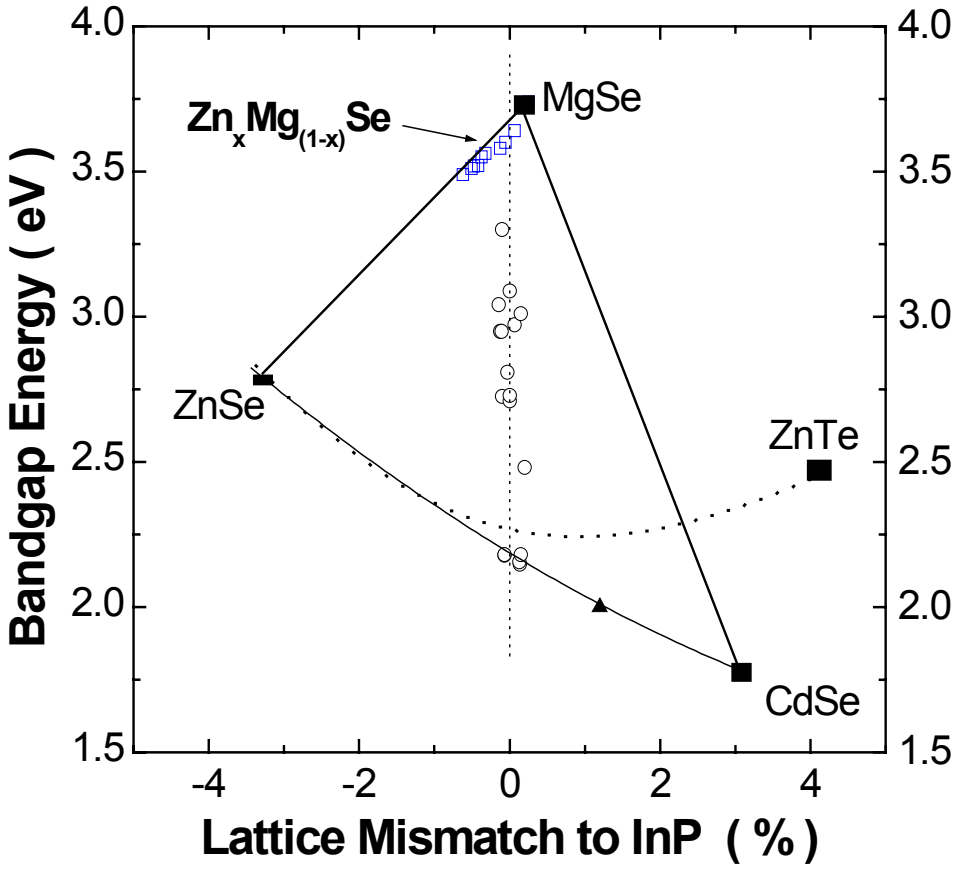

Fig. 3.8. Band gap energy versus lattice constant for $Zn_xCd_yMg_{1-x-y}Se$ material family. $Zn_xMg_{1-x}Se$ composition are shown in blue squares.

Table 3.1. I/I_{max} of different material system.

Structures	$\|F\|^2$	p	$\frac{(1+\cos^2 2\theta)}{(\sin^2\theta \cos\theta)}$	I	I/I_{max}
ZnSe	25728	6	5.13	791907.8	0.62
MgSe	10691	6	5.13	329068.9	0.26
CdSe	41290	6	5.13	1270906	1
ZnCdSe	33509	6	5.13	1031407.02	0.81
ZnMgSe	12193	6	5.13	275300	0.21
ZnCdMgSe	16474	6	5.13	507082	0.398

Chapter 4

Optical properties of $Zn_{(1-x')}Cd_{x'}Se/Zn_{(1-x)}Mg_xSe$ Quantum Wells

One of our primary goals for this research is to investigate the potential of the ternary $Zn_{(1-x)}Mg_xSe$ for quantum cascade lasers. So it is of our great interest to understand the growth and characterization of $Zn_{(1-x')}Cd_{x'}Se/Zn_{(1-x)}Mg_xSe$ quantum wells (QW), their electron and wave confinement in the laser structure. Wide band gap II-VI $Zn_{(1-x)}Mg_xSe$ material has potential application as a cladding layer for optical devices in the blue region due to its wide direct band gap. [1] In the previous chapter the growth of high crystalline quality zincblende $Zn_{(1-x)}Mg_xSe$ grown on InP (001) substrates by molecular beam epitaxy (MBE) has been described. [2] It was shown that a nearly lattice matched $Zn_{0.15}Mg_{0.85}Se$ layer can be grown on InP with a bandgap of 3.59 eV at 77K.

In this chapter we present the investigations of the optical properties of a series of $Zn_{(1-x')}Cd_{x'}Se/Zn_{(1-x)}Mg_xSe$ single QW samples lattice matched to InP (001).

4.1. Emission of $Zn_{(1-x')}Cd_{x'}Se/Zn_{(1-x)}Mg_xSe$ quantum wells

The heterostructures were fabricated in the MBE chamber. The $Zn_{0.13}Mg_{0.87}Se$ / $Zn_{0.53}Cd_{0.47}Se$ QWs were grown lattice matched to InP substrates. The schematic of the structure is shown in figure 4.1 along with a band diagram. The InP substrate was deoxidized at ~ 490°C under an As-flux impinging on the substrate. Then a ~0.1 μm InGaAs buffer layer was grown to smooth the surface and to adjust the surface stoichiometry. The sample was then transferred into the II-VI chamber. Prior to II-VI growth, the buffer was exposed to a Zn flux for 40 sec. This was followed by growth of a 50Å ZnCdSe interfacial layer at 170°C. The temperature was then raised to 270°C and the desired QW structures were grown. The beam equivalent pressure (BEP) ratio of the group-VI to group-II fluxes was ~5-6. For the structures, ZnCdSe QW layer was sandwiched between two $Zn_{0.13}Mg_{0.87}Se$ barrier layers with thickness of 0.3 μm and 0.15 μm for the bottom and top barrier layer, respectively. The same Zn flux was used for both barrier and well but Mg and Cd fluxes were adjusted to have lattice-matched conditions. The thickness of the well was varied between 6Å and 70Å. The growth was monitored *in-situ* by reflection high-energy electron diffraction (RHEED). A streaky (2x1) RHEED pattern was observed during the growth indicating layer-by-layer growth, and Se-rich conditions. Since

ZnMgSe is very hygroscopic, a 70Å thick cap layer of ZnCdSe or CdSe was used to avoid oxidation of the ZnMgSe layer. Thick calibration samples of ZnMgSe barrier layers and ZnCdSe layers were grown as well.

All the samples have the same structure as shown in figure 4.1 except for having different ZnCdSe well thickness. The band gap of the lattice matched ZnMgSe barrier layer was 3.59 eV and the band gap of the lattice matched ZnCdSe well used is 2.1 eV. The room temperature and low temperature (77K) PL spectrum of a 6Å thick QW structure is shown in figure 4.2. A very strong PL emission was observed in the near-UV region at 3.31 eV at 77K and at 3.190 eV at room temperature. No deep level emission was observed. The full width at half maximum (FWHM) of the PL emission lines were measured to be 114 meV at 77K and 115 meV at room temperature. The FWHM of the PL emission is almost the same at room temperature and at 77K (and even at 9K), which is attributed to dominant interface broadening effects due to the very narrow well. The strong RT emission suggests the very high quality of the sample. Also, the low intensity peak in the lower energy level of the spectrum shown by an arrow around 2.17 eV at 77K and RT is the ZnCdSe cap layer's emission.

A set of samples having QW thicknesses ranging from 6 Å to 60 Å was grown and their PL spectra were measured. The PL emission peak

energy as a function of QW layer thickness is plotted in Figure 4.2. The dashed line is the fit obtained by considering a finite barrier model, the details of which will be described below. In this model, the upper and lower boundary is dictated by the band gap of the lattice matched $Zn_{0.15}Mg_{0.85}Se$ (3.59 eV) and ZnCdSe materials (2.1 eV), with a conduction band offset of 80% of the band gap discontinuity. This offset estimate is based on contactless electroreflectance measurements (CER) results that are presented in the next chapter. [3-4] An excellent fit between the experimental results and calculated values was observed indicating a good QW behavior. Also, the confinement energy decays as the thickness of the well is increased. It also shows that there is a large tunability range of the QW emission covering from the near-UV to the visible range of the spectrum using ZnMgSe barrier layers grown near lattice-matched on InP substrates.

4.2. Finite Barrier Model:

In order to calculate the energy level within the quantum well, we have used the finite barrier model, which solves the Schrödinger equation in a finite potential square well by applying the appropriate boundary conditions, a first order quantum mechanical calculation. [5-7] In order to use the finite barrier model to calculate the energies in the high bandgap materials, band non-parabolacity, a phenomenon that arises due to the

interband mixing, must be considered. [8] It also requires the modification of the boundary conditions to include the effective masses at the interface which will be described later of this section. First we consider a simple model of finite QW.

The time independent Schrödinger equation for a single particle of mass m moving in one dimension is-

$$\frac{\hbar^2}{2m}\frac{d^2\Psi(x)}{dx^2} + V_o(x)\,\Psi(x) = E\Psi(x) \qquad (4.1)$$

Figure 4.4 shows a potential well centered at the origin of width w and barrier height V_0, the structural potential seen by the particle (electron or hole). In the equation, *E* is the energy of a given state, for the finite square potential well.

The potential energy function is $V = V_0$ outside of the well. The wave function, $\Psi(x)$ must fulfill the following boundary conditions-

1. $\Psi(x)$ must be continuous every where
2. $d\Psi(x)/dx$ must be continuous every where
3. lim $|\Psi(x)|$ is finite, as x → infinity

Inside the well, the potential is zero. So $\Psi(x)$ is the sum of two plane waves of opposite wave vectors in $|x| < w/2$ and $x|> w/2$, and inside the well these wave propagate. So,

$$\frac{\hbar^2}{2m}\frac{d^2\Psi(x)}{dx^2} + k_1\,\Psi(x) = 0, \quad \text{where } |x| < w/2 \text{ with } k_1 = (2mE/\hbar^2)^{1/2} \text{ and} \qquad (4.2)$$

$$\frac{\hbar^2}{2m}\frac{d^2\Psi(x)}{dx^2} - k_2\,\Psi(x) = 0, \quad \text{where } |x| > w/2 \text{ with } k_2 = [2m(V_0 - E/\hbar^2)]^{1/2} \qquad (4.3)$$

V(x) is even in the x direction. Thus the wave function $\Psi(x)$ can be chosen either even or odd in x. For the even wave functions, the solution of the Schrödinger equation within the well is-

$$\Psi(x) = \begin{cases} C_1 \exp(-k_2(|x| - w)) & \text{where } |x| > w/2 \\ C_2 \cos k_1 x & \text{where } |x| < w/2 \end{cases} \qquad (4.4)$$

The wave function and its derivative must be continuous at the boundaries of the well.

So, $C_1 = C_2 \cos k_1 w/2$ 4.5(a)

$$\frac{k_2 C_1}{m_b} = \frac{k_1}{m_w} C_2 \sin k_1 w/2 \qquad 4.5(b)$$

where, m_b and m_w are the masses of the particle in the barrier and in the well, respectively.

Eliminating C_1 and C_2 by dividing *5(b) by 5(a)* we obtain the quantization condition:

$$k_2 = \frac{m_b k_1}{m_w} \tan k_1 w/2 \qquad (4.6)$$

Similarly for the odd wave function-

$$\Psi(x) = \begin{cases} C_1 \exp[-k_2(x-w/2) & \text{where } x > w/2 \\ C_2 \sin k_1 x & \text{where } |x| \leq w/2 \\ -C_1 \exp[-k_2(x+w/2) & \text{where } x < -w/2 \end{cases} \qquad (4.7)$$

By applying the boundary conditions we find that –

$$C_1 = C_2 \sin k_1 w/2$$

$$\frac{-k_2 C_1}{m_b} = \frac{k_1}{m_w} C_2 \sin k_1 w/2 \qquad (4.8)$$

Thus, the eigenequation becomes -

$$k_2 = -\frac{k_1 m_b}{m_w} C_2 \cot k_1 w/2 \qquad (4.9)$$

The solutions for the quantised eigenenergies can be obtained by $k_1 w$ and $k_2 w$ using a graphical approach since -

$(k_1 w/2)^2 + m_w/m_b [(k_2 w/2)^2] = 2 m_w V_0 (w/2)^2/\hbar^2$ and

$k_2 (m_b/m_w)^{1/2} w/2 = (m_b k_1 w)/2m_w \tan k_1 w/2$ *for even solutions*

$k_2 (m_b/m_w)^{1/2} w/2 = -(m_b k_1 w)/2m_w \cot k_2 w/2$ *for odd solutions*

To find the allowed energy levels, we plot $k_2 (m_b/m_w)^{1/2} w/2$ against $k_1 w/2$ and find the points where the curve crosses the horizontal axis, which gives the energy levels. Using this approach the energy levels can be obtained within the QWs, which can be compared to the experimental values as shown in figure 4.3.

For high bandgap materials, band non-parabolacity plays an important role in which consideration of band mixing requires the modification of the second boundary conditions to include the effective masses at the interface. The band non-parabolacity amounts to replace the band edge mass by an energy dependent mass whose relative increment is equal to the ratio between the kinetic energy and the bandgap. Also, electron levels can be some tenths of an electron volt above the bulk conduction band edge and makes it deviate from the parabolic behavior. The non-parabolicity phenomenon is very important for excited levels than for the ground states.

Non-parabolicity in the proximity of energy band extrema in bulk semiconductors can be described by the dispersion relation-

$$E = \frac{\hbar^2 k^2 (1-\alpha k^2)}{2m^*} \qquad (4.10)$$

Where *E, k,* and *m** are the energy, wave number and effective mass of the charge carrier and α is the non-parbolicity parameter. [9]

For example, when a square QW is formed by $Al_xGa_{(1-x)}As/GaAs/ Al_xGa_{(1-x)}As$ with x = 0.37, with a GaAs layer thickness of 5 Å, the first electron subband edge calculated for a parabolic band has an energy of 256 meV and a wave number in the well of 6.8×10^{-8} m^{-1}. So it can be seen from Eq. (1) the non-parabolicity term would be expected to cause a lowering of the edge by a fractional amount of order $\alpha k^2 \sim 0.23$ using $\alpha = 4.9 \times 10^{-19} m^2$. This illustrates the importance of including the non-parabolicity in analyzing QWs.

Considering the effective masses, the modified new boundary conditions which are-

$$\Psi(x) \text{ and } \frac{1}{2m^*}\frac{d\Psi(x)}{dx}$$

must be continuous at the interfaces of the barrier and the QW material.

As mentioned above, in the case of finite potential, inside the well, the potential is zero and the potential energy function is $V = V_0$ outside of the well.

The solution for $\Psi(x)$ is:

$\Psi(x) = C_2 \sin k_1 x$, where $|x| \leq w/2$, $k_1 x w = n\pi$ and n = 1, 2,..

As described in detail in Ref. 8, the solution of the Schrödinger equation leads to the following equation from which we can obtain the values for different subband minima -

$$E_c = 1/2\alpha[(1+ (4\alpha\, \hbar^2/2m^*)\, (n\pi/w)^2]^{1/2} - 1] \qquad (4.11)$$

In conclusion, we have grown a series of nearly lattice matched ZnCdSe/ZnMgSe QW structures on InP substrates. By varying the QW thickness, low temperature PL emission in the range from 2.19 eV to 3.31 eV was obtained from these QW structures. Intense PL band edge emission with the absence of deep levels was obtained both at room temperature and 77K indicating good optical quality. The energy of the quantum well emission was described by the finite barrier model, confirming the well-behaved nature of these structures.

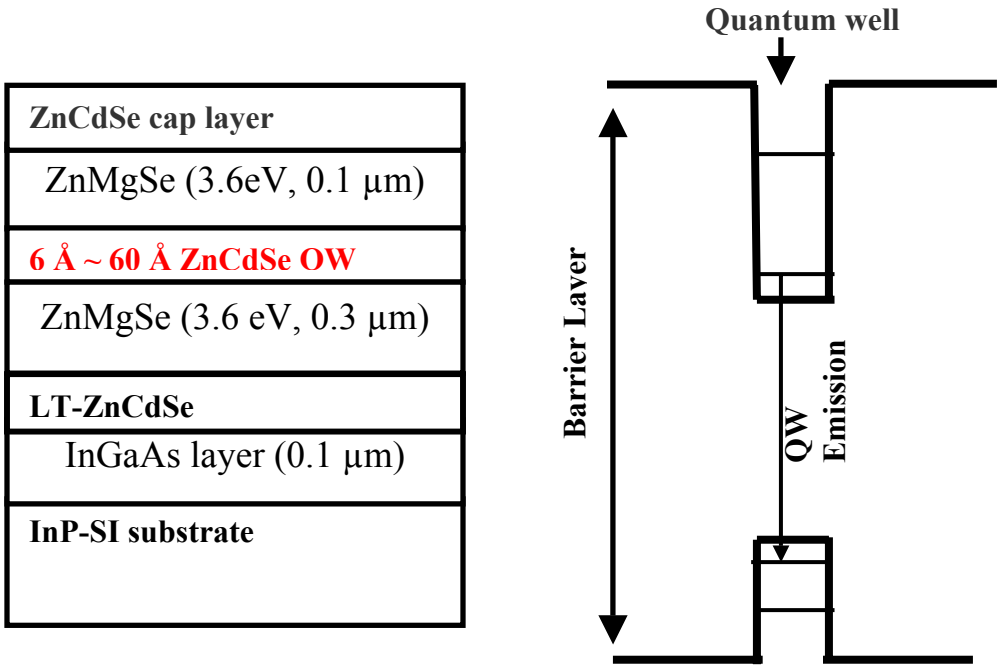

Figure 4.1. Schematic of the quantum well structure. Band diagram is shown on the right side.

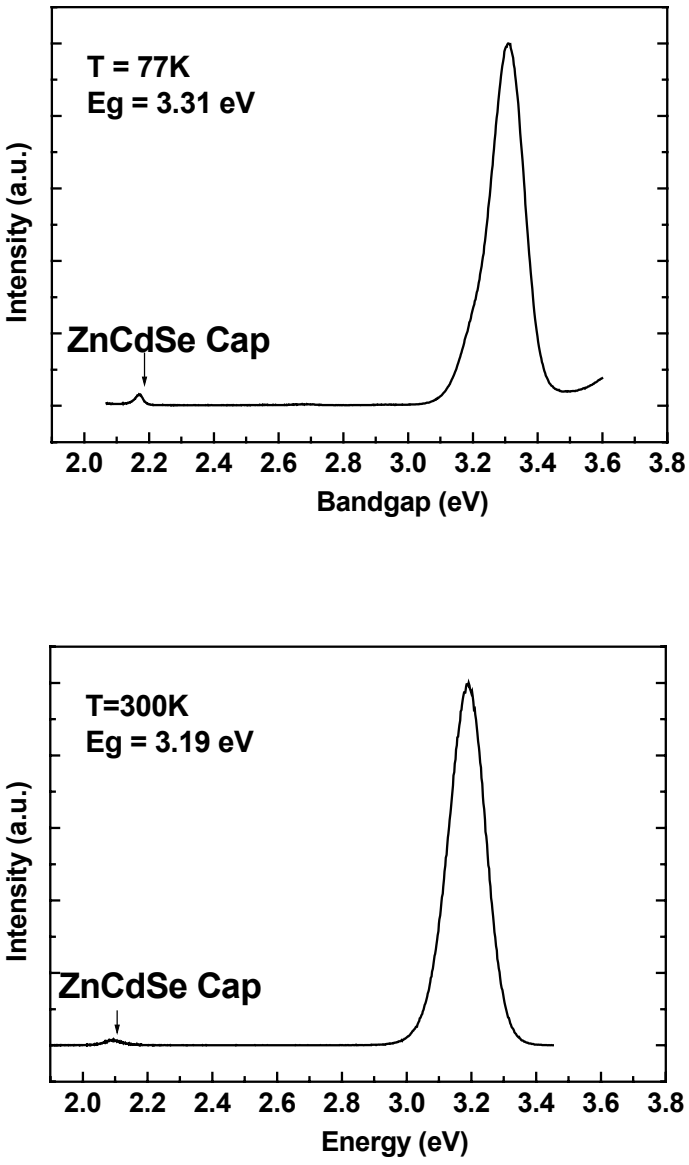

Figure 4.2 (a) 77K PL and (b) Room temperature spectra of a nearly lattice matched $Zn_{0.13}Mg_{0.87}Se/Zn_{0.53}Cd_{0.47}Se$ QW structure exhibiting near-UV visible emission.

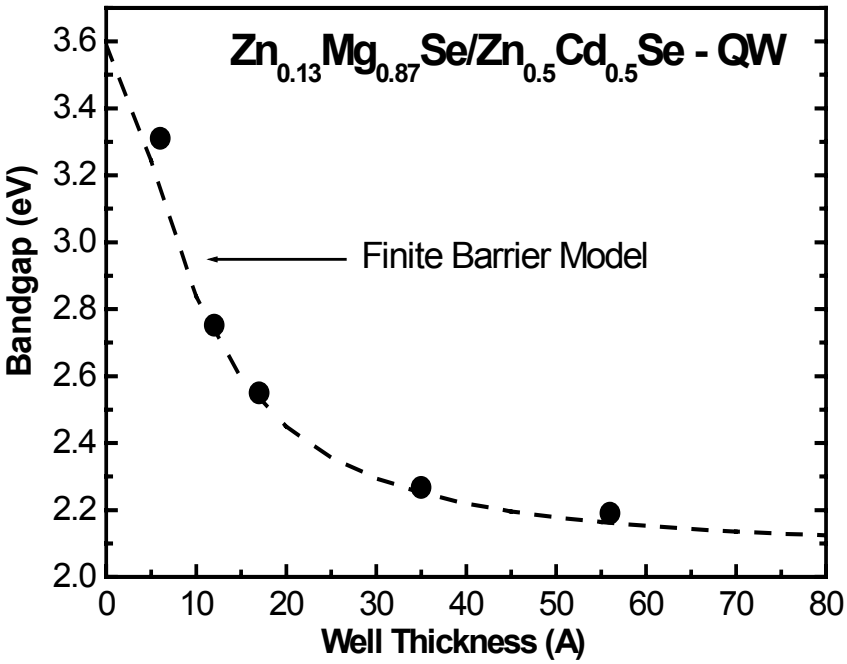

Figure 4.3.Bandgap as a function of QW thickness for a series of $Zn_{0.13}Mg_{0.87}Se/Zn_{0.53}Cd_{0.47}Se$ QW structures with a QW thickness varying from 6 to 60Å.

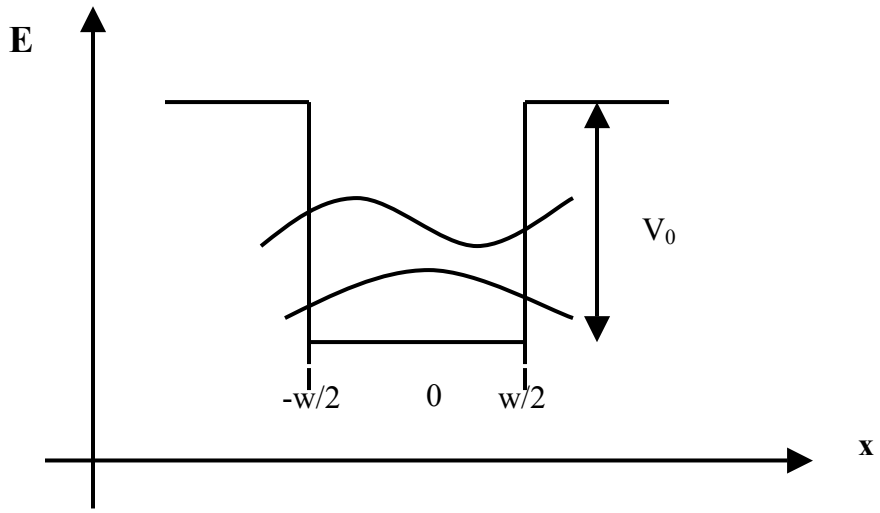

Figure 4.4 Potential energy for a particle (electron or hole) in a finite square potential well

Chapter 5

Band Offset Determination of $Zn_{X'}Cd_{(1-X')}Se/Zn_xCd_yMg_{(1-x-y)}Se$ Quantum Wells using Contactless Electroreflectance

As described in chapter 1, due to anticipated advantages such as simplicity of operation, unipolarity, wide wavelength tunability range in the mid infrared region, significant interest has been developed in quantum cascade lasers (QCLs) [1] and other intersubband devices. However, although considerable advances have been achieved in the development of the QCLs, some fundamental limitations inhibit the performance of the QCLs. In order to overcome some of these limitations, studies of the intersubband transitions have been recently extended to other systems based on GaN [2-3], GaSb [4-5] , Si [6] and II-VI compounds [7-10]. A large conduction band offset is desired for application in intersubband devices such as QCLs in order to address the present limitations of these devices. [11-17] As described in chapter 3, ZnMgSe lattice matched to InP substrates exhibits a bandgap as high as 3.6 eV. So, $Zn_{0.53}Cd_{0.47}Se/Zn_{0.85}Mg_{0.87}Se$ quantum well system is of primary

interest due to its large ΔE_g of ~1.5 eV. In this chapter, we will present the conduction band offset determination using the technique of contactless electroreflectance (CER) for $Zn_{0.53}Cd_{0.47}Se/Zn_{0.29}Cd_{0.24}Mg_{0.47}Se$ and $Zn_{0.53}Cd_{0.47}Se/Zn_{0.85}Mg_{0.87}Se$ quantum wells grown lattice matched to InP substrates.

5.1. Conduction band offset determination of a $Zn_{0.53}Cd_{0.47}Se/Zn_{0.29}Cd_{0.24}Mg_{0.47}Se$ single QW

The growth procedure $Zn_{0.53}Cd_{0.47}Se/Zn_{0.29}Cd_{0.24}Mg_{0.47}Se$ single QWs and their fundamental properties have been described in the previous chapters. In the samples used for this study, the $Zn_{0.53}Cd_{0.47}Se$ QW layer was sandwiched between a 0.1μm thick $Zn_{0.29}Cd_{0.24}Mg_{0.47}Se$ (E_0=2.8eV at room temperature) top barrier layer and 0.5μm thick ZnCdMgSe bottom barrier layer with the identical composition in the both barriers. A 70Å thick pseudomorphic ZnCdSe cap layer was used to protect ZnCdMgSe from oxidation. The beam equivalent pressure of the VI to II was ~3 for higher quality of the samples. The QW luminescence peaks were observed at 2.242 eV and 2.162 eV at 77 and 300K, respectively, while the luminescence peak for the barrier was at 2.880 eV at 77K.

The interband transitions in this structure were studied by CER measurement. As has been described in chapter 2, CER measures the changes in the optical reflectance of the material induced by a modulating electric field, giving rise to sharp, differential-like spectra in the region of the transitions. CER utilizes a condenser-like system consisting of a front wire grid electrode with a second metal electrode separated from the first electrode by insulating spacers, which are ~0.1 mm larger than the sample dimension. We placed the sample between these two capacitor plates and achieved electromodulation by applying an ac voltage of 1.2kV, 200 Hz across the electrodes. From the CER measurement we can observe higher order QW transitions, which allow us to obtain a good estimate of the anticipated large conduction band offset for this material system.

Figure 5.1 shows the room temperature CER measurement of a $Zn_{0.53}Cd_{0.47}Se/Zn_{0.29}Cd_{0.24}Mg_{0.47}Se$ single QW with a well thickness of ~50Å. The notation *EnH*(*L*)*m* in Fig. 5.1 indicates that the observed transitions are from the *n*th conduction subband to the *m*th valence subband of heavy (*H*) or light (*L*) hole character, respectively. In a quantum well, electrons and holes are confined and its wave function is localized in space. Since CER utilizes electric field, under an applied electric field along the confinement direction, the field adds a linear potential, which tilts the

confining potential, changing its shape. The electron and holes become spatially polarized, but still remain confined. This alters the electronic energies and the wave function overlap, which results in slightly different transitions energies with different intensity. The energies corresponding to the observed transitions were obtained using a fit of the experimental data, shown by the dashed line, based on the first derivative of a Gaussian line shape. [18] We use this line shape fitting because in the case of the modulated signal the features that we are interested in, are localized in photon energy. By analyzing these line shapes, we can estimate the accurate values of the energies and the broadening parameters of these transitions.

The following considerations were made in order to assign the observed transitions to physical processes as shown in figure 5.1 of the CER spectra. The assignment of the barrier peak at 2.8 eV was made from comparison to the 77K PL measurement which is 2.88 eV for the $Zn_{0.29}Cd_{0.24}Mg_{0.47}Se$ after considering its thermal shift of ~ 0.08 eV at room temperature. The transition at 2.159 eV is assigned to the $E_1 - H_1$ or lowest energy QW transition also by comparison to the PL spectrum. The intensities of the transitions at 2.159 eV and 2.192 eV exhibit a ratio close to three suggesting that they are associated with the heavy and light hole transitions, respectively. [19] The bandgap of $Zn_{0.53}Cd_{0.47}Se$ was determined by

CER from a thick sample grown during the same run. The value that we found was E_0=2.080±0.005eV in good agreement with reference 20, which reported E_0=2.078±0.002 and spin-orbit splitting Δ_0=0.442±0.02eV. [20] Using our value for the bandgap and the reported spin-orbit splitting of Δ_0=0.442±0.02eV, we obtain $E_0 + \Delta_0 = 2.522$, which agrees well with the experimental value of table 1.

In order to make the assignments to the remaining observed transitions we have performed a calculation based on the envelope function approximation, which is based on the non-parabolicity of the bands. [21-22] In this calculation, it is important to know the values of the effective masses and the spin orbit splitting parameter, Δ_0. There are no reported values for the effective masses of these compounds. In order to approximate the required masses we have followed a two step procedure: first for ZnSe, we took the average value between the maximum and minimum reported values shown which is 0.15, shown in the parentheses of table I, for MgSe and CdSe the data were taken from reference 23, and 24 respectively. [23-24] We did not find any reported value for the effective mass of the light hole of the CdSe. Since, electron and heavy hole masses for CdSe are approximately two thirds of those corresponding to ZnSe, using this proportionality, we assumed that $m_{lh}(CdSe) = 2/3 m_{lh}(ZnSe)$. Also, using these values for the

binaries and a weighted composition average, we obtained the corresponding values for our compounds, which are also shown in table 5.1. The values obtained using this scheme where the mass of the electron, $m_e = 0.22$, mass of the heavy hole and light holes are $m_{hh} = 0.76$, $m_{lh} = 0.31$ respectively, and the spin orbit splitting parameter $\Delta_0 = 0.44$eV. [20]

With the effective masses listed in table 5.1, we calculated the energies of the different transitions as a function of the parameter $Q_c=\Delta E_c/\Delta E_0$ using the envelop approximation. Figure 5.2 shows the results of this calculation in solid lines for the transitions that fit better the experimental values of the transitions, which are represented by the horizontal dashed lines. These transitions correspond to the symmetry allowed (n=m) and symmetry forbidden but parity allowed (n=m±2,4…). As indicated in this figure by the dotted vertical line, the best agreement between the calculated and the experimental values for all the transitions was found for $Q_c = 0.82\pm0.02$. This corresponds to $\Delta E_c = 590$meV which is comparable to the larger reported values for ΔE_c and suggests that this Mg based II-VI material is an alternative to use in the intersubband devices such as QCLs. The results are summarized in table 5.2, which shows a good agreement between the calculated, and the experimental values.

5.2. Band Offset Determination of a $Zn_{0.13}Mg_{0.87}Se$ / $Zn_{0.53}Cd_{0.47}Se$ QW single QW:

In order to further increase the CBO, we have extended our investigation to the $Zn_xMg_{(1-x)}Se$ ternary material system, which is the ternary endpoint of the $Zn_xCd_yMg_{(1-x-y)}Se$ quaternary system (assuming y = 0). As was described in chapter 3, high quality zincblende ZnMgSe alloy lattice-matched to InP substrate was grown with a bandgap of as high as ~ 3.6 eV at 77K. QWs having ZnMgSe as the barrier layers and ZnCdSe as the well have been demonstrated in chapter 4. These QWs show emission from near-UV to the visible range of the spectrum. Since ΔE_g of the ZnMgSe (3.6 eV) and ZnCdSe (2.1 eV) is ~ 1.5 eV, a large conduction band offset can be expected from this system.

We have investigated the conduction band offset of a $Zn_{0.13}Mg_{0.87}Se$ / $Zn_{0.53}Cd_{0.47}Se$ QW with a QW thickness of 35Å using CER. The structure consists of a 35 Å thick ZnCdSe QW is sandwiched between a 0.1 μm and 0.3 μm top and bottom barrier layer, respectively. Instead of a ZnCdSe cap layer, a 100 Å CdSe cap layer was used to avoid any deoxidation. This was done to avoid complications in the interpretation of the CER measurement since the active region consists of a ZnCdSe QW. Figure 5.3 shows the RT and 77K photoluminescence measurement of the sample, which exhibits a

strong PL emission at 2.21 eV at RT and 2.267 eV at 77K. A value of the parameter, $Q_c = \Delta E_c / \Delta E_g$ of ~ 0.8 was used to obtain the conduction band offset based on the calculation of $Zn_{0.53}Cd_{0.47}Se/Zn_{0.27}Cd_{0.23}Mg_{0.50}Se$ single quantum well (QW) structure described in the previous section.

The CER spectrum for this sample is shown in figure 5.4. The signal at 1.69 eV corresponds to the CdSe cap layer, which also exhibits the typical Franz-Keldish oscillations (FKO), which are the intrinsic absorptions of photons with energies less than the bandgap in semiconductor. [25] These oscillations originate in the intermediate field regime of the electromodulation. The FKOs originates due to the fact that, under the influence of the electric field F in the *z*-direction, the energy bands are tilted by qF_z. An electron attempting to tunnel from the valence to the conduction band sees a barrier due to the tilt. If during the tunneling process the electron interacts with a photon of energy *E,* the effective width of the barrier to be traveled by the electron become smaller. If the photon energy is less than the bandgap E_g, then the transmission probability is exponential as a consequence of photon assisted tunneling. However, if $E_{photon} > E_g$ then the transmission probability becomes an oscillatory function and give rises to FKOs. [26]

The transitions in the range of 2.2 – 2.8 eV correspond to five QW transitions. In order to assign the observed transitions to the QW processes we calculate the energies corresponding to the QW processes and compares the calculated value to the experimentally observed transition energies. For this we have performed a calculation based on the envelope approximation using a $Q_c \sim 0.8$. The values were calculated for an optimum quantum well layer thickness of 33.6Å, which agrees with the nominal experimental value (35Å). The value for the band gap energy of the barrier $E_0 = 3.52$eV, was obtained from the room temperature PL measurements of a bulk layer grown in the same day. The transitions of the ZnMgSe barrier layer cannot be seen in the spectrum due to the limit of the CER apparatus at high energies.

The results are summarized in Table 5.3. A very good agreement was obtained between the experimental and calculated transitions for $\Delta E_c = 80\%$ of the band gap discontinuity (ΔE_0), which yields $\Delta E_c = 1.12$ eV. This assumption is in agreement with the common anion rule which states that two semiconductors with a common anion and lattice matched should have the most of the band discontinuity in the conduction band. [27] Assuming that the separation between electron subbands in the QW can be as high as 70% of the ΔE_c, one can anticipate that emission energies from QCLs made with QWs of these structures of the appropriate well width, may approach 1.55

μm showing a potential application of this material system in quantum cascade lasers and other intersubband devices for optical communications applications. Figure 5.5 illustrates the transitions observed in the CER. By calculating the difference between the energy of the E_1H_1 and E_2H_2 transition we obtain the sum of E_2-E_1 and H_2-H_1 intersubband energies assuming the 80% of this represent the difference between electron energy levels. We can estimate the conduction band intersubband energy (E_2-E_1) of ~ 300 meV which would yield an emission wavelength of ~ 4.13 μm. By using thinner QWs, shorter wavelengths can be achieved. A conservative estimate of the shortest wavelength that could be achieved, assuming that the separation between the electron energy levels can be as high as 60% of the conduction band offset, is 1.84 μm.

In conclusion, using CER measurements and the envelope function approximation, we have determined the conduction band offset of the nearly lattice matched ZnCdSe/ZnMgSe QW structure. A CER spectrum exhibiting several QW transitions was obtained. These transitions were identified using an envelope approximation. The assignments are consistent with a very large conduction band offset of ~1.12 eV for this QW system. The shortest intersubband emission wavelength that might be obtained from such a QW was estimated to be 1.84 μm. We suggest that, lattice matched

ZnCdSe/ZnMgSe QWs grown on InP may be excellent candidates for applications in intersubband devices for optical communications and other devices where a large conduction band offset of 1.12 eV is desirable.

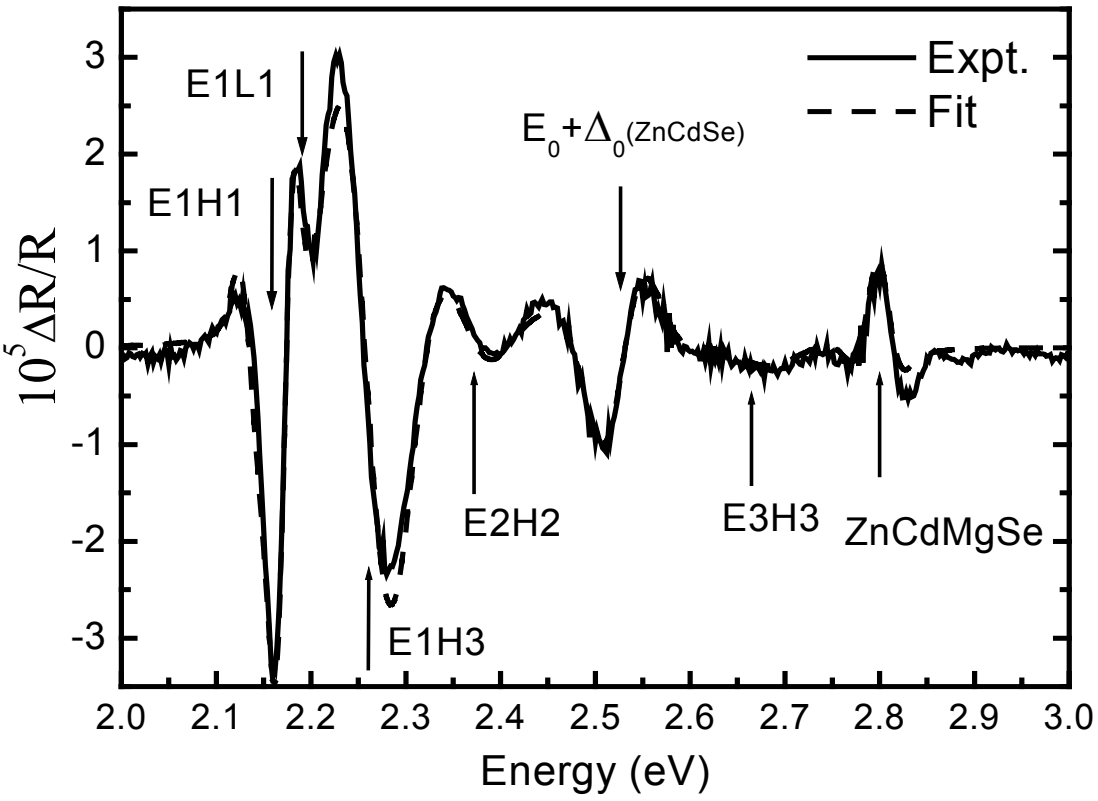

Figure 5.1. Room temperature CER measurement of $Zn_{0.53}Cd_{0.47}Se/Zn_{0.29}Cd_{0.24}Mg_{0.47}Se$ single QW. The solid line represents the experimental $\Delta R/R$ spectra. The dashed line is a fit yielding the energies indicated by the arrows.

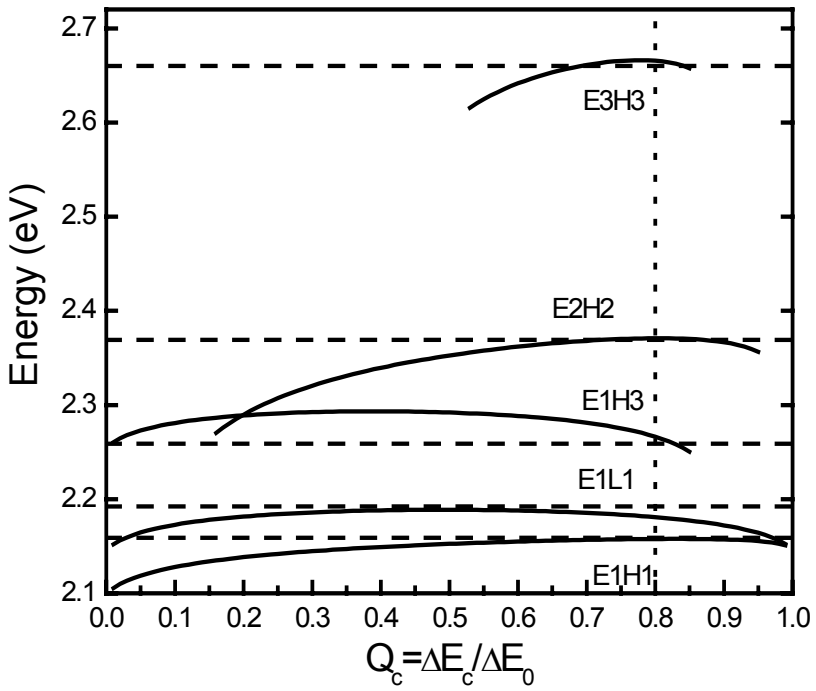

Figure 5.2. Energies of the transitions determined by the envelope function approximation vs. Qc ($=\Delta E_c/\Delta E_0$).

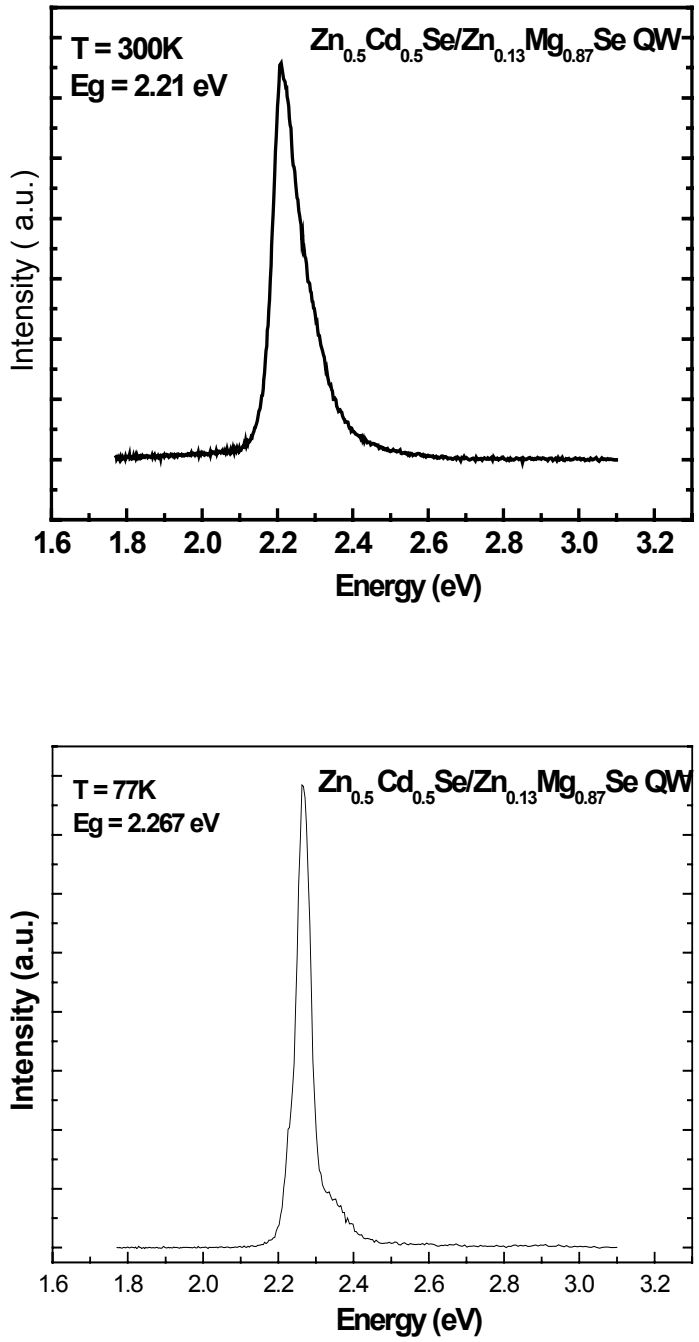

Figure 5.3. Room temperature and 77K PL emission spectrum of a nearly lattice matched $Zn_{0.13}Mg_{0.87}Se$ / $Zn_{0.53}Cd_{0.47}Se$ QW with a QW thickness of 35Å.

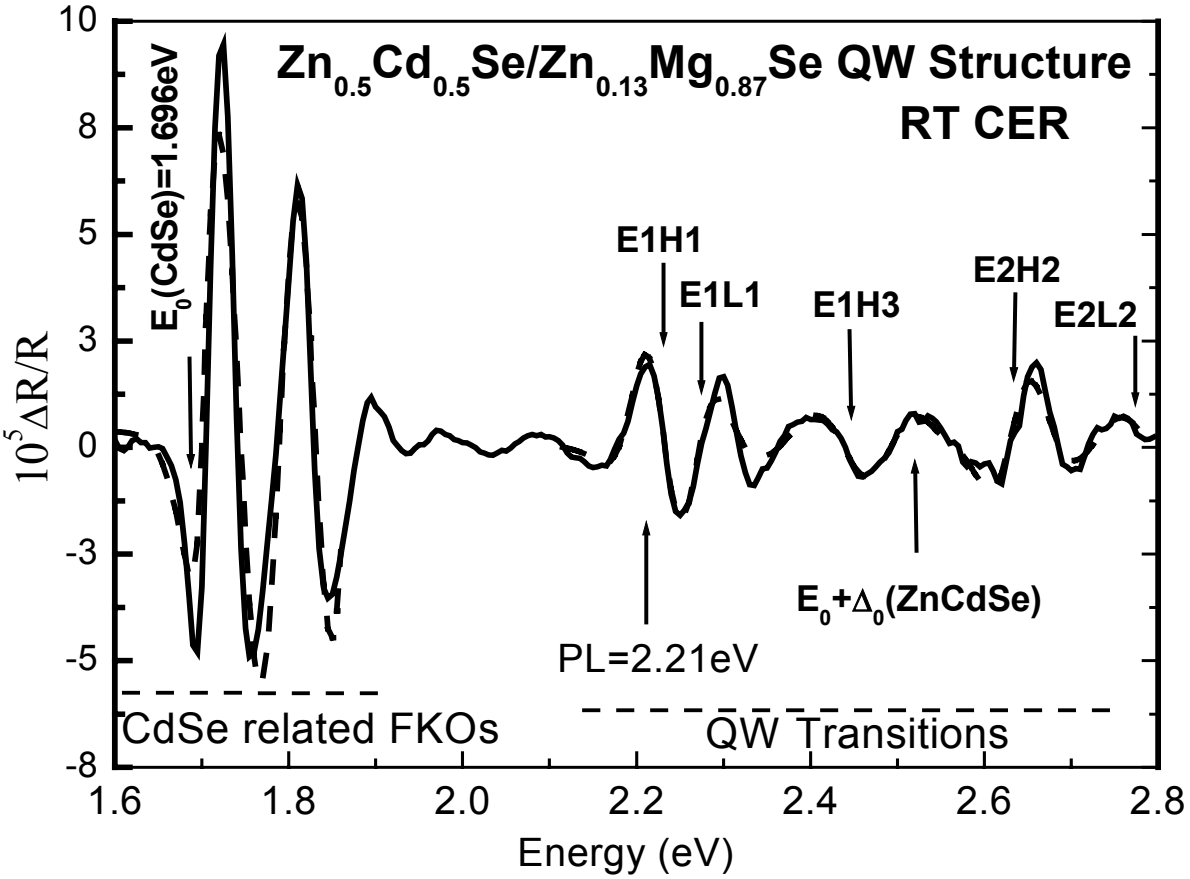

Figure 5.4. Room Temperature CER spectrum where the solid line represents the experimental $\Delta R/R$ spectra and dashed line is a fit yielding the energies indicated by the arrows.

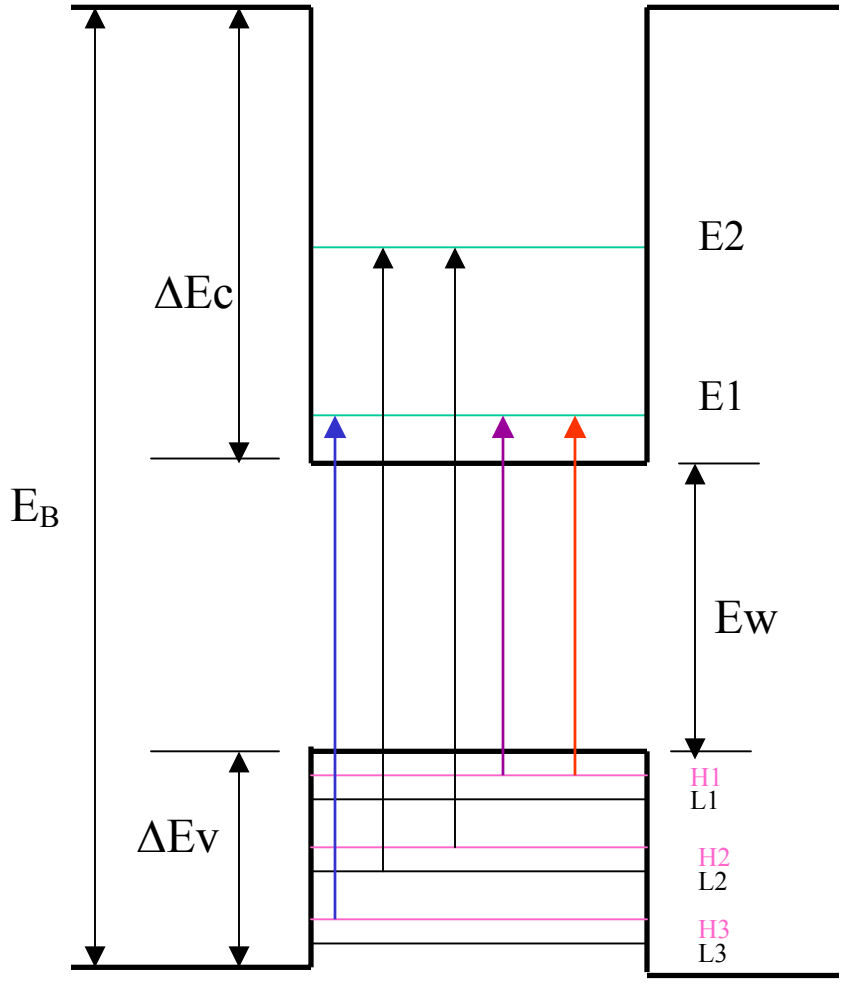

Figure 5.5. Band diagram showing the transitions in the $Zn_{0.13}Mg_{0.87}Se$ / $Zn_{0.53}Cd_{0.47}Se$ QW structure that were obtained from the CER data.

Table 5.1. Values of the parameters used in the calculation.

Parameter	ZnSe	CdSe	MgSe	$Zn_{0.27}Cd_{0.23}Mg_{0.50}Se$	$Zn_{0.53}Cd_{0.47}Se$
E_0(eV)				2.800[a]	2.080[a]
$\mathbf{m_e}$	0.15[b] (0.13…0.17)	0.11[c]	0.23[d]	0.18	0.13
m_{hh}	0.66[b] (0.57...0.75)	0.44[c]	0.78[d]	0.67	0.56
m_{lh}	0.145	0.09	0.33[d]	0.22	0.11
Δ_0(eV)	0.43[e]	0.42[e]	0.40[d]	0.414[f]	0.442[a]
QW Thickness (Å)			35 (Expt.)	33.6 (Calculated)	

[a] Experimental value.

[b] Average between maximum and minimum values showed in parentheses, these values were obtained from Ref. 24.

[c] Reference [28]

[d] Reference [29]

[e] Reference [30]

[f] Interpolated value using the binary values.

Table 5.2. Experimental and calculated interband energies of $Zn_{0.53}Cd_{0.47}Se/Zn_{0.29}Cd_{0.24}Mg_{0.47}Se$ single QW structure.

Transition	Experiment (eV)	Theory (eV)
E1H1	2.159±0.005	2.158
E1L1	2.192±0.005	2.180
E1H3	2.259±0.005	2.261
E2H2	2.369±0.005	2.371
E3H3	2.660±0.005	2.664
$E_0+\Delta_0$	2.525±0.005	2.522 [a]
E_0(Barrier)	2.800±0.005	

Table 5.3. Experimental (fit from CER) and calculated (envelope function calculation) values of the interband transition energies of a $Zn_{0.13}Mg_{0.87}Se$ / $Zn_{0.53}Cd_{0.47}Se$ QW structure.

Transitions	Fit from CER (eV)	Envelope Calculation (eV)
E1H1	2.228	2.229
E1L1	2.272	2.269
E1H3	2.448	2.444
$E_0+\Delta_0$ (ZnCdSe)	2.521	2.525 exp. (ref. 3) 2.522 calc. (ref. 16)
E2H2	2.635	2.624
E2L2	2.777	2.780

Chapter 6

Summary

The purpose of the research presented in this dissertation was to develop new II-VI materials with large conduction band offsets for application in intersubband devices such as Quantum Cascade Lasers. A series of high crystalline quality zincblende $Zn_xMg_{1-x}Se$ alloys was grown for the first time lattice matched to InP (001) substrates by molecular beam epitaxy. The use of InP as a substrate allows us to optimize the materials quality of the high Mg content compositions, since near lattice matching to this substrate is achieved with as much as ~87% Mg concentration. This alloy has a bandgap of 3.6 eV at 77K with a full width and half maximum (FWHM) of 112 meV. Based on the extrapolation of our data, it was determined that the band gap of zincblende MgSe is 3.74 eV, resolving the existing discrepancies between several reported and estimated values for this parameter in the literature. Several groups have reported the presence of bowing in the bandgap relationship with composition for ZnMgSe alloys, but we have found no bowing in ZnMgSe alloy system. This is due to the fact that samples with high Mg content previously grown on GaAs or other

substrates by other authors exhibited a mixture of rocksalt or wurtzite phase instead of pure, single phase zincblende, as was the case in our samples.

Using lattice-matched ZnMgSe as a barrier we have grown a series of near lattice matched ZnCdSe/ZnMgSe quantum well structures on InP with varying the thickness of the well, ranging between 6Å and 60Å. These samples exhibited emission that ranged form the near-UV, and throughout the visible range of the spectrum. The dependency of the QW emission with QW layer thickness was modeled using a finite barrier model.

Room temperature CER measurements were also performed to calculate the conduction band offset in ZnCdSe/ZnMgSe QW system. The experimental values of the transitions were assigned using a fit and the theoretical value was based on envelope approximation calculation. Experimental and theoretical values agreed well. Assuming 80% of the band discontinuity in the conduction band, we have calculated the conduction band offset as high as 1.12 eV. Using this system, we estimate that intersubband emission wavelengths as short as 1.84 μm can be achieved. Integration of ZnMgSe alloys with such a high bandgap and high band offset, will make this material a suitable candidate for application in intersubband devices such as QCLs in the near-IR region in ultrafast optical

communications, and thus resolve some of the present challenges in other material system in developing such high quality QCLs.

Publication and Conference Presentations

Publications:

1. "*Molecular Beam Epitaxial growth and characterization of zincblende ZnMgSe on InP (001)"*- **Mohammad Sohel**, Martin Munoz, Maria C. Tamargo, Appl. Phys. Lett., **85**, 2794, (2004).

2. *"Optical Characterization and Evaluation of the Conduction Band Offset for ZnCdSe/ZnMgSe Quantum Wells Grown on InP(001) by MBE"*- **Mohammad Sohel,** Xuecong. Zhou, Hong Lu, M. Noemi Perez Paz, Maria Tamargo, Martin Munoz, Accepted for Publication, J. Vav. Sci. Technol. B, **23,** 1209 (2005).

3. *"CdSe self-assembled quantum dots with ZnCdMgSe barriers emitting throughout the visible spectrum"*- M. N. Perez-Paz, X. Zhou, M. Munoz, H. Lu, **M. Sohel**, and M. C. Tamargo, Appl. Phys. Lett., **85**, 6395, (2004).

4. *"Single layer and stacked CdSe self-assembled quantum dots with ZnCdMgSe barriers for visible light emitters"*- M.N. Perez-Paz, X. Zhou, M. Munoz, **M. Sohel**, Hong Lu, Francisco Fernandez and Maria C. Tamargo, J. Vav. Sci. Technol. B, 23, 1236 (2005).

Conference Presentations:

1. "*ZnMgSe alloys lattice matched to InP (001) grown by Molecular Beam Epitaxy for inter subband devices and near UV emitters*"- **Mohammad Sohel**, Martin Munoz, Maria C. Tamargo, Oral presentation, 22nd North American Molecular Beam Epitaxy Conference, October 10 – 13 2004, Banff, Canada.

2. *"Quantum Confinement Effects in Structures Grown via Delta-doping during Molecular Beam Epitaxy"*- Igor L. Kuskovsky, Y. Gu, M. van der Voort, G. F. Neumark, X. Chou, **M. Sohel**, M. Munoz, M. C. Tamargo, Poster presentation, 11th International Conference on II-VI Compounds, September 22 – 26 2003, Niagara Falls, New York.

3. *“ (N+Te) –δ^3 doping of ZnBeSe alloys for p-type doping grown by Molecular Beam Epitaxy”* - Oral presentation, IGERT Annual Conference, July 2002, Pocono, Pennsylvania.

References

Chapter 1

1. R. F. Kazarinov, R. A. Suris, Sov. Phys. Semicond., **5**, 707 (1971).

2. J. Faist, F. Capasso, D. L. Sivco, C. Sirtori, A. L. Hutchinson, and A. Y. Cho, Science **264**, 553 (1994).

3. F. Capasso, C. Gmachl, A. Tredicucci, A. L. Hutchinson, D. L. Sivco, and A. Y. Cho. Opt. Photonics News, 10 (1999).

4. J. Faist, F. Capasso, C. Sirtori, D. L. Sivco, A. L. Hutchinson, S.N. Chu and A. Y. Cho, App. Phys. Lett. **72**, 680 (1998).

5. F. Capasso, R. Paiella, A. Tredicucci, A. Hutchinson, D. L. Sivco, J. Baillargeon, A. Y. Cho, H. C. Liu, IEEE J. Sel. Top. Quantum Electron. **6**, 931 (2000).

6. C. Sirtori, P. Kruck, S. Barbieri, P. Collot, J. Nagle, M. Beck, and J. Faist and U. Oesterle App. Phys. Lett. **73**, 3486 (1998).

7. C. Gmachl, H. M. Ng, and A. Y. Cho, App. Phys. Lett. **79**, 1590 (2001).

8. C. Gmachl, H. M. Ng, S. N. G. Chu, and A. Y. Cho, App. Phys. Lett. **77**,

3722 (2000).

9. B. H. Yang, D. Zhang, Rui Q. Yang, C.-H. Lin, S. J. Murry, and S. S. Pei, App. Phys. Lett. **72**, 2220 (1998).

10. R. Q. Yang, B. H. Yang, D. Zhang, C.-H. Lin, S. J. Murry, H. Wu, and S. S. Pei, App. Phys. Lett. **71**, 2409 (1997).

11. I. Bormann, K. Brunner, S. Hackenbuchner, G. Zandler, G. Abstreiter, S. Schmult, and W. Wegscheider, Appl. Phys. Lett. **80**, 2260 (2002).

12. R. Akimoto, K. Akita, F. Sasaki, and T. Hasama, Appl. Phys. Lett. **81**, 2998 (2002).

13. R. Akimoto, K. Akita, F. Sasaki, and S. Kobayashi, Appl. Phys. Lett. **80**, 2433 (2002).

14. R. Akimoto, Y. Kinpara, K. Akita, F. Sasaki, and S. Kobayashi, Appl. Phys. Lett. **78**, 580 (2001).

15. M. Göppert, M. Grün, C. Maier, S. Petillon, R. Becker, A. Dinger, A. Storzum, M. Jörger, and C. Klingshirn, Phys. Rev. B **65**, 115334 (2002).

16. C. Gmachl, H. M. Ng, and A. Y. Cho, Appl. Phys. Lett. **79**, 1590 (2001).

17. C. Gmachl, H. M. Ng, S. N. G. Chu, and A. Y. Cho, Appl. Phys. Lett. **77**, 3722 (2000).

18. B. H. Yang, D. Zhang, Rui Q. Yang, C. H. Lin, S. J. Murry, and S. S. Pei, Appl. Phys. Lett. **72**, 2220 (1998).

19. R. Q. Yang, B. H. Yang, D. Zhang, C. H. Lin, S. J. Murry, H. Wu, and S. S. Pei, Appl. Phys. Lett. **71**, 2409 (1997).

20. R. Akimoto, K. Akita, F. Sasaki, and T. Hasama, Appl. Phys. Lett. **81**, 2998 (2002).

21. R. Akimoto, K. Akita, F. Sasaki, and S. Kobayashi, Appl. Phys. Lett. **80**, 2433 (2002).

22. M. Göppert, M. Grün, C. Maier, S. Petillon, R. Becker, A. Dinger, A. Storzum, M. Jörger, and C. Klingshirn, Phys. Rev. B **65**, 115334 (2002).

23. N. Dai, A. Cavus, R. Dzakpasu, M. C. Tamargo, F. Semendy, N. Bambha, D. M. Hwang, C. Y. Chen, Appl. Phys. Lett., **66**, 2742 (1995).

24. M. C. Tamargo, N. Dai, A. Cavus, R. Dzakpasu, W. Krystek, F. H. Pollak, F. Semndy, N. Bambha, P. Boyd, D. M. Hwang, C. Y. Chen, SPIE Proceedings, **2346** (1995).

25. M. A. Haase, J. Qiu, J. M. DePuydt, H. Cheng, Appl. Phys. Lett., **59**, 1272 (1991).

26. M. C. Tamargo, A. Cavus, L. Zeng, N. Dai. N. Bambha, A. Gray, F. Semendy, W. Krystek, F. H. Pollak, J. Electron. Matter., **25**, 259 (1996).

27. L. Zeng, Y. Guo, B. X. Yang, A. Cavus, W. Lin, Y. Y. Luo, Y. C. Chen, M. C. Tamargo, Appl. Phys. Lett., **72**, 3136 (1998).

28. M. C. Tamargo, W. Lin, S. P. Guo, Y. Luo, Y. Guo, Y. C. Chen, J. Crystal Growth, **214/214**, 1058 (2000).

29. M. Muñoz, H. Lu, X. Zhou, F. H. Pollak, M. C. Tamargo, Appl. Phys. Lett. **83**, 1995 (2003)

Chapter 2

1. A. Y. Cho, Thin Solid Films **100**, 291 (1983).

2. M. A. Herman, T. H. Sitter, *Molecular Beam Eptaxy: Fundamentals and Current Status*, Ed. M. B. Panish, Springler series in materials Science 7, Springer-Verlag, Berlin Heidelberg (1989).

3. V. Swaminathan, A. T. Macrander, *Material Aspects of GaAs and InP Based Structures*, Prentice Halls, NJ, 131 (1991).

4. A. Y. Cho, J. Vac. Sci. Technol. **8**, 31 (1971).

5. A. Y. Cho, J. R. Arthur, Prog. Solid State Chem. **10**, 157 (1975).

6. A. Avery, D. Sudijono, J. Jones, B. Joyce, Appl. Surf. Sci., **104/105**, 539 (1996).

7. H. H. Farrel, M. C. Tamargo, J. H. de Miguel, F. S. Turso, D. M. Huang, and R. E. Nahory, J. Appl. Phys. **69**, 7021 (1991).

8. K. Ploog, *Microscopical structuring of solids by molecular beam epitaxy*. Angewandte Chemie - Int. English ed*,* **27**,593-621 (1988).

9. J. H. Neave and B. A. Joyce, Appl. Phys. **A 31**, 1 (1993).

10. D. K. Bowen, B. K. Tanner, *High Resolution X-ray Diffractometry and Topography*, Taylor and Francis Inc., Pennsylvania (1998).

11. J. Hornastra, W. J. Bartels, J. Cryst. Growth, **44**, 513 (1978).

12. L. Pavesi, M. Guzzi, J. Appl. Phys. **75**, 4779 (1994).

13. H. G. Tompkins, W. A. Mc Gahan, Spectroscopic Ellipsometry and Reflectometry, John Willey and Sons, Inc., New York (1999).

14. F. H. Pollak, H. Shen, Mater. Sci. Eng. **R10**, 275 (1993).

15. F. H. Pollak, *Handbook on Semiconductors,* vol. 2, ed. M. Balkanski, north Holland, Amsterdam, p. 527 (1994).

16. H. Shen, M. Dutta, J. Appl. Lett., **78**, 2151 (1995).

17. F. H. Pollak, *Photonic Probes of Surfaces,* ed. P. Halevi, North Holland, New York, p. 175 (1995).

18. O. J. Glembocki, B. V. Shanabrook, *Semiconductors and Semimetals,* vol. 36, ed. D. G. Seiler and C. L. littler, Academic Press, New York, p. 221 (1992).

19. F. H. Pollak, Proc. Soc. Photo-optical Instrum. Eng., **276**, 142 (1981).

20. M. Munoz, H. Lu, M. C. Tamargo, Appl. Phys. Lett., **85,** 1995 (2003).

21. X. Yin, F. H. Pollak, Appl. Phys. Lett., **59**, 2305 (1991).

22. X. Yin, X. Guo, F. H. Pollak, G. D. Pettit, J. M. Woodwall, T. P. Chin, C. W. Tu, Appl. Phys. Lett., **60,** 1336 (1991).

Chapter 3

1. J. Faist, F. Capasso, D. L. Sivco, C. Sirtori, A. L. Hutchinson, and A. Y. Cho, Science **264**, 553 (1994).

2. C. Sirtori, P. Kruck, S. Barbieri, P. Collot, J. Nagle, M. Beck, and J. Faist and U. Oesterle App. Phys. Lett. **73**, 3486 (1998).

3. J. Faist, F. Capasso, C. Sirtori, D. L. Sivco, A. L. Hutchinson, S.N. Chu and A. Y. Cho, App. Phys. Lett. **72**, 680 (1998).

4. C. Gmachl, H. M. Ng, and A. Y. Cho, App. Phys. Lett. **79**, 1590 (2001).

5. C. Gmachl, H. M. Ng, S.-N. G. Chu, and A. Y. Cho, App. Phys. Lett. **77**, 3722 (2000).

6. B. H. Yang, D. Zhang, Rui Q. Yang, C.-H. Lin, S. J. Murry, and S. S. Pei, App. Phys. Lett. **72**, 2220 (1998).

7. R. Q. Yang, B. H. Yang, D. Zhang, C.-H. Lin, S. J. Murry, H. Wu, and S. S. Pei, App. Phys. Lett. **71**, 2409 (1997).

8. I. Bormann, K. Brunner, S. Hackenbuchner, G. Zandler, G. Abstreiter, S. Schmult, and W. Wegscheider, Appl. Phys. Lett. **80**, 2260 (2002).

9. R. Akimoto, K. Akita, F. Sasaki, and T. Hasama, Appl. Phys. Lett. **81**, 2998 (2002).

10. R. Akimoto, K. Akita, F. Sasaki, and S. Kobayashi, Appl. Phys. Lett. **80**, 2433 (2002).

11. R. Akimoto, Y. Kinpara, K. Akita, F. Sasaki, and S. Kobayashi, Appl. Phys. Lett. **78**, 580 (2001).

12. M. Göppert, M. Grün, C. Maier, S. Petillon, R. Becker, A. Dinger, A. Storzum, M. Jörger, and C. Klingshirn, Phys. Rev. B **65**, 115334 (2002).

13. S. Guo, M. C. Tamargo, in M. O. Manasreh (ed.), *Optoelectronic Properties of Semiconductor and Superlattices*, Vol. 12, Taylor and Francis, New York (2002), p. 262.

14. M. Muñoz, H. Lu, X. Zhou, F. H. Pollak, M. C. Tamargo, Appl. Phys. Lett. **83**, 1995 (2003).

15. H. Okuyama, T. Miyajima, Y. Morinaga, F. Hiei, M. Ozawa, K. Akimoto, Electron. Lett. **28**, 1798 (1992).

16. H. Okuyama, K. Nakano, T. Miyajima, K. Akimoto, Jpn. J. Appl. Phys. **30**, L1620 (1991).

17. B. Jobst, D. Hommel, U. Luntz, T. Gerhard, G. Landwehr, Appl. Phys. Lett. **69**, 97 (1996).

18. M. Worz, E. Griebl, Th. Reisinger, R. Flierl, B. Haserer, T. Semmler, T. Frey, W. Gebhardt, Phys. Stat. Sol. B **202,** 805 (1997).

19. B. Vögele, C. Morhain, B. Urbaszek, S. A. Telfer, K. A. Prior, B. C. Cavenett, J. Crystal Growth **201/202**, 950 (1999).

20. M. Th. Litz, K. Watanabe, M. Korn, H. Ress, U. Lunz, W. Ossau, A. Waag, G. Landwehr, Th. Walter, B. Neubauer, D. Gerthsen and U. Schüssler, J. Crys Growth **159**, 54 (1996).

21. C. Morhain, D. Seghier, B. Vogele, C. O'Donnell, K.A. Prior, B. C. Cavenett, H.P. Gislason, J. Crystal Growth **214/215,** 482 (2000).

22. G. J. Davies, R. Heckingbottom, H. Ohno, C. E. C. Wood, A. R. Calawa, Appl. Phys. Lett., **37(3)**, 290 (1980).

23. E. Snoeks, L. Zhao, B. Yang, A. Cavus, L. Zeng, M. C. Tamargo, J. Cryst. Growth, **179**, 83 (1997).

24. E. Snokes, S. Herko, L. Zhao, B. Yang, A. Cavus, L. Zeng, M. C. Tamargo, Appl. Phys. Lett., **70**, 2259 (1997).

25. N. Dai, A. Cavus, R. Dzakpasu, M. C. Tamargo, F. Semendy, N. Bambha, D. M. Hwang, C. Y. Chen, Appl. Phys. Lett., **66**, 2742 (1995).

26. L. Zeng, Ph.D. thesis, The City University of New York (1998)

27. F. Jiang, Q. Liao, G. Fan, C. Xiong, X. Peng, C. Pan, N. Liu, J. Crystal Growth, **183**, 289 (1998).

28. S. P. Guo, X. Zhou, O. Maksimov, M. C. Tamargo J. Vac. Sci. Tech. B, **19,** 1635 (2001).

29. P. Prete, N. Lovergine, L. Tapfer, C. Zanotti-Fregonara, A. M. Mancini, J. Crystal Growth, **214/215**,119 (2000).

30. B. D. Cullity, *Elements of X-ray Diffraction*, Adison-Wesley, Massachusetts, (1977).

31. H. Okuyama, Y. Kishita, and A. Ishibashi, Phys. Rev. B, **57**, 2257 (1998).

32. P. P. Ewald, Handbuch der Physik, Vol. **23**, 691 (1933).

33. B. W. Bitterman, G. Hilderbrandt, Acta Cryst. **3**, 187 (1968).

34. L. Tapfer, W. Stoltz, K. Poog, J. Appl. Phys. **66** (1989) 3217.

35. N. Kato, A. R. Lang, Acta Cryst. **12**, 787 (1959).

36. W. T. Stacy, M. M. Janssen, J. Cryst. Growth, **27**, 282 (1974).

37. B. Salazar-Hernandez, M. A. Vidal, H. Navarro-Contreras, C. Vasquez-Lopez, Thin Solid Film, **352**, 269 (1999).

38. J. A. Van Vechten and T. K. Bergstresser, Phys. Rev. B, **1**, 3351 (1970).

39. R. Hill, J. Phys. C **7,** 521 (1974).

Chapter 4

1. Okuyama, K. Nakano, T. Miyajima, K. Akimoto, Jpn. J. Appl. Phys. **30**, L1620 (1991).

2. M. Sohel, M. Muñoz, M. C. Tamargo, Appl. Phys. Lett., **85**, 2794 (2004).

3. Mohammad Sohel, Xuecong Zhou, Hong Lu, Noemi Perez Paz, Martin Munoz, Maria C. Tamargo, J. Vac. Sci. Technol. B **23**, 1209 (2005).

4. F. H. Pollak, H. Shen, Mater. Sci. Eng., **R. 10**, 275 (1993)

5. D. Branson, Am. J. Phys., **47**, 1000 (1979).

6. I. N. Levine, *Quantum Chemistry*, 5th ed. Prentice Hall, New Jersey (2000).

7. G. Bastard, *Wave mechanics applied to semiconductor heterostructures*, Les Editions de Physique, France (1988) pp. 3-6

8. J A López-Villanueva, J A Jiménez-Tejada, A Palma, S Rodríguez Bolívar and J E Carceller, Semicond. Sci. Technol., **20**, 532 (2005).

9. D. F. Nelson, R. C. Miller, D. A. Kleinman, Phys. Rev. B., **35**, 7770 (1987).

Chapter 5

1. J. Faist, F. Capasso, D. L. Sivco, C. Sirtori, A. L. Hutchinson, and A. Y. Cho, Science **264**, 553 (1994).

2. C. Gmachl, H. M. Ng, and A. Y. Cho, App. Phys. Lett. **79**, 1590 (2001).

3. C. Gmachl, H. M. Ng, S. N. G. Chu, and A. Y. Cho, App. Phys. Lett. **77**, 3722 (2000).

4. B. H. Yang, D. Zhang, Rui Q. Yang, C.-H. Lin, S. J. Murry, and S. S. Pei, App. Phys. Lett. **72**, 2220 (1998).

5. R. Q. Yang, B. H. Yang, D. Zhang, C. H. Lin, S. J. Murry, H. Wu, and S. S. Pei, App. Phys. Lett. **71**, 2409 (1997).

6. I. Bormann, K. Brunner, S. Hackenbuchner, G. Zandler, G. Abstreiter, S. Schmult, and W. Wegscheider, Appl. Phys. Lett. **80**, 2260 (2002).

7. R. Akimoto, K. Akita, F. Sasaki, and T. Hasama, Appl. Phys. Lett. **81**, 2998 (2002).

8. R. Akimoto, K. Akita, F. Sasaki, and S. Kobayashi, Appl. Phys. Lett. **80**, 2433 (2002).

9. R. Akimoto, Y. Kinpara, K. Akita, F. Sasaki, and S. Kobayashi, Appl. Phys. Lett. **78**, 580 (2001).

10. M. Göppert, M. Grün, C. Maier, S. Petillon, R. Becker, A. Dinger, A. Storzum, M. Jörger, and C. Klingshirn, Phys. Rev. B **65**, 115334 (2002).

11. C. Gmachl, H. M. Ng, and A. Y. Cho, Appl. Phys. Lett. **79**, 1590 (2001).

12. C. Gmachl, H. M. Ng, S. N. G. Chu, and A. Y. Cho, Appl. Phys. Lett. **77**, 3722 (2000).

13. B. H. Yang, D. Zhang, Rui Q. Yang, C. H. Lin, S. J. Murry, and S. S. Pei, Appl. Phys. Lett. **72**, 2220 (1998).

14. R. Q. Yang, B. H. Yang, D. Zhang, C. H. Lin, S. J. Murry, H. Wu, and S. S. Pei, Appl. Phys. Lett. **71**, 2409 (1997).

15. R. Akimoto, K. Akita, F. Sasaki, and T. Hasama, Appl. Phys. Lett. **81**, 2998 (2002).

16. R. Akimoto, K. Akita, F. Sasaki, and S. Kobayashi, Appl. Phys. Lett. **80**, 2433 (2002).

17. M. Göppert, M. Grün, C. Maier, S. Petillon, R. Becker, A. Dinger, A. Storzum, M. Jörger, and C. Klingshirn, Phys. Rev. B **65**, 115334 (2002).

18. O. J. Glembocki and B. V. Shanabrook, in *Semiconductors and Semimetals*, edited by R. K. Willardson and A. C. Beer (Academic, New York 1992), **36**, p. 221 (1992).

19. F. H. Pollak in *Group III Nitride Semiconductor Compounds*, ed. By B. Gil (Clarendon, Oxford, 1998) p. 158.

20. T. Holden, P. Ram, F. H. Pollak, J. L. Freeouf, B. X. Yang, and M. C. Tamargo, Phys. Rev. B **56**, 4037 (1997).

21. G. Bastard and J. A. Brum, IEEE J. Quantum Electron. **QE-22**, 1625 (1986).

22. G. Bastard, *Wave Mechanics applied to Semiconductor Heterostructures*, Les editions de Physique, France (1988).

23. K. L. Leo, Y. P. Feng, M. F. Li, T. C. Chong, J. B. Xia, Semicond. Sci. Technol., **9**, 349 (1994).

24. *Semiconductors- BasicData,* 2nd ed., edited by O. Madelung, Sringer, Berlin, (1996).

25. T. M. Gassym, Phys. Rev. B, **68**, 155205 (2003).

26. F. H. Pollak, H. Shen, Material Science and Engineering: R **10,** 275 (1993).

27. W. Harrison, J. Vac. Sci. Tecnol. **14**, 1016, (1977); J. Vac. Sci. Tecnol. B **3**, 1231 (1985).

28. R. Paiella, F. Capasso, C. Gamachi, C. G. Bethea, D. L. Sivco, J. N. Baillargeon, A. L. Hutchinson, A. Y. Cho, IEEE Photonics Technol. Lett. **12**, 780, (2000).

29. K. L. Teo, Y. P. Feng, M. F. Li, T. C. Chong, J. B. Xia, Semicond. Sci. Technol., **9**, 349 (1994).

30. P. Lawaetz, Phys. Rev. B, **4,** 3460 (1971).